

EVALUATION OF NON-SUPPORTED OVERHANGS PRODUCED BY AEROSWIFT HIGH-SPEED LASER POWDER BED FUSION

Mfanufikile Shange

**Dissertation submitted in fulfilment of the requirements for the degree
MASTER of ENGINEERING: MECHANICAL ENGINEERING**

in the

Department of Mechanical and Mechatronics Engineering

Faculty of Engineering, Built Environment and Information Technology

at the

Central University of Technology, Free State

Supervisor: Prof. Ihar Yadroitsau, Ph.D.

Co-supervisors: Prof. Sisa Lesley Pityana, Ph.D.

Dr Ina Yadroitsava, Ph.D.

Bloemfontein

December 2019

Declaration of independent work

I, Mfanufikile Shange, identity number _____ and student number _____, do hereby declare that this research project submitted to the Central University of Technology, Free State (CUT) for the Master of Engineering in Mechanical Engineering, is my own independent work; and complies with the code of academic integrity, as well as other relevant policies, procedures, rules and regulations of the Central University of Technology, Free State; and has not been submitted previously to any institution by myself or any other person in fulfilment of the requirements for the attainment of any qualification.



Signature of student.

Date 12 February 2020

Acknowledgements

Firstly, I would like to thank the Lord for giving me the strength and courage to complete my studies.

A special thanks to my supervisors, Prof Igor Yadroitsev (Ihar Yadroitsau) and Dr Ina Yadroitsava from the Central University of Technology, Free State, for their guidance and support throughout the duration of this project. Their willingness to always be available to assist whenever help was needed is highly appreciated. I would also like to thank my co-supervisor from the CSIR National Laser Centre, Prof Sisa Pityana, for his mentorship. He helped me set high standards for myself and showed me that I could achieve more than I imagined.

I wish to express my thanks to Prof Anton du Plessis from Stellenbosch University for his expertise in the CT scan and his contribution to this work. I would also like to thank my colleagues at the National Laser Centre for their moral support. Our daily conversations kept me motivated.

My sincere thanks to the CSIR, Aeroswift project, SARChI and CPAM programmes for financial support provided to complete my research.

Last but foremost, I would like to thank the people who are dear to my heart: my wife (Azile Geza) and my daughters (Khanya and Zizo) for their support and understanding during the times I had to be away working on my research.

This work is based on the research supported by the South African Research Chairs Initiative of the Department of Science and Technology and National Research Foundation of South Africa (Grant № 97994) and Aeroswift Project № LMEBB70 funded by the Department of Science and Technology.

Abstract

Additive manufacturing (AM) is a unique manufacturing technology that aims at fabricating parts that were previously regarded as impossible by other manufacturing techniques. One of the AM techniques that has established itself in the aerospace industry is the laser powder bed fusion technique. However, poor surface roughness and porosity of the as-built components are the limiting factor for this technique. This study carried out an experiment to address these limitations by fabricating overhangs, i.e. parts without any support structures.

Parallelepiped samples were manufactured with inclination angles from 25° to 90° with 5° increment between angles. Samples were built with optimal process-parameters developed by the unique Aeroswift high-speed laser powder bed fusion system. Two directions of scanning were used: parallel-to-powder deposition direction and perpendicularly.

Subsequent to the building process, samples were cut from the base plate and prepared for characterisation. Two surfaces were examined, i.e. downward-facing surface (downskin) and the upward-facing surface (upskin). The surface morphology for the as-built samples were analysed using contact-type surface roughness meter Mitutoyo Surftest SJ-210a, image processing by digital microscope Zeiss Smartzoom 5 and microCT scans by a General Electric VTomeX L240 system. Surface morphology was validated by gathering images and 2D profiles. Statistical analysis includes calculation of average values, standard deviations and Student's t-test for corresponding groups. MicroCT data was visualised and analysed in Volume Graphics VGStudioMax 3.0 to characterise the 3D aerial surface roughness parameters, such as: Sa, Sz, Sq, Ssk, etc. MicroCT scans and optical microscope images of polished cross-sections were used to quantify porosity for different inclination angles.

From the measured surface roughness results, it was determined that roughness is affected by the inclination angle. The downward-facing surface was identified as having the worst surface roughness at low inclination angles (25°–45°). However, surface roughness improved as the inclination angle increased. From the findings it was determined that this was attributed to powder sticking to the surface and stair-

stepping effect. Powder sticking to the surface occurred as a result of the melt pool solidifying on top of loose powder during processing of overhangs. The particles on the surface were clearly visible on the 3D images and SEM images. The level of peaks and valleys was also improved as the angle increased which agreed to the measured results. The cross-sectioning obtained using an optical microscope showed a more rugged profile on downskin surface at low inclination angles.

The reverse occurred on the upskin surfaces: an increased in inclination angle did not yield any improvement in the level of surface roughness. Surface roughness for the upskin surfaces was found to be influenced mostly by stair-stepping effect at low angles and by partially sintered powder particles sticking to the surface at higher inclination angles. This phenomenon resulted in a zigzag curve (roughness data *versus* inclination angle from 25° to 90°). The qualitative images validated this observation as there was no improvement in the amount of roughness on the upskin surface of the samples.

The microCT results and cross-sectional analysis showed that there was no significance difference in the level of near-surface area porosity in the comparison between the inclination angle for the upskin and the downskin surfaces. All the manufactured samples for different inclinations and orientations exhibited porosity levels less than 0.1%.

The scanning direction was found to have an influence on the level of surface roughness. The results showed that surfaces that were created by start-end parts of the tracks with contouring (XZ-orientated samples) achieved better quality than the ones that were created by lateral sides of the tracks with contouring (YZ-orientation). Furthermore, the scanning direction was also observed to affect the level of deformation to the samples. The samples that were scanned along the long side, i.e. YZ-orientated samples, experienced more deformation compared to the ones scanned in the perpendicular direction.

This study concluded that parts can be successfully produced using higher processing parameters. However, lower inclination angles pose a challenge with regard to surface quality of samples. To achieve a better surface quality during production the parts need to be XZ-orientated as described above and inclination

angles less than 45 should be avoided where possible. In addition, it was found that neither the orientation of samples or inclination angle has an effect on the level of porosity when process parameters are properly optimised.

Some promising directions for further investigation of surface characterisation in high-speed LPBF parts based on the study's findings are discussed.

Keywords: Laser powder bed fusion; Ti6Al4V; surface roughness; overhand parts, CT-scans, porosity

Contents

DECLARATION OF INDEPENDENT WORK.....	1
ACKNOWLEDGEMENTS.....	2
ABSTRACT	4
CONTENTS	7
LIST OF FIGURES	9
LIST OF TABLES	12
GLOSSARY	13
CHAPTER 1: INTRODUCTION.....	16
1.1 BACKGROUND	16
1.2 AIMS AND OBJECTIVES.....	18
1.3 OBJECTIVES	18
1.4 RESEARCH QUESTIONS	18
1.5 DELINEATION.....	18
1.6 RESEARCH PROBLEM	19
1.7 SIGNIFICANCE OF THE STUDY	19
SUMMARY	19
CHAPTER 2: LITERATURE REVIEW	20
2.1. ADDITIVE MANUFACTURING	20
2.2. LASER POWDER BED FUSION	21
2.3. LASERS	23
2.4. LASER-MATTER INTERACTION	27
2.5. POWDER PROPERTIES.....	28
2.6. SINGLE TRACK FORMATION IN LPBF.....	30
2.7. LAYER FORMATION IN LPBF.....	32
2.8. 3D PARTS MANUFACTURED BY LPBF	34
2.8.1. <i>Density</i>	34
2.8.2. <i>Residual stresses, cracks and deformations</i>	38
2.8.3. <i>Dimensional accuracy and surface quality</i>	40
2.9. POST-PROCESSING LPBF PARTS	52
SUMMARY	53
CHAPTER 3: MATERIALS AND METHODS	54
3.1. MATERIAL	54
3.2. METHODS	55

3.2.1. CAD software	55
3.2.2. Aeroswift machine.....	55
3.2.3. Mitutoyo Surftest SJ-210.....	57
3.2.4. 3D Zeiss Smartzoom 5	58
3.2.5. Scanning Electron Microscope.....	59
3.2.6. MicroCT.....	59
3.2.7. Statistical analysis.....	60
SUMMARY	60
CHAPTER 4: RESULTS AND DISCUSSION	61
4.1. CHARACTERISATION OF SURFACE ROUGHNESS ON DIFFERENT INCLINATION ANGLES.....	61
4.1.1. 2D surface roughness characterisation.....	61
4.1.2. 3D surface roughness characterisation.....	66
4.2. SURFACE ROUGHNESS AND POROSITY	76
4.3. DEFORMATION OF THE AS-BUILT SAMPLES	80
SUMMARY	83
CHAPTER 5: CONCLUSION AND RECOMMENDATIONS	84
CONCLUSIONS	84
RECOMMENDATIONS FOR FUTURE WORK	85
REFERENCES.....	86
APPENDIX 1. RA: MEASURED SURFACE ROUGHNESS RESULTS (MEAN \pm STANDARD DEVIATION, μM)*	98
APPENDIX 2. RQ: MEASURED SURFACE ROUGHNESS RESULTS (MEAN \pm STANDARD DEVIATION, μM)*	99
APPENDIX 3. RZ: MEASURED SURFACE ROUGHNESS RESULTS (MEAN \pm STANDARD DEVIATION, μM)*	100
APPENDIX 4. PREDICTED VALUES OF THE ROUGHNESS	101
APPENDIX 5. TYPICAL PROFILES OF SURFACE ROUGHNESS RESULTS FOR SET A	102
APPENDIX 6. TYPICAL PROFILES OF SURFACE ROUGHNESS RESULTS FOR SET B.....	107
APPENDIX 7. TYPICAL PROFILES OF SURFACE ROUGHNESS RESULTS FOR SET C.....	112
APPENDIX 8. TYPICAL PROFILES OF SURFACE ROUGHNESS RESULTS FOR SET D	117
APPENDIX 9. POROSITY IN AREAS NEAR DOWNSKIN AND UPSKIN SURFACES IN SAMPLE A.....	122
APPENDIX 10. POROSITY FOR AREAS NEAR DOWNSKIN AND UPSKIN SURFACES IN SAMPLE B.....	129
APPENDIX 11. SEM IMAGES SHOWING THE TYPICAL SURFACES FOR THE DOWNSKIN, TOP AND THE UPSKIN SURFACES	136

List of Figures

Figure 1: Different processing stages for AM [23].....	21
Figure 2: Laser powder bed fusion setup [28].....	22
Figure 3: Laser-based additive manufacturing for material curing or heating: (a) schematic of general 3D printing machines, (b) UV curing process, (c) heating process for sintering or melting [32]..	23
Figure 4: CO ₂ laser: (a) Schematic of a CO ₂ laser, (b) Commercial CO ₂ laser discharge tube [32]. ...	26
Figure 5: Nd:YAG laser: (a) schematic of a Nd:YAG laser, (b) commercial Nd:YAG lasers [32].....	26
Figure 6: Yb-fibre laser: (a) schematic of Yb-fibre laser, (b) commercial Yb-fibre lasers in operation [32].....	27
Figure 7: Schematic plot of the general phenomena in the -PBF AM process [38].	28
Figure 8: Visualisation of the relationships between powder properties, bulk powder behaviour, powder performance in process and finally the manufactured part quality as elaborated by different research groups [41].	29
Figure 9: Top view of single tracks from SS grade 316L powder on steel substrate. Laser power is 50 W, scanning speed is $V = 0.04 \div 0.28$ m/s [48].	30
Figure 10: Tracks from stainless steel grade 904L (-16 μ m) powder with $P/V = \text{const}$ for the corresponding tracks (vectors) [39].	31
Figure 11: Balling effect [53].	32
Figure 12: Hatch distance between two neighbouring tracks (vectors) [39].	33
Figure 13: Different types of scanning strategies (a) unidirectional (b) bidirectional (c) inter-layer and (d) inter-layer rotation strategies [55].	33
Figure 14: Illustration of laser power and the influence on porosity [63].	35
Figure 15: The relationship between scanning speed and relative density [65].	35
Figure 16: The effect of increasing layer thickness on the morphology of thin walls: Laser sintered thin walls from SS grade 316L powder. Thickness of powder layers varied from 40 to 80 μ m with a step of 10 μ m, 20 layers for each thickness, $V = 0.04 \div 0.20$ m/s. Laser power is $P = 50$ W [39].	37
Figure 17: The effect of increasing layer thickness on the level of porosity [46].	38
Figure 18: Temperature gradient mechanism [52].	39
Figure 19: Parts breaking off the supports [16].	40
Figure 20: Different types of supports structures [75].	41
Figure 21: Contact area between part and support structure [74].....	42
Figure 22: Self-detaching of the support structures [74].	43
Figure 23: Cantilever beam with heat support [77]	45
Figure 24: Illustration of best (left) and worst (right) orientations [5]	46
Figure 25: Stair-stepping effect illustration [15].	47
Figure 26: Illustration of the resultant surface roughness (R) for different melt depths for different laser powers [36].	47
Figure 27: Illustration of sloping angles that can build parts with or without supports structures [83].	49
Figure 28: Illustration of unsupported self-supporting parts [84].	49

Figure 29: Graphical illustration of roughness versus angle [14].	50
Figure 30: Solid lines indicating calculated Ra values and dashed line for trigonometric model [88].	51
Figure 31: Illustration of heat flow for two different building angles. The number of attached particles (red spheres) due to heat varies depending on the building angle: (a) 90° building angle; (b) 45° building angle [89].	52
Figure 32: Morphology of Ti6Al4V powder particles.	55
Figure 33: The external structure of the Aeroswift machine.	56
Figure 34: Build layout for samples build.	57
Figure 35: Schematic of surface roughness measuring instrument (a) and Mitutoyo SJ-210 Surftest roughness measurement instrument (b).	57
Figure 36: 3D Zeiss Smartzoom 5 microscope.	59
Figure 37: Schematic representations of MicroCT scan [98].	60
Figure 38: Ra values for downskin surface at different inclination angles.	62
Figure 39: The illustration of stair-stepping effect for different sloping angles.	62
Figure 40: Ra values for the upskin surfaces.	63
Figure 41: Rq values for both (a) downskin and (b) upskin surfaces.	64
Figure 42: Ten-point height (Rz) representation for downskin surfaces.	65
Figure 43: Measured ten-point height values for the upskin surface.	66
Figure 44: MicroCT reconstruction of surfaces versus an inclination angle: set A (a) and set B (b).	68
Figure 45: MicroCT measured root mean square deviation Sq evaluated over surfaces <i>versus</i> inclination angle.	68
Figure 46: Illustration of the scanning strategy for set A (a) and set B (b), red arrows are scanning direction, grey lines are contouring.	70
Figure 47: Ssk evaluated over surfaces versus inclination angle for sets A and B.	71
Figure 48: Maximum height Sz evaluated over surfaces versus inclination angle for sets A and B.	71
Figure 49: Illustration of surface roughness for the downskin surface for angles 25°, 65° & 90° respectively.	73
Figure 50: Illustration of surface irregularities using 3D Zeiss Smartzoom 5 digital microscope for angle 25°, 65° & 90° respectively.	74
Figure 51: SEM images illustrating surface roughness for different inclination angles of 25° (a), 30° (b) and 90°(c) respectively.	75
Figure 52: Optical microscope cross-sections of downskin surfaces for set A at inclinations of 25° (a), 55° (b) and 90° (c) respectively.	76
Figure 53: Optical microscope cross-sections of downskin surfaces for set B at inclinations of 25° (a), 55° (b) and 90° (c) respectively.	77
Figure 54: Defect analysis of near-upskin (left) and downskin (right) by CT scans.	78
Figure 55: Porosity and maximum pore size for near-downskin areas for samples A and B.	79
Figure 56: Porosity and Rq surface roughness for samples A and B.	79
Figure 57: Cross-sections of sets A and B at inclinations of 25° (a) and 55° (b) respectively.	80

Figure 58: MicroCT scans of LPBF samples manufactured at different inclination angles versus designed shape coded with blue colour, from left to right – set A: 25–55° (a), 60–90° (b); set B: 25–55° (c), 60–90° (d)..... 82

List of Tables

Table 1: Lasers in various commercial 3D printing machines [32]	24
Table 2: Absorptivity of various materials in a loose powder state at the operating wavelength of Nd:YAG and CO ₂ lasers [32].....	25
Table 3: Ti6Al4V chemical composition (wt.%).....	54
Table 4: Area roughness of downskin surfaces as per CT scans	69

Glossary

3D	Three dimensional
AM	Additive manufacturing
ASTM	American Society for Testing and Materials
CAD	Computer-aided design
CRPM	Centre for Rapid Prototyping and Manufacturing
CSIR	Council for Scientific and Industrial Research
CT	Computer tomography
DfAM	Design for additive manufacturing
DMLS	Direct metal laser sintering
LPBF	Laser powder bed fusion
PBF	Powder bed fusion
R&D	Research and development
SEM	Scanning electron microscope
STL	Stereolithography

Nomenclature for roughness values

R_a	Arithmetic average height
R_z	Ten-point height
R_q	Root mean square
S_a	Arithmetic mean height
S_z	Maximum height
S_q	Root mean square height
S_p	Maximum peak height
S_v	Maximum valley depth
S_{sk}	Skewness

Publications

- M. Shange, I. Yadroitsava, S. Pityana, I. Yadroitsev, D. Bester. Surface morphology characterisation for parts produced by the high-speed selective laser melting. Conference of the South African Advanced Materials Initiative (CoSAAMI 2019). IOP Conf. Series: Materials Science and Engineering 655 (2019) 012045. IOP Publishing, doi:10.1088/1757-899X/655/1/012045.
- M. Shange, I. Yadroitsava, S. Pityana, I. Yadroitsev, A. du Plessis. Determining the effect of surface roughness and porosity at different inclinations of LPBF parts. Proc. of RAPDASA-2019 conference: 5-9 November 2019, Central University of Technology, Bloemfontein, South Africa, pp. 40-51. ISBN 978-0-6398390-0-4.
- D.C. Bester, M. Shange. Design for additive manufacturing: an introduction to design rules and constraints for high speed SLM. Proc. of RAPDASA-2019 conference, 5-9 November 2019, Central University of Technology, Bloemfontein, South Africa, pp 413-420. ISBN 978-0-6398390-0-4.

CHAPTER 1: Introduction

1.1 Background

Additive manufacturing (AM) or 3D printing is a disruptive technology which is envisaged to play a key role in sectors such as automotive, aerospace, medical industries, etc. [1], [2]. The advantages of adopting AM are time- and cost savings on material, processing and tooling [3]. These savings will enable companies to produce parts at relatively competitive prices in short timeframes [1]. It has also been stated that the adoption of AM will eliminate product obsolescence which will prolong the product lifecycle [2].

In South Africa, this technology took off a decade later than the international community [4]. Despite this late start, a team of researchers from Council of Scientific and Industrial Research (CSIR) in collaboration with Aerosud and the South African Department of Science & Technology have developed the largest AM laser powder bed fusion machine (LPBF) for producing complex metal aircraft parts called Aeroswift. This platform is the fastest in the world in terms of production speed and lead time to market. The Aeroswift was designed to print objects of up to 2000 mm × 600 mm × 600 mm and uses a laser with a maximum power of 5 kW. These features make this AM system unique compared to the existing available commercial systems that produce parts at relatively lower speeds. This consortium was formed to exploit and utilise the abundant mineral resources in the country, such as the raw material that can produce titanium alloys used for aerospace components. Furthermore, by having the largest 3D printing machine the country will gain a competitive advantage [1].

An industry such as aerospace has high-performance requirements with its current rather low scale of manufacturing. AM is very suitable for production parts with optimum strength-to-weight ratio. This can be achieved by redesigning the parts and meeting the functional requirements while reducing material volume. However, sceptics of AM have hindered the progress towards the adoption of this technology [1]. The reasons for the mistrust and resistance to the technology range from the speed of the AM process, to quality and reliability of the produced parts.

It is known that some inclination angles necessitate the need of support structures for the LPBF process. During the laser printing process, the laser beam selectively melts the metal powder track by track, layer by layer, according to the designed computer-aided design (CAD) file. The laser intensity exceeds the melting point of the material in order to melt the powder material and previously sintered layer (substrate). The layer-by-layer nature of manufacturing, high temperature gradients and cooling rates lead to high stresses and risk of distortions: parts might lose dimensional stability, have porosity and high roughness. Support structures are used to eliminate overhanging: they act as anchors, serving as heat dissipators and prevent thermal warping of the parts. However, excessive utilisation of support structures has a direct implication on material cost, build time, removal and also high roughness after support removal [5].

The number of support structures required to anchor the part is determined by the way in which a part is orientated during the production or printing process [5]. This means that optimising part orientation in order to use fewer support structures will improve the post-processing activities. Therefore, designers for AM are required to consider the production time, amount of material and how to build and remove support structures [6]. It is advisable to consider what the effect of removing the support structures would be with regard to part quality [5], [7]. Furthermore, it is also recommended that designers minimise or eliminate the amount of overhanging surface that needs to be supported during the design stage [8], [9], [10]. This will lead to the design of completely self-supporting objects which can eliminate the need for support structures [11], [12], [13] and specifically, the design of objects where all features do not exceed the minimum allowable self-supporting angle [14].

Previous studies have highlighted that building self-supporting parts minimises the building of support structures on angled surfaces [15]. It has also been reported that self-supporting components that have an angle less than 30° towards the build plate require support structures and an angle greater than 30° can be built without support structure. However, parts produced with angles less than 45° possess poor surface quality due to heat accumulation that results in powder agglomeration on the underside [16]. Furthermore, in [14], it was stated that a phenomenon called the stair-stepping effect contributes to poor surface roughness and becomes more

pronounced at angles lower than 45° . In addition, it has also been reported that by determining the minimum support angle, the use of a solid support structure is not required up to a certain point, which adds to a more effective post-manufacturing process [17].

This study aims to build a self-supporting test artefact and characterise the resulting surface quality on different inclination angles. This will be achieved by building a benchmarking test artefact with different inclination angles which will help design engineers understand the performance of the Aeroswift platform, by building without the use of support structures when creating new components.

1.2 Aims and objectives

The aim of this research is to build test artefacts to characterise surface roughness and porosity and to determine the minimum angle for building without support structure from Ti6Al4V powder using the Aeroswift platform.

1.3 Objectives

- To fabricate self-support structures using the high-speed Aeroswift machine.
- To determine the minimum angle so as to characterise various surface morphologies and porosity of different overhangs for different angles.

1.4 Research questions

- What is the relationship between roughness and inclination angle?
- What is the effect of scan orientation on surface roughness and porosity?
- What is the effect of inclination angle on porosity?

1.5 Delineation

All test specimens were produced using Ti6Al4V powder. The study focused on analysing surface roughness for as-built samples without conducting any post-processing to the parts. The roughness variables that were analysed are: arithmetic average height (R_a), ten-point height (R_z), root mean square (R_q), arithmetic mean height (S_a), maximum height (S_z) root mean square height (S_q) and skewness (S_{sk}) for both the downward and the upward surfaces.

1.6 Research problem

It is well known in literature that fabricating self-supporting objects using non-optimal parameters leads to the formation of unwanted defects such as porosity and poor surface quality. In SLM, fabricating parts with defects is associated with cost implications. However, there are other underlying challenges, such as porosity and surface roughness for different inclination angles, which have not been fully highlighted by other scholars.

Poor surface roughness necessitates posts-processing and increases the cost to produce components. In addition, surface roughness in AM is known to be the main contributor to pores and micro-cracks. Furthermore, surface roughness also reduces the dimensional stability of the parts produced by the Aeroswift machine. This study seeks to conduct an in-depth analysis of the surface roughness for parts produced on the high-speed laser powder bed fusion machine.

1.7 Significance of the study

At the conclusion of this thesis, new information will be added to the pool of knowledge as researchers and design engineers will understand the limitations of parts built using high-power laser and higher scanning speeds especially using the Aeroswift platform.

Summary

AM is the future manufacturing technology and features that emanate from this technology need to be studied and evaluated. Therefore, design engineers need to understand implications such as building with or without a support structure. The effects of process restrictions, such as poor surface quality on self-supporting objects, need to be studied and understood. Surface roughness arising from self-supporting parts need to be defined for the high-speed Aeroswift machine. Furthermore, the determination of these limitations will enhance the development of additive manufacturing as an alternative means of production technology.

CHAPTER 2: Literature review

This chapter looks at the fundamentals of the AM process and concludes by discussing the effects associated with surface roughness on the additively manufactured parts. This is achieved by discussing the previous works that have been studied by other scholars in the field of additive manufacturing.

2.1. Additive manufacturing

ASTM F2792 describes additive manufacturing (AM) as the method of joining materials to create parts from 3D model data, usually a layer-wise process, in contrast to traditional manufacturing practices [18]. Furthermore, it is called an additive manufacturing process in the sense that the material is added whereas the process of forming parts by casting is called the formative process [19]. Forming parts by material removal is called subtractive manufacturing [20].

AM, as a result of its layer-manufacturing technology, is capable of fabricating complex profiles created using a CAD file [21]. The main advantage of adopting AM technology is that there are no added costs accumulated when fabricating complex shapes as there is no need for special tooling, refitting, improved operator proficiency or even production time [3]. Moreover, this technology enables the manufacturing of complex profiles that would require numerous parts if manufactured by traditional techniques [22]. A step-by-step AM process is illustrated in Figure 1 below, from inception to completion. The process starts by drawing a three-dimensional computer-aided model which is converted to a stereolithography (.STL) file, then sliced into layers before being transferred to the machine for printing.

AM, also previously known as rapid prototyping, was the earliest method developed in the 1980s and achieved popularity in the 2000s as a layer-by-layer manufacturing technique [24]. The term “rapid prototyping” was previously used to describe technologies which created objects directly from three-dimensional information. AM has evolved from rapid prototyping where it was only used to fabricate prototypes, due to its capability to manufacture objects directly from computer-aided drawings [25].

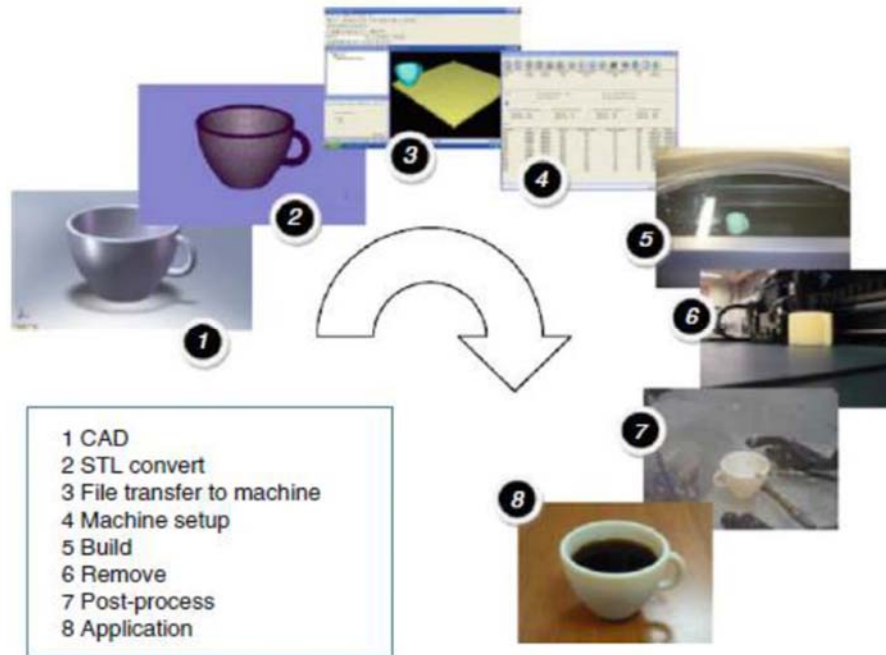


Figure 1: Different processing stages for AM [23].

AM technology incorporates several manufacturing techniques that produce objects layer by layer [2]. These manufacturing techniques are divided into seven distinct categories according to ASTM F2792 standard, namely, powder bed fusion, vat photopolymerisation, binder jetting, material jetting, sheet lamination, direct laser deposition and material extrusion. Furthermore, various feedstock materials determine the type of AM process to be used. These materials are metallic, polymer, sand, ceramic, etc. and are available in different forms such as filaments or liquids, powders, wires, etc. [22]. The aforementioned AM processes build and consolidate layers in different ways; however, different processed parts can vary significantly [26]. The various manufacturing techniques enable diverse differences in surface finish and geometric tolerance of parts [22]. However, this study is only limited to powder bed fusion – laser powder bed fusion process.

2.2. Laser powder bed fusion

Laser powder bed fusion (LPBF) is an AM technique that entails the process of melting deposited layers of powder into a solid object using laser energy [27]. The illustration of an LPBF process is shown in Figure 2 which starts by depositing a thin layer of powder onto the base plate (substrate). The laser beam then scans the

powder bed based on the CAD drawing's sliced information, inducing high laser energy to melt the powder and the substrate. The layer-by-layer consolidation is repeated until the part is complete [28]. The LPBF process apparatus comprises a laser system, a roller/scrapper powder deposition system, a computer for process control, an inert gas protection system and heaters for pre-heating the bed [28]

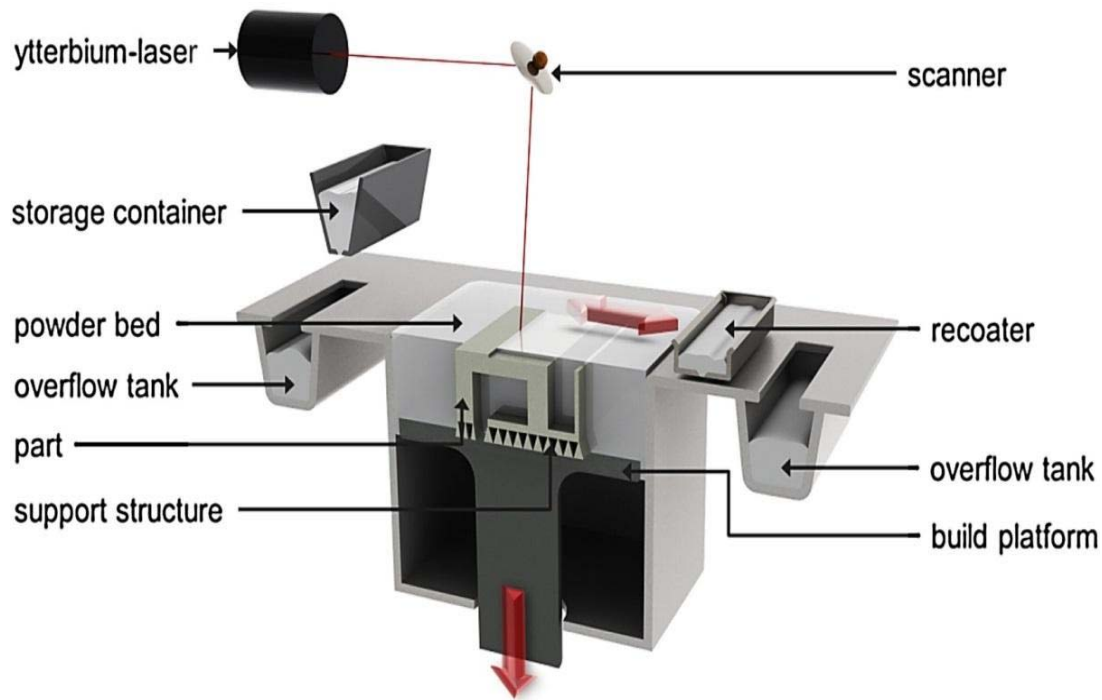


Figure 2: Laser powder bed fusion setup [28].

The laser powder bed manufacturing process is a process capable of fabricating objects with high precision and good surface integrity [25]. By optimising LPBF input parameters, fully dense objects can be produced with mechanical properties corresponding or even higher than those created by traditional methods [15]. Furthermore, this technology uses standard metallic powders which melt completely ensuring mechanical properties match 100 percent density or even beat conventional techniques [29].

Although LPBF technology is presented as being capable of printing any shapes, it has been argued that it is not entirely correct. The LPBF fabrication process necessitates support structures during the production [20], [30]. The inclusion of support structures is the main setback in LPBF as these objects are made sacrificial and their removal adds to the cost of post-processing [27]. During the LPBF,

fabricated parts must be sufficiently anchored otherwise quality cannot be guaranteed [22]. However, the amount of material wasted on fabricating support structures affects manufacturing costs especially when high-value metals, such as titanium alloy, are used in the production of aerospace components [5].

2.3. Lasers

Light Amplification by Stimulated Emission of Radiation or commonly known as “laser” is an instrument that regulates the way that energised atoms release photons. Three techniques that use laser in the AM process are powder bed fusion, direct energy deposition and vat photopolymerisation (Figure 3) [32].

Lasers used in modern commercial AM machines are presented in Table 1. The rated power for the laser used in AM varies from 1 W up to 4–6 kW with a wavelength from 354.7 nm to 10.6 μm [31]. In AM, wavelength is one of the key variables to be considered as a result of different material absorption (Table 2) at different wavelengths [33]. More frequently, three different types of lasers are used for AM processes that include fibre, CO₂ and Nd: YAG laser systems [34].

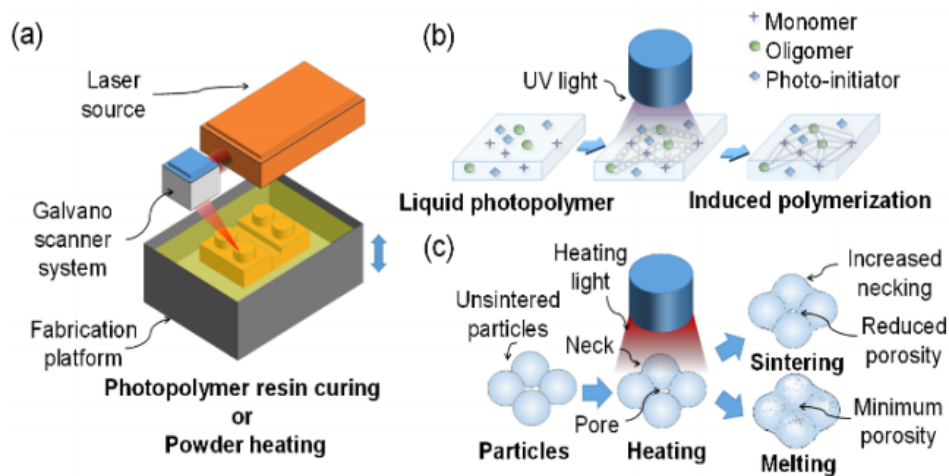


Figure 3: Laser-based additive manufacturing for material curing or heating: (a) schematic of general 3D printing machines, (b) UV curing process, (c) heating process for sintering or melting [32].

Table 1: Lasers in various commercial 3D printing machines [32]

Company	System	Process	Power	Laser type
Photopolymer resins				
3D Systems	ProX series	SLA	up to 1.45 W	Nd:YVO4 laser
CTC	Riverbase500	SLA	300-500 mW	Nd:YVO4 laser
Polymer powders				
3D Systems	sPro series	SLS	30-230 W	CO ₂ laser
EOS	EOSINT P series	SLS	50 W	CO ₂ laser
Metal powders				
3D Systems	ProX DMP series	DMP/SL M	500-1000 W	Yb-fibre laser
SLM Solutions	HL series	SLM	400-1000 W	Yb-fibre laser
Optomec	LENS series	LENS/D MD	400-1000 W	Yb-fibre laser
EOS	EOS M series	DMLS	200-400 W	Yb-fibre laser
Matsuura	LUMEX Avance series	DMLS/Milling	400-1000 W	Yb-fibre laser
Concept Laser	LaserCUSING series	SLM	100-1000 W	Yb-fibre laser
Metal wire				
Irepa Laser	EasyCLAD MAGIC LF6000	LC	750-4000 W	Yb-fibre laser
Huffman	H series	LC	400 W	Yb-fibre laser

Table 2: Absorptivity of various materials in a loose powder state at the operating wavelength of Nd:YAG and CO₂ lasers [32]

Material	Nd:YAG laser (1.06 μm)	CO ₂ laser (10.6 μm)
<i>Metals</i>		
Cu	59%	26%
Fe	64%	45%
Sn	66%	23%
Ti	77%	59%
Pb	79%	-
<i>Ceramics</i>		
ZnO	2%	94%
Al ₂ O ₃	3%	96%
SiO ₂	4%	96%
SnO	5%	95%
CuO	11%	76%
SiC	78%	66%
Cr ₃ C ₂	81%	70%
TiC	82%	46%
WC	82%	48%
<i>Polymers</i>		
Polytetrafluoroethylene	5%	73%
Polymethylacrylate	6%	75%
Epoxy polyether-based polymer	9%	94%
<i>Mixtures</i>		
Cu-10Al (wt%)	63%	32%
Fe-3C-3Cr-12V+10Ti(wt%)	65%	39%
Fe-0.6C-4Cr-2Mo-1Si15+TiC(wt%)	71%	42%
Fe-1C-14Cr-10Mn6Ti+66TiC(wt%)	79%	44%

CO₂ lasers (Figure 4) are regarded as low-power systems; therefore, operating cost is low compared to other types of lasers [32], [35]. The advantage of using CO₂

lasers is that they can be easily scaled up to 20 kW, but the most common is the 3 kW. CO₂ lasers have a wavelength of 10.6 μm which results in higher reflectivity and can reduce the effect on metal processing. For higher conductivity metals it is recommended to use lasers with shorter wavelength [33].

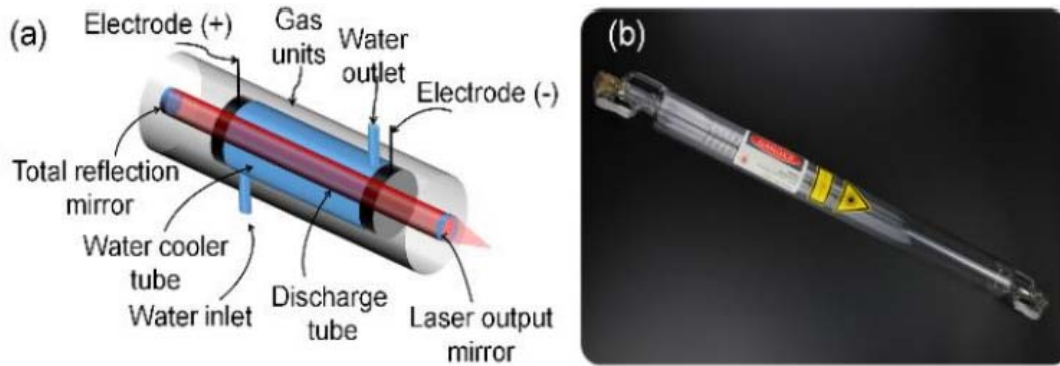


Figure 4: CO₂ laser: (a) Schematic of a CO₂ laser, (b) Commercial CO₂ laser discharge tube [32].

Yttrium aluminium garnet (YAG) hosts the Neodymium (Nd³⁺) ion due to its thermal, optical and mechanical properties (Figure 5). Nd: YAG laser has an increased processing efficiency compared to CO₂ lasers with the same power [35]. Also, another advantage of Nd: YAG over CO₂ includes the ability to deliver laser radiation through fibres. The basic wavelength for Nd: YAG laser is 1064 nm, second-harmonic is 532 nm (green laser) and third-harmonic at 355 nm is UV laser [35].

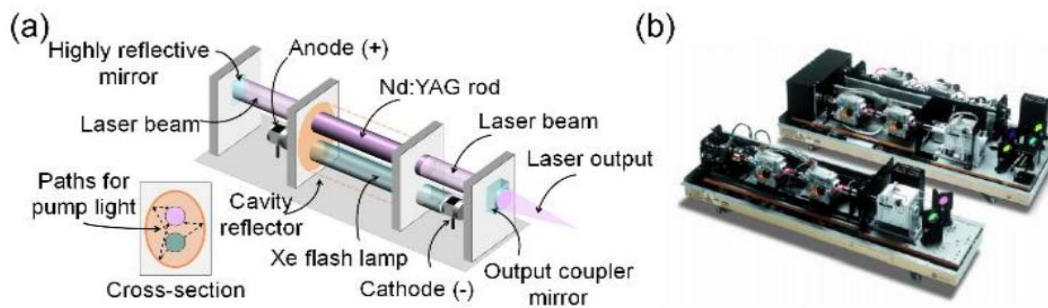


Figure 5: Nd:YAG laser: (a) schematic of a Nd:YAG laser, (b) commercial Nd:YAG lasers [32].

Fibre lasers (Figure 6) are the most commonly used type of laser due to their limitless advantages over the other types of lasers [34]. Fibre lasers possess good beam quality, compact design and high power. The limitation of using this type of

laser is the fairly high operational price. The wavelength for Yb-doped fibre laser is 1030–1070 nm.

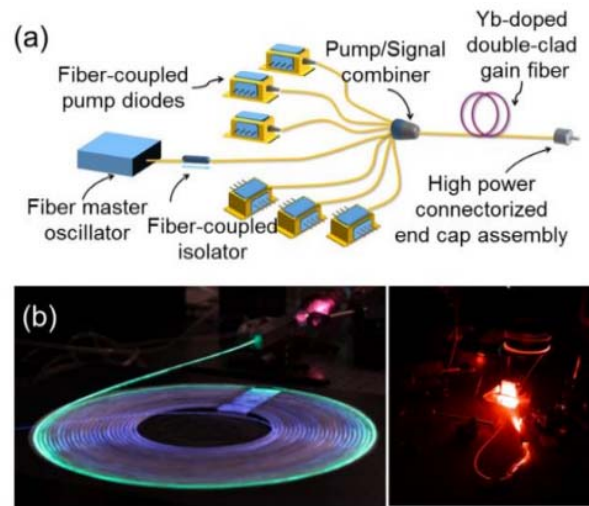


Figure 6: Yb-fibre laser: (a) schematic of Yb-fibre laser, (b) commercial Yb-fibre lasers in operation [32].

2.4. Laser-matter interaction

During the laser processing in LPBF, the powder material is superheated and melts to form a liquid pool known as the melt pool which solidifies and cools down rapidly [36]. The melt pool is the start of the solid part. Furthermore, the melt pool enlarges with increasing laser power. Figure 7 below summarises general phenomena at the interaction zone between a laser source and powder material. When the powder bed surface is irradiated by a laser beam, heat can be dissipated by convection and radiation. Subsequently, substrate and powder materials absorb the remaining laser energy through conduction.

The transient phenomena in the melt pool include the morphology of the surface and temperature and wetting behaviour, which are of paramount importance in obtaining optimum mechanical properties [37]. The processing parameters that influence the laser melting processes are laser power and spot size, time of irradiation, layer thickness and scan spacing (hatch distance). These parameters together with material properties individually or collectively influence the various physical

phenomena such as heat conduction, energy penetration, radiation, capillary forces, melting/solidification, wetting, distortion, Marangoni effect, humping, balling, etc.

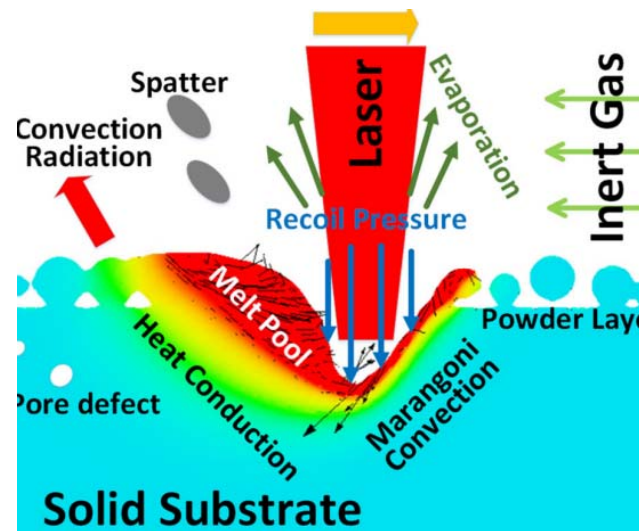


Figure 7: Schematic plot of the general phenomena in the -PBF AM process [38].

2.5. Powder properties

Powder particle size and morphology are the key elements that influence LPBF part quality (Figure 8) [39], [40], [41]. The spherical morphology and smooth surface of the powder particles result in a good flowability and homogeneous layer distribution [39]. In the LPBF process, good powder flowability is required to achieve uniform thickness of powder layers, which allows uniform laser energy absorption in the processing area [43]. It has been shown that powder with lower particle size has lower flowability [39]. However, absorptivity of the powder bed diminished with increasing particle size [42]. Also, the spot size of the laser beam and time of irradiation (scanning speed) influence the geometry and morphology size of the tracks [39]. So, molten pool temperature, flows inside molten pool, its stability and size will be different for powders with various particle size distribution. All these factors can influence single track formation and properties of 3D parts. But to date, comprehensive correlation between powder properties, powder in-process behaviour and bulk properties of sintered materials have not yet been identified. New characterisation methods for powder qualification and process-parameters, exclusively designed for the specific PBF process, have to be elaborated [41].

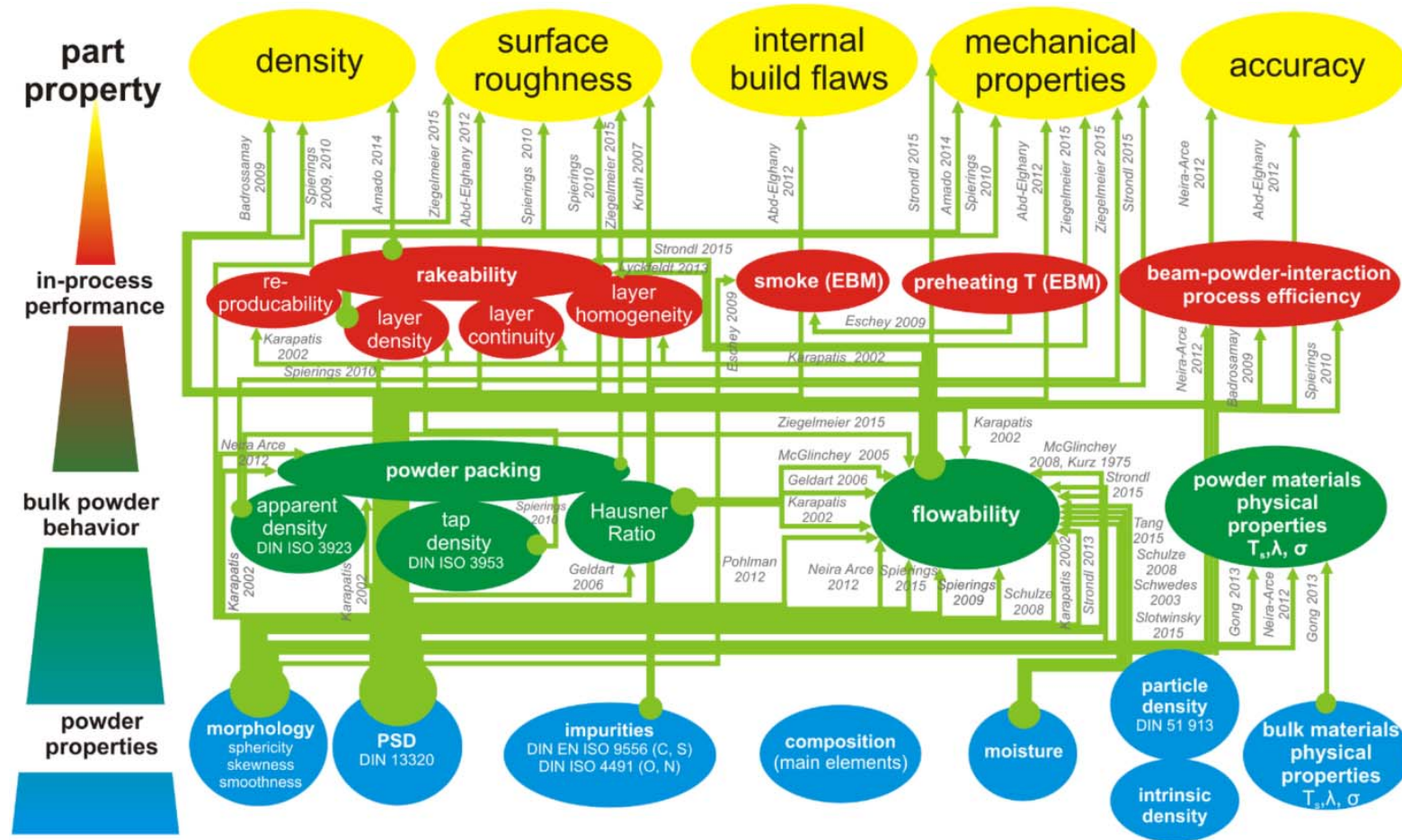


Figure 8: Visualisation of the relationships between powder properties, bulk powder behaviour, powder performance in process and finally the manufactured part quality as elaborated by different research groups [41].

2.6. Single track formation in LPBF

The main objective of LPBF is to create parts that are fully dense with minimal defects. The full melting mechanism for the LPBF process influences the melt pool stability and leads to parts defects if process parameters are not properly selected [45]. Process parameters include laser power, spot size and shape, scanning speed, powder layer thickness, powder bed preheating temperature, hatch distance, *etc.*

The laser power settings and scanning speeds have the most significant effect on producing dense objects [44]. However, defects such as pores, cracks or distortions as a result of rapid phase transformation of the LPBF process might occur if process parameters are not properly selected. In addition, scanning speed and laser power also influence the energy density and temperature distribution of each molten layer. Careful control of the LPBF processing parameters is required in order to avoid defect formation in the melt pool [46], [47], [49]. The properties of parts produced by LPBF mostly depend on the quality of each single line and each track [48]. Single tracks play an important role in parameter optimisation. This can be achieved by examining the shape and the microstructure of the single tracks which can provide useful information for developing a comprehensive strategy to manufacture LPBF parts with tailored microstructure and mechanical properties [45]. A balance of parameters between the scanning speed and powder layer thickness have to be determined in order to melt the base plate and create a joint melt pool and stabilising effect of the contact zone (Figure 9) [48].

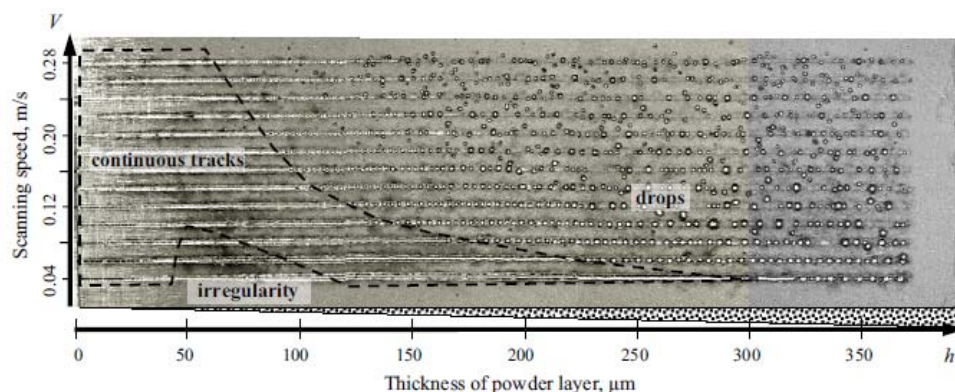


Figure 9: Top view of single tracks from SS grade 316L powder on steel substrate. Laser power is 50 W, scanning speed is $V = 0.04 \div 0.28$ m/s [48].

It has been reported that when keeping the laser power constant and increasing scan speed, the scan tracks become irregular and a further increase in speed consequently results in the formation of balling effect [39], [51] as shown in Figure 10. The high scanning speed results in the formation of small liquid droplets on the surface due to instability of molten metal pool [39], [48], [51].

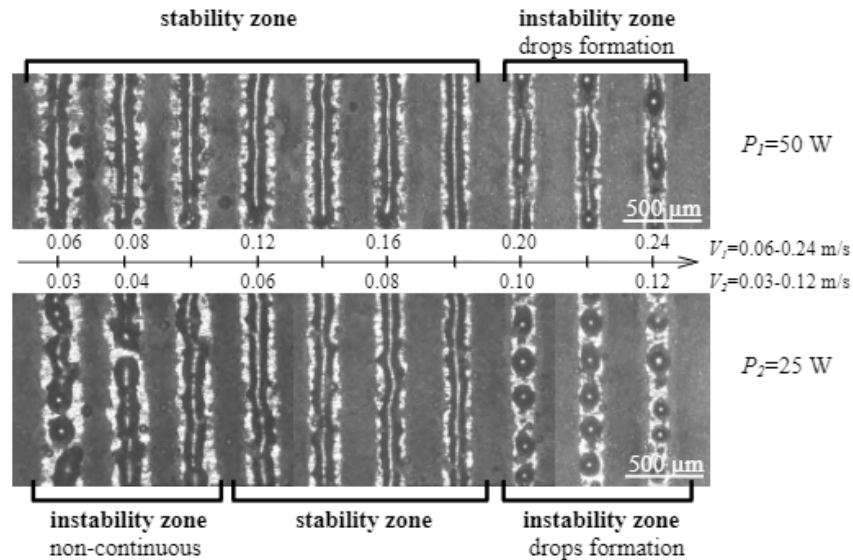


Figure 10: Tracks from stainless steel grade 904L (-16 μm) powder with $P/V = \text{const}$ for the corresponding tracks (vectors) [39].

The balling effect is defined as a result of high-temperature gradient between different volumes of molten material which generates surface tension within the melt pool and droplets are formed. A balling effect, as a result of breakage of melt pool during laser scanning, results in beads instead of continuous track [14]. The resulting product of a severe balling effect is poor surface quality due to an uneven layer-by-layer deposition (Figure 11), and as result, low density of 3D LPBF objects.

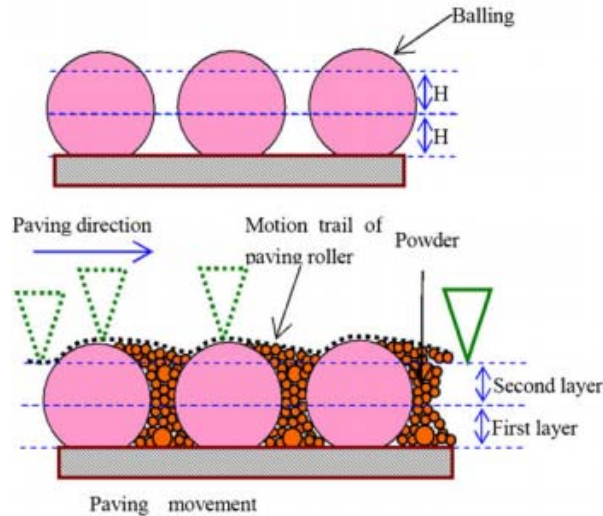


Figure 11: Balling effect [53].

The powder layer thickness selected impacts on the stability of the molten pool [45]. Thinner layer thickness increases the wetting ability between the molten pool and the substrate due to improved melt pool stability resulting in less balling effect. It has been suggested that a thin layer thickness ensures finer particle sizes and facilitates a more complete melting process due to the higher surface-to-volume ratio compared to a thicker layer thickness [47].

2.7. Layer formation in LPBF

LPBF process entails the melting of tracks and layers which join with one another to form a solid object. Process parameters, such as hatch spacing (distance) or scan spacing (Figure 12), determine the overlapping between neighbouring tracks in order to form a dense layer [49]. A higher building rate in LPBF can be attained by increasing hatch spacing [53]. However, further increasing the hatch spacing causes porosity [39], [47], [54]. LPBF uses manufacturing patterns (scanning strategies) including parallel, zigzag, spiral, chessboard (island), stripes, and paintbrush (Figure 13). Also, different strategies can be used for different layers and parts of the 3D object. The aforementioned scanning strategies are used to control the temperature gradient inside the part, to avoid consolidation problems and to decrease porosity, to avoid overheating near the sides of the LPBF parts, to decrease or disorientate residual stresses, to improve surface finishing, etc. [55], [56], [57].

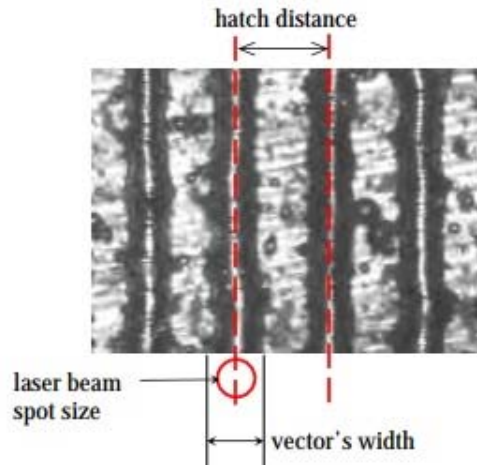


Figure 12: Hatch distance between two neighbouring tracks (vectors) [39].

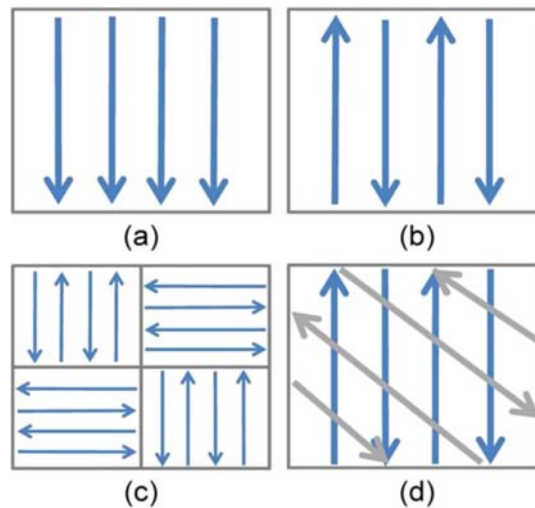


Figure 13: Different types of scanning strategies (a) unidirectional (b) bidirectional (c) inter-layer and (d) inter-layer rotation strategies [55].

Laser re-melting is used during or after the laser melting process to overcome process limitations such as high surface roughness and porosity [59]. This process is achieved by scanning the same sliced layer before putting down a new powder layer. Laser re-melting has been reported to be a key to improving surface quality for the external surface without applying any surface modification technologies such as applying mechanical, chemical and thermal processes. The advantage of re-melting parts is that it can be applied to inclined or curved surfaces. Laser re-melting has also been reported to reduce the residual stresses in the top layer by about 55% when optimal process-parameters in re-scanning are selected [59]. However, laser

re-melting results in an increase in the production time depending on the selected scan speed and scan spacing.

2.8. 3D parts manufactured by LPBF

2.8.1.Density

Industrial applications require reliable mechanical properties of parts, so the density of LPBF parts is extremely important. LPBF can produce parts with densities of 98% and higher. Porosity has a negative effect on the mechanical properties of the parts and can act as stress concentrators which may lead to premature plasticity and localised strain. The mechanical behaviour of a material is directly affected by the morphology and distribution of pores [60], [61]. Where a fatigue crack is introduced to the surface or subsurface, the crack will grow and spread from one pore to the other, using pores as linkages [62]. It has also been reported that poor surface quality contributes to the formation of pores which may lead to structural weakness under stress combined with surface roughness. In addition, parameters such as scanning speed and laser power have the greatest influence on the melt pool; therefore, they have more effect on the level of porosity [46].

Du Plessis [63] reported that with low laser power and keeping a constant spot size, scanning speed and powder layer thickness, porosity will be very high due to lack of fusion. At optimal process parameters, porosity will be minimal. Further increase in laser power results in the formation of keyhole-type pores (Figure 14). This has been attributed to higher laser power which creates deeper melt pool, thus causing entrapment of vapours.

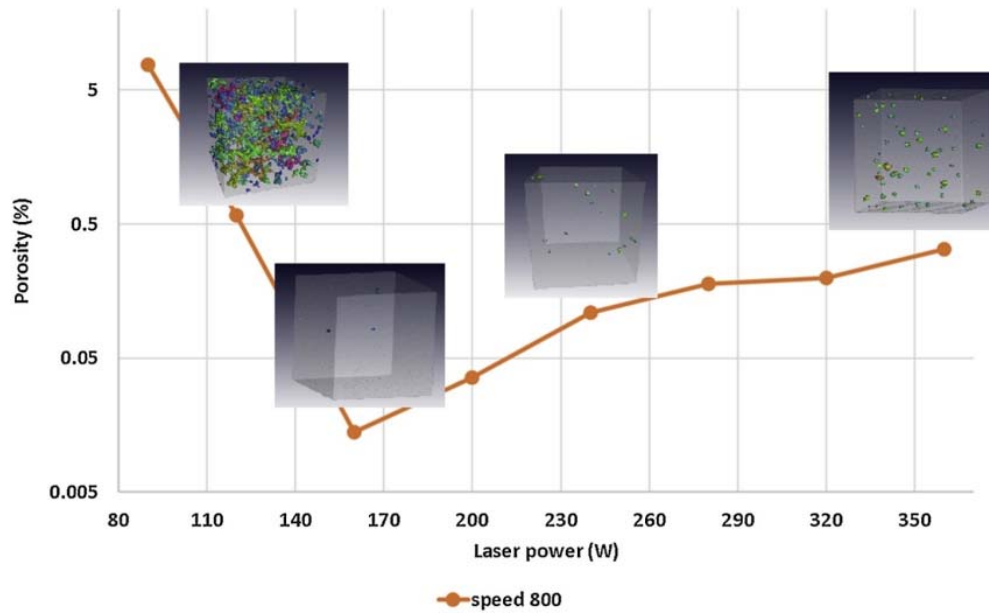


Figure 14: Illustration of laser power and the influence on porosity [63].

An increase in scanning speed results in increasing build rate in the LPBF process. However, the increasing scan speed is only applicable up to a certain limit [64]. Qiu et al. [65] reported that for Ti6Al4V powder at fixed laser power of 400 W and a fixed powder layer thickness (20 μm), increasing the scanning speed above 2.7 m/s results in an increase in porosity fraction (Figure 15). It must be noted that samples were produced by Concept Laser M2 Cusing SLM system.

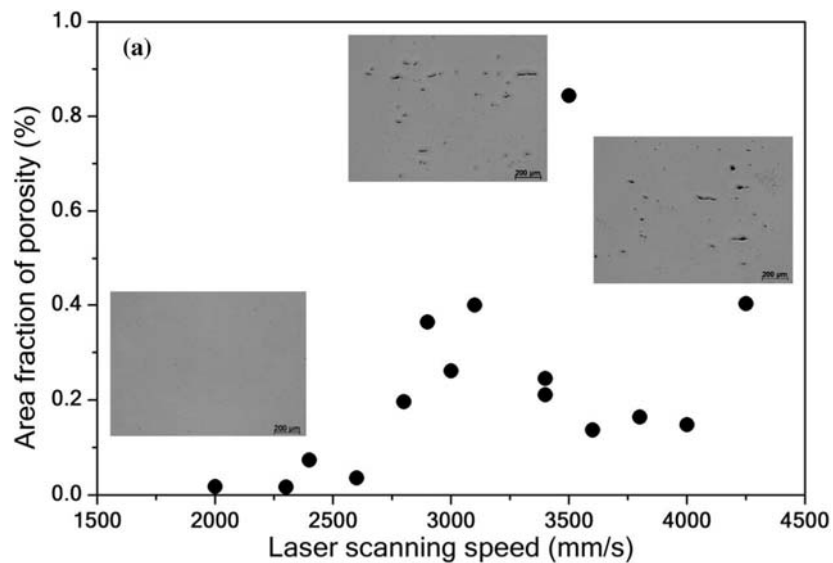


Figure 15: The relationship between scanning speed and relative density [65].

Short interaction time at high scanning speed leads to high temperature gradients and significant flows in the molten pool: it becomes unstable and tracks are irregular, thus leading to the formation of pores.

Studies have reported that the level of porosity is also influenced by hatch spacing. The increase in hatch spacing leads to an increase in the level of porosity [66]. This was found to be attributed to the track overlapping. In addition, when increasing the hatch spacing led to less overlap, this resulted in lack of fusion between the layers [63]. Hatch distance depends on geometrical characteristics of single tracks, that in turn depend on laser spot size, laser power, scanning speed (interaction time) and material properties [66]. It is recommended to use thinner layer thickness when building with larger hatch spacing in order to attain both intra-layer and inter-layer overlap [67].

The powder layer thickness selected affects the level of porosity of LPBF-manufactured parts. It has been reported that increasing the size of the layer thickness led to an increase in size of pores [39], [46] as shown in Figure 16. When keeping process parameters and increasing layer thicknesses, joint molten pool (powder + substrate) became shallower resulting in the formation of pores Figure 17 [39], [65].

Porosity, caused by lack of fusion due to non-optimal energy input for the selected layer thickness, occurs as a result of the non-melted powder inside pores [46]. Regularly spaced porosity was also found when too large a hatch distance was used [68]. Thus, powder material, powder layer thickness and process parameters, such as laser power, spot size, scanning speed, hatch distance and scanning strategy, are the main factors that define density of LPBF parts.

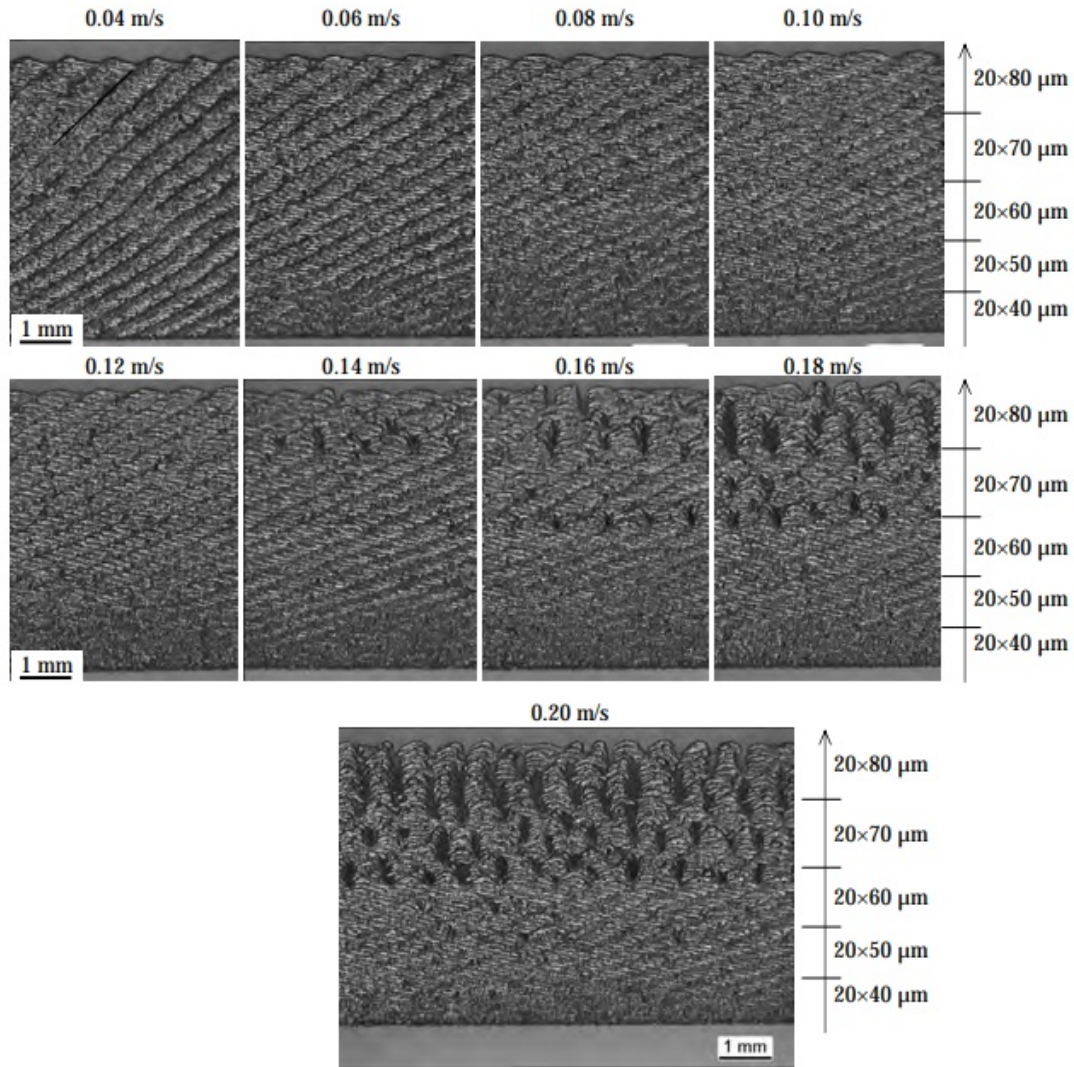


Figure 16: The effect of increasing layer thickness on the morphology of thin walls: Laser sintered thin walls from SS grade 316L powder. Thickness of powder layers varied from 40 to 80 μm with a step of 10 μm , 20 layers for each thickness, $V = 0.04\div 0.20$ m/s. Laser power is $P = 50$ W [39].

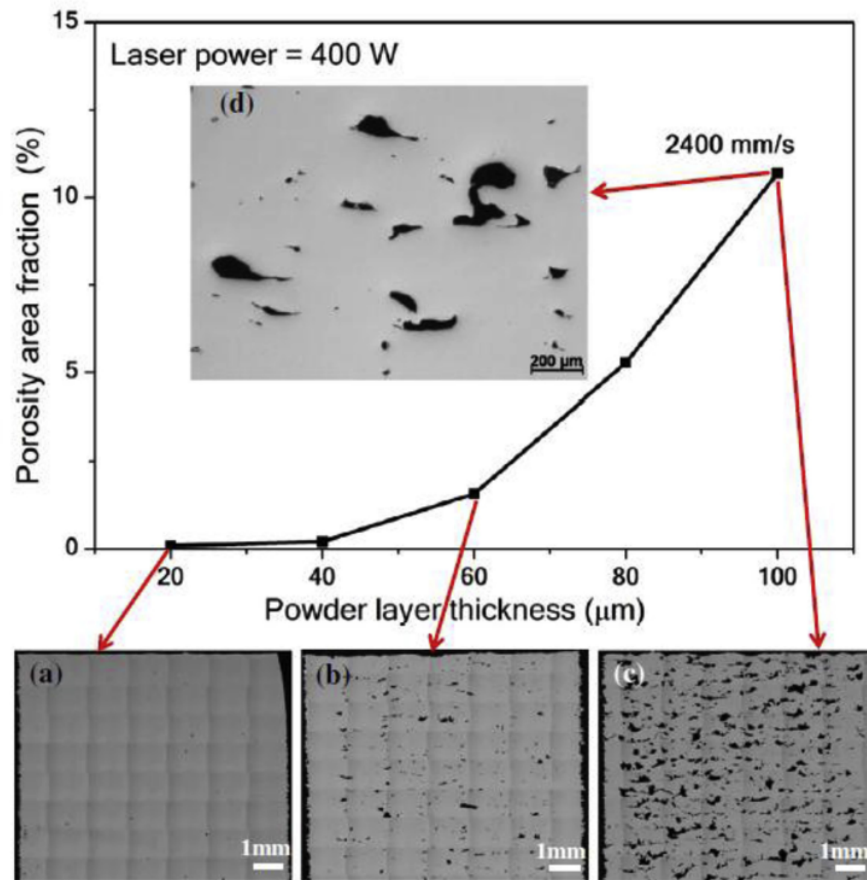


Figure 17: The effect of increasing layer thickness on the level of porosity [46].

2.8.2. Residual stresses, cracks and deformations

The fabrication process in LPBF is divided into two phases – heating and cooling [69]. When the laser beam leaves the irradiated zone, the molten pool begins to solidify and cool down immediately as shown in Figure 18. Different layers of material cool at different rates; this means that the contraction occurs at different speeds causing the plastic flow. Laser processing of new tracks and layers will cause stresses and deformations near the molten pool creating a complex superposition of strains and stresses. Plastic deformations in the surrounding material and in the solidifying track occur as a result of lowered yield strength at the elevated temperature. Thus, non-uniform deformation of the material results in residual stress being present in the LPBF part.

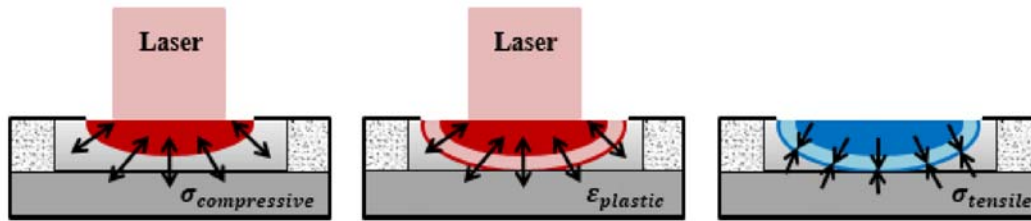


Figure 18: Temperature gradient mechanism [52].

Previous studies have indicated that thermal gradients within the layers arise due to LPBF [21]. Melting tracks are formed when the laser irradiates the powder bed, resulting in shrinkages along the scanning direction. The shrinkage compensation is insufficient for excessively long scanning tracks which results in the formation of high tensile residual stresses. Consequently, cracks or disconnections of the part from the substrate (Figure 19) occur as a result of residual stresses [71].

To mitigate defects in LPBF, it is recommended incorporating support structures to fabricate metal objects to minimise geometric distortions and reduce temperature gradients [17]. The primary function of support structures is to dissipate heat away from the newly melted layers of the part; however, there is less heat dissipated when no solid material is available. However, it is argued that there is no guarantee that a part will not deform by the introduction of supports structures, as geometries that are susceptible to residual stresses can break off from the support structures causing the part failure [72]. In addition, a part can still warp even after support removal due to remaining stresses within the object which can be eliminated through the heat treatment process [73]. This suggests that before parts are cut from the base plate, they undergo stress relief to relieve the internal stresses within the part [21]

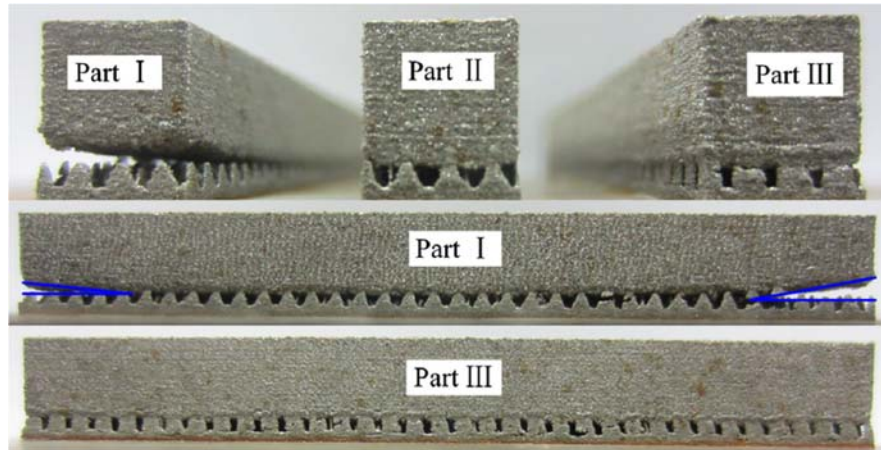


Figure 19: Parts breaking off the supports [16].

2.8.3. Dimensional accuracy and surface quality

The challenges associated with metal printing are dimensional control and surface quality for as-built parts [14]. Poor surface quality yields inaccurate dimensional accuracy. In addition, dimensional accuracy in self-supporting parts can also be affected by defects such as curling, dross formation, distortions and stair-stepping effect [74]. However, defects such as warping or distortions can be alleviated by the introduction of support structures for self-supporting geometries; (see Figure 19, Part II & Part III) [75]. On the other hand, geometries built at a relatively low angle require supports [76]. For this reason, support structures have to be incorporated when fabricating these structures in order to overcome geometric distortions and warping induced by non-uniform thermal stresses [77]. Warping occurs as a result of thermal stresses produced by rapid solidification of the melt pool and also might be due to the lack of support structures [17].

2.8.3.1. Support structures

Support structures are decomposed into two functional areas: support structure itself and the teeth connection between the support and the main part. AM uses support structures that can be found in two forms, either the same material or in dissimilar material. Support structures that are made from dissimilar material can be easily distinguished from the part; the process entails the utilisation of weaker material to

support which can be easily removed either applying chemicals as in Fused Deposition Modelling (FDM) [74] or mechanically. The types of support structures that are used in LPBF are made from the same material and are formed through the same fabrication process [74]. Figure 20 below shows different types and profiles of the support structures which have either a hollow or cellular profile.

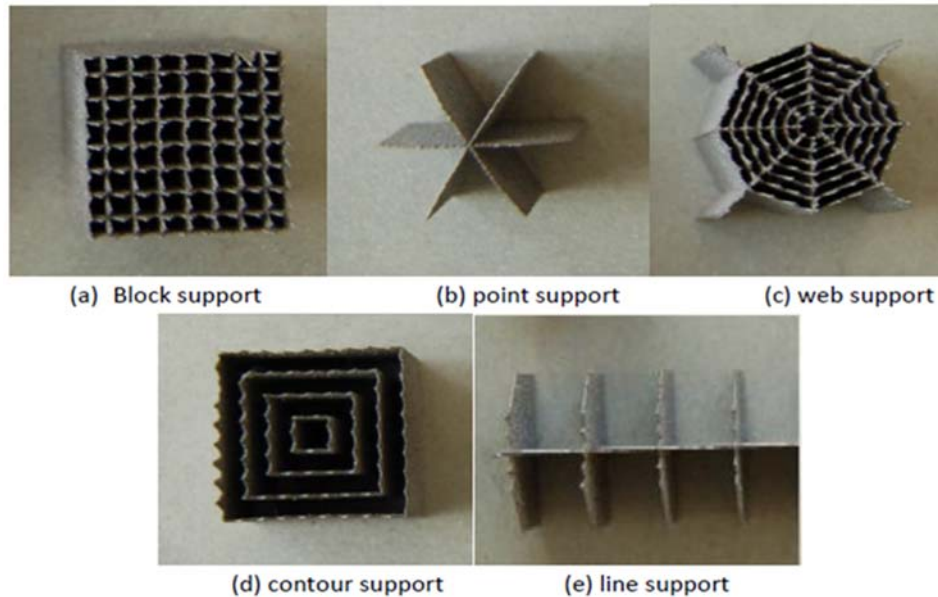


Figure 20: Different types of supports structures [75].

Support structures with teeth connections are easier to remove and good surface quality can be attained. However, teeth too close to each other require extra effort to detach from the part, whereas teeth too far apart might not be effective and can result in larger distortions of the part [15] – see the illustration of teeth dimensions in Figure 21 below. It has been reported that minimum contact area at the intersection between the part and the support should be used to avoid damage to the surface of the part but sufficient to provide mechanical constraints caused by production stresses. Large contact areas between supports and a part must be avoided as they are hard to detach and might result in damaging the surface of the part during support removal, which will leave the part with poor surface quality. To optimise the teeth connections, it is recommended to define the support structures teeth dimensions at the intersection between the support and the main part.

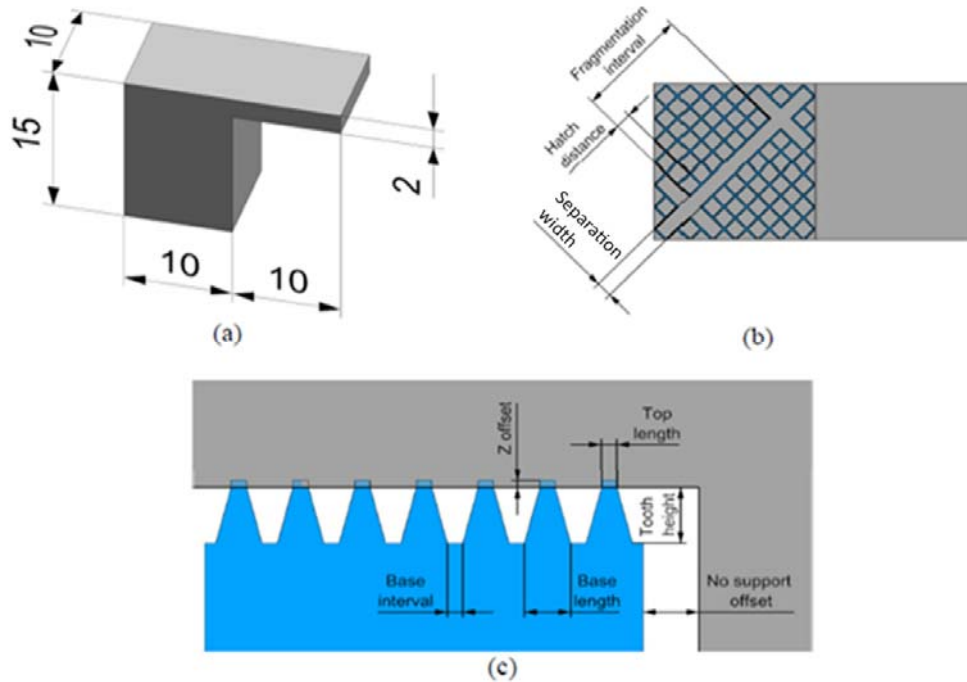


Figure 21: Contact area between part and support structure [74]

Previous studies reported that the top of the support structures may penetrate the part to ensure a strong joining between the support and the part [74]. However, the volume of the support structures needs to be as low as possible in order to be easily detached without damaging a part. Jarvinen *et al.* [71] carried out a study to compare two types of support structures in terms of attaining better support removal and achieving better surface quality, namely, tube and web supports. For the study, 17-4PH stainless steel bars were orientated at different angles 25° – 65° with a 5° increment between the angles. Dimensions for web supports were 1.3 mm and 1.45 mm, and for tube supports, diameters were 1.3 mm and 2 mm. It was determined that web support structures could be more easily removed than tube structures. Ultimately, web support structures produced better surface quality. A larger contact area in tube supports consequently makes them difficult to detach.

Calignano [15] used the Taguchi method to ascertain teeth parameter values that are appropriate for easy removal. The advantage of using the Taguchi method is the utilisation of an orthogonal array which helps to study the whole desired process with the minimum number of experiments. The experiments were conducted on an EOSINT M270 machine with laser power of up to 200 W. Two materials were

investigated: AlSi10Mg and Ti6Al4V powder. Block support structures were used as they are capable of supporting large parts and can be easily removed. Results of the investigation indicated that the appropriate values for aluminium alloy supports were at a hatch space of 0.5 mm, teeth height of 0.43 mm, and teeth base interval of 0.10 mm. There was little difference between the Z-offset values. For titanium alloy, the supports could be designed with a hatch spacing of 0.75 mm, teeth height of 0.43 mm, teeth base interval of 0.10 mm, and Z-offsets of 0.03 mm.

A similar study was carried out by Poyraz *et al.* [74] which focussed on the effect of support contact area in the form of teeth dimensions. Samples were manufactured on an EOS M290 machine using EOS Nickel Alloy IN625 material. The investigation focused on the influence of teeth top length in three different levels, namely, 0.15 mm, 0.25 mm, 0.35 mm, and also Z-offset at three different levels, viz., 0.04 mm, 0.12 mm, 0.2 mm on the block-type support structures. The results showed that both the teeth top length and Z-offset value reduction had an impact on the distortion results. Another observation made was that the extent of deformation was aggravated by a reduction in teeth top length or increase in Z-offset. This implies that an inversely proportional relationship exists between the two, and a balance must be achieved in order to reduce the extent of deformation of the built part. It was also observed that parts that failed or broke off from the support structures had irregularities to the surface as well as porosity formations, as shown in Figure 22 below.

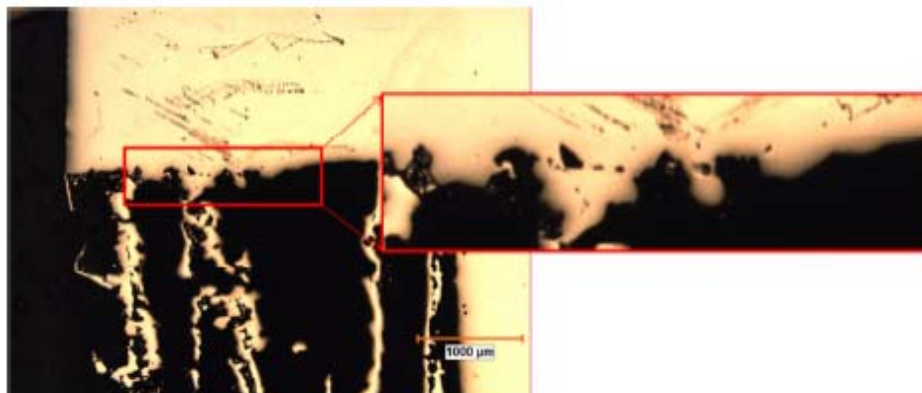


Figure 22: Self-detaching of the support structures [74].

Baskett [16] conducted a study on an LPBF machine to determine the effects of two contact area parameters, the teeth spacing, and top length, on the residual stresses in self-supporting features. The study focussed on 14 self-supporting parts made of 316L stainless steel which were subjected to a laser speed of 0.6 m/s and laser power of 200 W. From the experimental results, it was determined that increasing the top length reduces the amount of compressive stress in the Z-direction. Reducing the spacing between the contact areas will result in lower residual stress in the self-supporting feature. The study determined that a relationship exists between the contact area and a cooling rate. This is to say that increasing teeth contact area resulted in an increased average cooling rate in the unsupported part.

An investigation by Kajima *et al.* [78] studied the influence of intentionally added support structures on the microstructure and fatigue strength, using an EOSINT M280 LPBF machine. A clasp arm, fabricated at a 45° angle from Co-Cr-Mo alloy, was investigated; both supported and unsupported. Block-type support structures were chosen for the study. From the study it was seen that the supported specimen exhibited finer microstructures and had higher fatigue strength than the unsupported specimen. The finer microstructure can be attributed to the introduction of support structures which facilitated higher cooling rates. When tested for fatigue strength, the supported specimen managed to hold up to 217% more cycles than the unsupported specimen. The unsupported specimen exhibited more defects such as pores and micro-cracks. The study concluded that adding support structures in a part can yield good results with regard to fatigue strength.

However, Jhabvala *et al.* [79] proposed to use a pulsed laser system to fabricate supports in LPBF systems. The study was conducted on a R&D LPBF system which uses Nd: YAG laser system with an average operating power of 100 W. Block-type support structures made of 316-stainless steel and silver were used for the study. It was determined that a pulsed laser system facilitates the fabrication of porous structures with inferior mechanical properties compared with those made by continuous laser. According to the study, support structures fabricated by pulsed laser system can be easily detached and are capable of withstanding forces from the powder scraper and large thermal distortions. On the other hand, Hussein *et al.* [21] recommended building self-supporting parts with negative warping; ultimately

attaining a flat surface after warping. However, Tounsi *et al.* [72] proposed a different approach of contact-free supports structures that entails building a thick block underneath an unsupported part that is able to overcome the distortion and achieve good surface quality. According to the study, the major defects associated with LPBF, such as loss of thickness and decrease in layer length due to higher heating and cooling rates, can be minimised by employing a heat sink beneath the unsupported surfaces. This approach was supported by Cooper *et al.* [77] who determined that the gap distance between the support and the heat sink should be at least 0.63 mm in order to provide sufficient thermal properties. It was recommended that the introduction of heat supports minimise the inevitability of post-processing whilst also reducing part distortion (Figure 23).

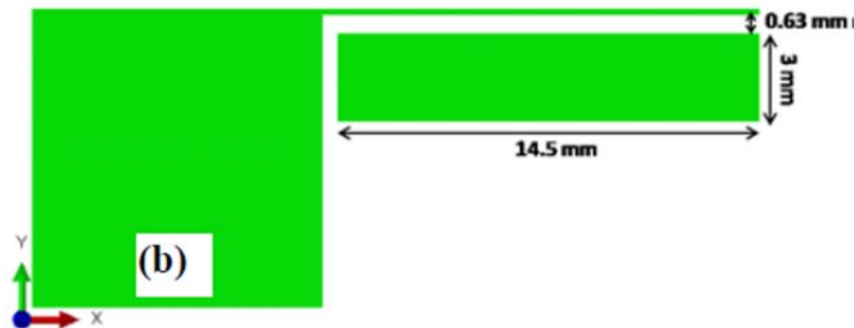


Figure 23: Cantilever beam with heat support [77]

2.8.3.2. Building strategy

Previous studies have reported that designers need to adjust part orientation during the design stage to alter the angle of inclination [19]. By adjusting the part orientation, the self-supporting angle changes, thus influencing the amount of support to be generated [80], [81]. Strano *et al.* [5] demonstrated this on a truss with complex shape geometries where a significant material saving of up to 45% can be achieved by an optimal part orientation, shown in Figure 24. Similar results were presented in [76] where a big difference in support volume was observed when tilting a part by 18° from the substrate about the X-axis; however, there was a minimum influence on the build time. In addition, it has been reported that adjusting part orientation on the part to reduce the volume of support structures may contribute to an increase in height, subsequently resulting in an increase in time taken to fabricate the part [76].

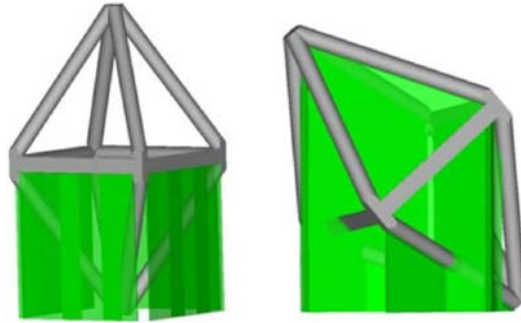


Figure 24: Illustration of best (left) and worst (right) orientations [5]

On the other hand, literature has shown that build time depends on part size, scanning speeds, build orientation and layer thickness. For example, it takes a longer period to print an object that is longer in the layer-up direction or Z-axis or Z-height [22]. Build time for parts manufactured by LPBF is directly affected by Z-height [82]. This suggests that if the part is bigger in the Z-direction, more layers are required to print the object and a greater volume of powder is needed to fill up the machine, but it does not affect the number of parts to be produced. The number of parts to be printed is directly affected by the X- or Y-printing direction and indirectly influences the amount of powder needed and build time. It has been recommended that in order to minimise the amount of powder needed to fill up the machine and reduce printing time the Z-height direction should be minimised which subsequently results in a decrease in the number of layers required to build a part [82].

2.8.3.3. Stair-stepping effect

Stair-stepping effect in LPBF produced parts can be attributed to the layer-by-layer nature of the manufacturing technique. In addition, the stair-stepping effect occurs as a result of the build angle and powder layer thickness [52]. This drawback becomes more pronounced if the layer thickness is increased and an inclination angle is low towards the base plate. The stair effect can be minimised by reducing the layer thickness and increasing the build angle. On the other hand, the stair effect occurs as a result of uniform slicing particularly to angled surfaces and round geometries. By reducing the slicing thickness, the stair-stepping effect becomes smoother. Fox *et al.* [86] defines slicing as a process that entails the slicing of the CAD file into thin layers to create 2-dimensional data which the AM machine can utilise as the build guideline – see Figure 25 below.

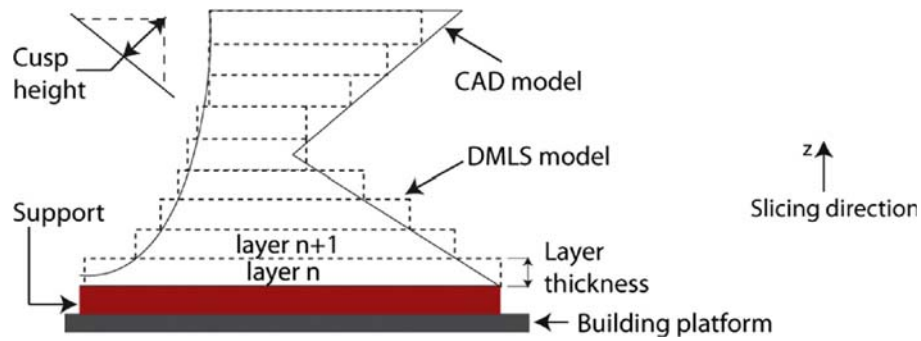


Figure 25: Stair-stepping effect illustration [15]

It was found that it is difficult to attain optimal adhesion between the single layers, by increasing the layer thickness, due to insufficient melt depth [58]. Thicker layers require more material to be melted by the laser energy, which can lead to evaporation and the intensive fluid flows. Furthermore, it was determined that the powder layer thickness influences the surface roughness of the samples as shown in Figure 26. Surface roughness of the thinner layers tends to be better than that of the thicker layers in the given processing conditions [58].

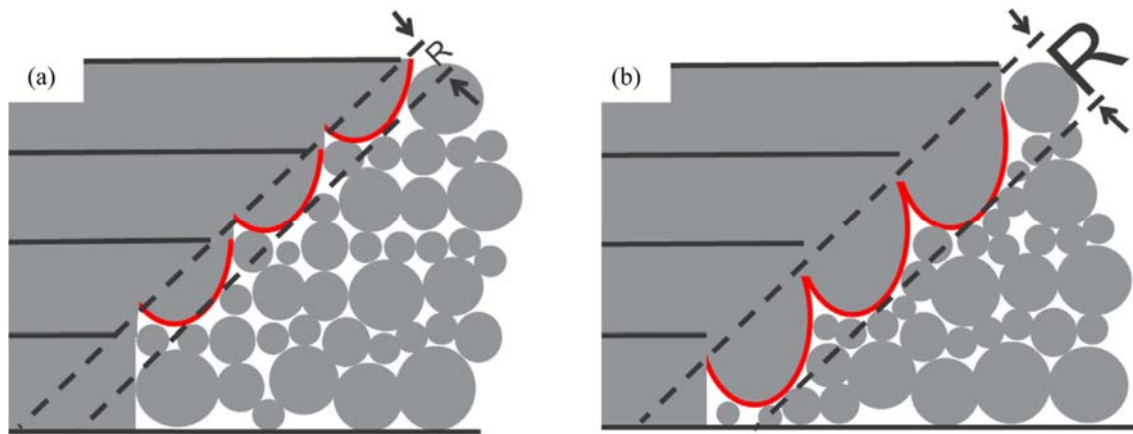


Figure 26: Illustration of the resultant surface roughness (R) for different melt depths for different laser powers [36].

2.8.3.4. Contouring

Contouring involves scanning the perimeter of the selected areas during the LPBF production process [40]. Contour scanning enhances accuracy and the surface quality of the objects by re-melting irregularities on surface edges. This is achieved by minimising inhomogeneity to the surface. However, the area of re-melting is subjected to the laser spot size and contour beam offset as well as the energy input

of the contour scan. The diameter of the melted zone is usually larger than the laser diameter which is necessary to compensate for the dimensional error and the laser beam to make sure that the contour of the finished part will correspond exactly to the original CAD data. This correcting position is known as beam offset.

2.8.3.5. Hatch spacing

Hatch spacing has been identified to contribute to the level of surface roughness [87]. Smaller hatch spacing results in a smoother surface until it reaches an optimum level and a further reduction results in poor surface roughness [57]. However, large hatch spacing promotes the attachment of partially melted powder particles to the surface. This can be attributed to an increased melt pool size which deteriorates surface quality [52].

2.8.3.6. “Upskin” and “downskin” surfaces

Parts that are supported by metal powder instead of solid support structures are dubbed as self-supporting [75]. This means that self-supporting parts relate to an inclined or sloping object that is melted on top of loose powder particles instead of support structures during the fabrication process. Moreover, self-supporting parts are used to regulate the amount of building support structures on angled walls and surfaces [15]. In these parts, first layers that are melted directly on the powder, will shrink and warp which subsequently leads to unwanted results such as cracks and high roughness [21].

Surfaces for the self-supporting objects can be classified into two categories, i.e. “upskin” and “downskin” surfaces. Downskin is defined as a surface that is facing downwards towards the base plate whereas upskin is a surface that is facing upwards. Downward-facing surfaces normally possess higher surface roughness than upward-facing surfaces [19]. Poor surface quality is the main challenge associated with parts produced by LPBF, especially for self-supporting objects. This can be attributed to drawbacks such as stair-stepping effect and powder particles sticking to the surface [52].

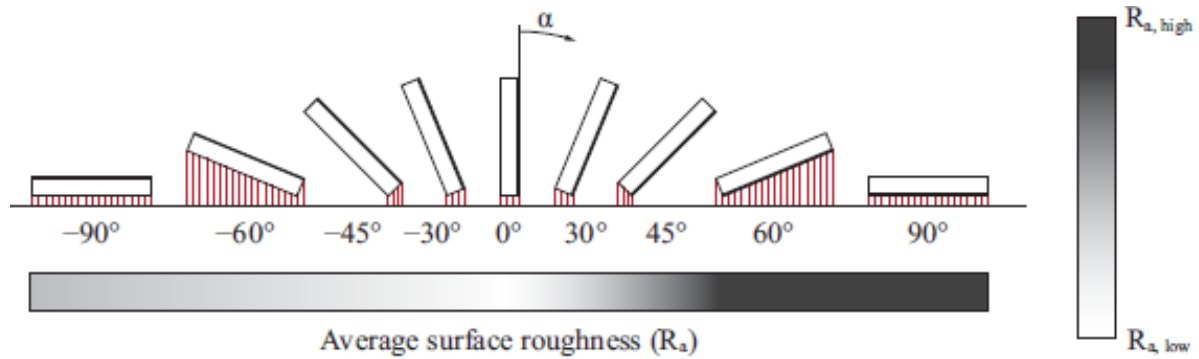


Figure 27: Illustration of sloping angles that can build parts with or without supports structures [83].

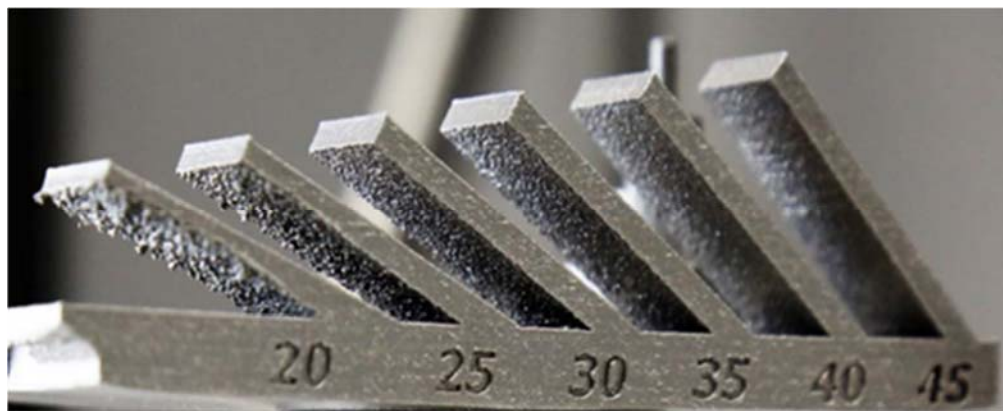


Figure 28: Illustration of unsupported self-supporting parts [84].

A study by Chen *et al.* [85] evaluated the measurement of surface roughness for parts produced by EOS M280 LPBF machine on Ti6Al4V. Optimised parameters of 350 W laser power, 770 mm/s scan speed and 0.18 mm hatch distance were utilised for the study. Samples at inclinations of 40°, 50°, and 60° were grouped at different positions along a base plate for ease of comparison. The cross-section for the upward-facing surface observed through an electron microscope had lower peak amplitude and smoother transitions. Downward-facing surfaces with higher arithmetic average height (R_a) values and root mean square (R_q) exhibited deeper melt pool penetrations. Results indicated that the orientation of a part affects surface roughness, and the roughness values for the upward-facing surfaces were found to be lower compared to downward-facing surfaces, as previously outlined by Covarrubias *et al.* [14].

2.8.3.7. Inclination angles

Covarrubias *et al.* [14] conducted a study on an EOS M290 system to evaluate different surface roughness values at different inclinations. For the experiment, a test artefact called parallelepipeds, fabricated from EOS Nickel Alloy IN718, was used to characterise the surface morphology. Analytical calculations for surface roughness were conducted and validated by characterising the fabricated test artefacts produced with different angles. A scanning electron microscope (SEM) was used to study the influence of other effects on surface morphology. From the experiments it was determined that the surface roughness value at 60° and 75° were lower than the angle 90°. Higher surface roughness at 90° was a result of incomplete melting between the layers. Theoretically, at an angle of 90° roughness value should be 0°. Also, theoretical calculations assume a perfect environment with sharp edges whereas AM has round edges.

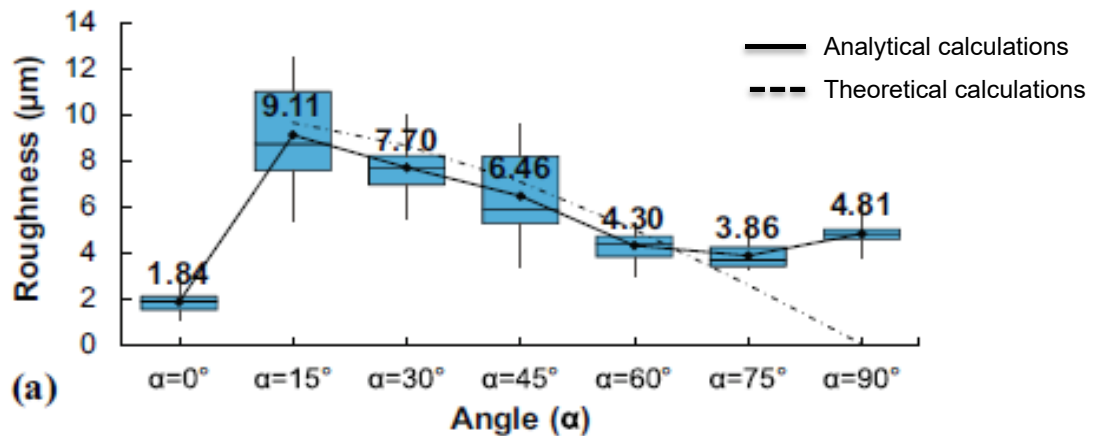


Figure 29: Graphical illustration of roughness versus angle [14].

A similar study was performed by Barari *et al.* [88] on cusp geometry on the Fused Deposition Modelling (FDM) process using Acrylonitrile Butadiene Styrene (ABS) material. The study conducted both analytical and experimental investigations of the effect of surface roughness at different angles and using different layer thicknesses. The specimens were fabricated at layer thicknesses of 150 µm, 250 µm and 500 µm. Angles that were evaluated varied from 5° to 85° in increments of 5°. From the study it was determined that for all angles below 70°, the value for the actual evaluated angle is smaller than the commonly assumed theoretical roughness value. The

reason for the difference in roughness values is that the theoretical calculation overestimated the real surface roughness, which according to the author can be as high as 30%. For angles close to 90° , the actual evaluated surface roughness was larger than the commonly used theoretical estimated value. The large Ra values were identified as being the result of the corners that are neglected by analytical calculations produced by the AM process, [14][88].

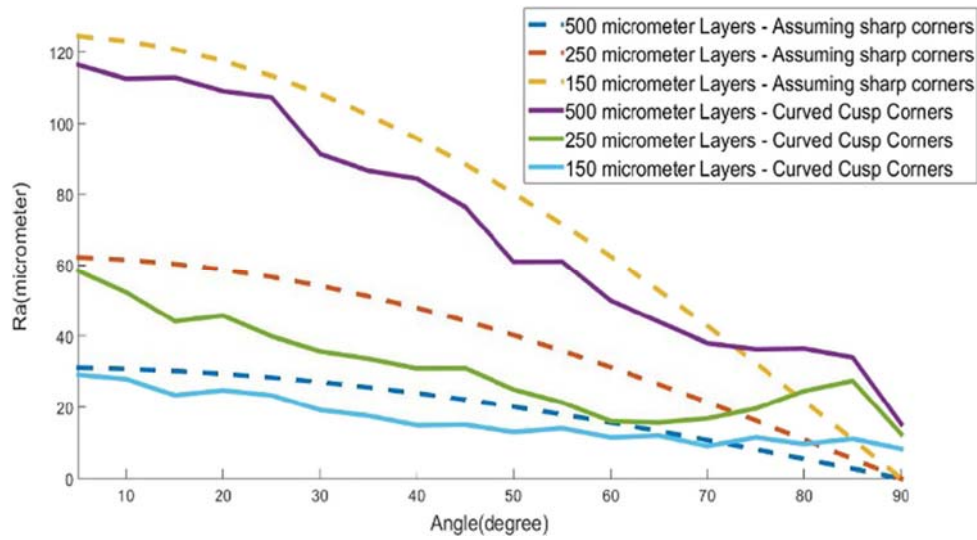


Figure 30: Solid lines indicating calculated Ra values and dashed line for trigonometric model [88].

On the other hand, Wang *et al.* [7] studied the influence of process parameters, such as laser power and scanning speeds, on fabricating self-supporting objects with different angles. For the experiment, an LPBF machine was used to fabricate a specimen made of gas-atomized 316L stainless steel powder. It was initially determined by means of analytical calculations that a minimum angle of 27° was achievable on an LPBF machine. Experimental work was carried out at process parameters ranging from 120 to 180 W laser powers, and 200 to 1200 mm/s scanning speeds as a means to validate the calculated angle. Inclination angles were varied from 45° to 25° . From the experimental results for scanning speed, it was found that at low speed of 200 mm/s for the inclination angles tested, deformation defects were identified at all angles, but an increase in scanning speed to 600 mm/s only reported defects at a 25° inclination angle and parts experienced

major warping when the speed was increased to 1200 mm/s. When laser power was increased to 180 W, parts experienced more warping compared to parts fabricated at 150 W. From the study it was concluded that parameters such as scanning speeds and laser power limit the options for the angle of inclination.

Calignana [89] found that the orientation and position of the component with respect to the blade and other parts can affect surface roughness. For thin layers, the increase in surface roughness was mainly due to the presence of partially fused particles that adhere to the molten part, but not stair-stepping effect. The number of attached particles due to heat varied depending on the building angle, as shown in Figure 31. Process parameters, orientation and position of the part with respect to the recoating blade and the powder material – all will influence dimensional accuracy and surface roughness of LPBF parts.

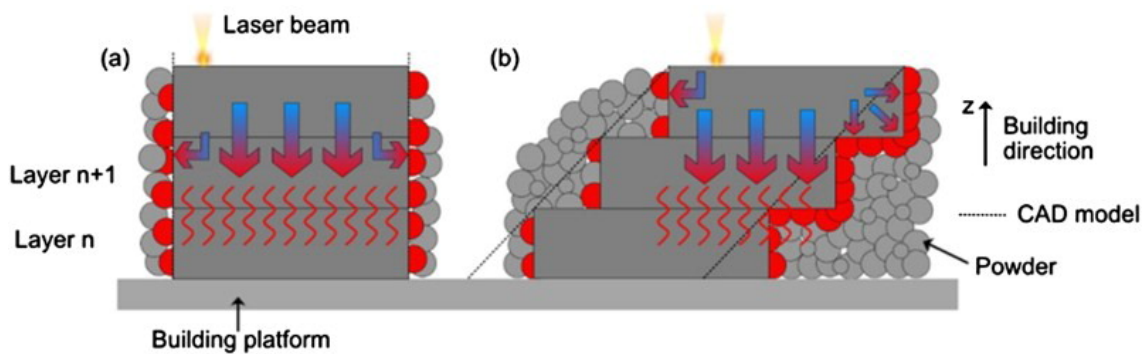


Figure 31: Illustration of heat flow for two different building angles. The number of attached particles (red spheres) due to heat varies depending on the building angle: (a) 90° building angle; (b) 45° building angle [89].

2.9. Post-processing LPBF parts

Post-processing includes the removal of loose powder, heat treatment process, cutting off parts from the substrate, support removal and surface modification [90], [91]. Previous studies have shown that the more complex the part, the harder it gets to do post-processing [14]. In addition, the manual removal of support structures after the production process increases the cost of post-processing [80]. Hussein *et al.* [21] also reported that support structure removal of delicate parts is a challenging

task; it adds to post-processing time and may result in small parts breaking, leading to inaccurate dimension accuracy.

Summary

This chapter highlighted the fundamentals of AM and the importance of having optimised processing parameters during the LPBF manufacturing process was investigated. The effects of building with or without support structure on the final product was also discussed.

The chapter also revealed the importance of understanding the melt pool dynamics to ascertain the build rate success of parts in LPBF. Non-optimal processing parameters, such as scanning speed and higher laser power, were found to be associated with the formation of parts with defects. Researchers in the field of AM need to be conversant with the individual LPBF machine's limitations by carrying out process development. Although building without using support structures saves on time and material, drawbacks such as poor surface roughness, porosity and warping can still influence the final product; that is to say, these defects need to be studied and realised in order to improve on process development.

This section also detailed the advantages and disadvantages of building using support structures and their effect on the surface during post-processing. Previous studies recommended first orientating a part into an angle that does not require support structures. Then, if the orientation of the part cannot self-support, support structures should be used. However, it was suggested that the contact between support and the part should be optimised for unsupported geometries. The area where supports contact the part determines the integrity of support structures and also determines the success of the part. Similarly, this study also highlighted other methods available, such as heat support structures.

CHAPTER 3: MATERIALS AND METHODS

This chapter presents the type materials used and also outlines the test plan to produce the samples. The test plan was formulated based on the literature studies which were performed on commercial systems.

3.1. Material

Titanium alloys are named according to their grade number as well as their impurity. Therefore, the purity of titanium is determined by the increase in grade number. This indicates that grade 1 is the purest titanium grade out the entire grade [92]. Grade 5 (Ti6Al4V) alloy is the most explored alloy with very good mechanical properties, such as good corrosion, ductility and low density, which makes it an ideal material for aerospace applications. [93]; [94]. Often the reason for choosing Ti alloy is weight savings [95].

All samples for this study were fabricated using gas atomised pre-alloyed Ti6Al4V powder supplied by TLS Technik GmbH & Co. Spezialpulver KG with the chemical composition shown in Table 3.

Table 3: Ti6Al4V chemical composition (wt.%)

Al	V	C	Fe	O	N	H	Y	Ti
6.38	3.96	0.006	0.161	0.006	0.008	0.002	<0.01	bal.

The Ti6Al4V was comprised of spherical powder particles which had equivalent diameters $d_{10} = 22\text{--}27\text{ }\mu\text{m}$, $d_{50} = 35\text{--}40\text{ }\mu\text{m}$ and $d_{90} = 51\text{--}56\text{ }\mu\text{m}$, as shown in Figure 32. The powder particles were characterised using scanning electron microscope.

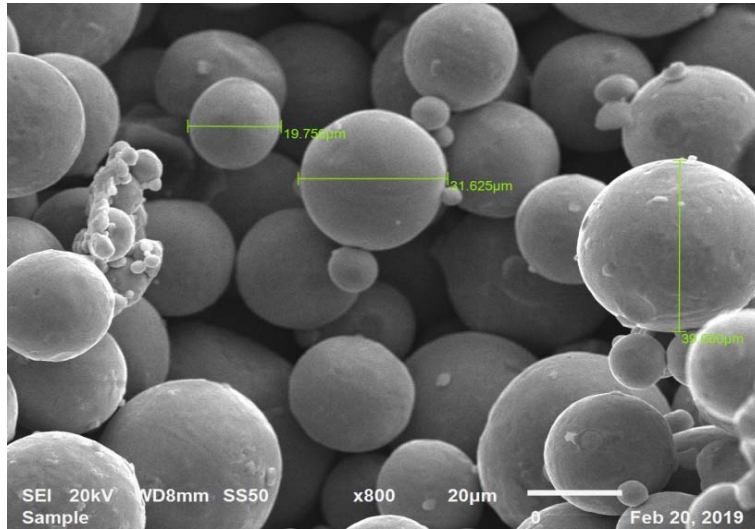


Figure 32: Morphology of Ti6Al4V powder particles.

3.2. Methods

3.2.1. CAD software

Test samples were designed and prepared using commercial software SolidWorks® 2019 and Materialise Magics. SolidWorks was used to design the 3D CAD files. Materialise Magics was used for slicing the part and to generate supports before transferred to the machine for printing.

3.2.2. Aeroswift machine

The samples were printed on the Aeroswift platform shown in Figure 33. The Aeroswift platform uses the ytterbium laser with a wavelength of 1076 nm and a maximum power output of 5 kW. This machine has a build volume of 2000mm × 600 mm × 600 mm. Before the start of the build, the machine was filled with argon until the value reached below 100 ppm. Argon was used as the shielding gas to avoid oxidation. Before filling the machine, the powder first had to be dried by heating it in an oven at 120° C for four hours to remove moisture.

During the building process, the powder layer thickness was maintained at 50 μm which is the distance equated to the movement of the z-axis. Bi-directional or back-and-forth (zigzag) scanning strategy was used to scan the powder layer. First, the

sample body was scanned, then contouring with the same process-parameters for all samples was implemented afterwards.

A manufactured test artefact called parallelepipeds is shown in Figure 34. Test artefacts are used to quantify surface roughness for LPBF specimens at different angles during process optimisation [29]. Test artefacts were manufactured on solid blocks that were scanned in a similar way with parallelepipeds.

Figure 34 also shows the build layout of the samples at different orientations. This will help to understand the effect of surface roughness for parts fabricated at different orientations: set A, D (YZ orientation), set B, C (XZ orientation) and set E, F were repetition of set B, C. The blue arrow in Figure 34 indicates that scanning started from left bottom corner.



Figure 33: The external structure of the Aeroswift machine.

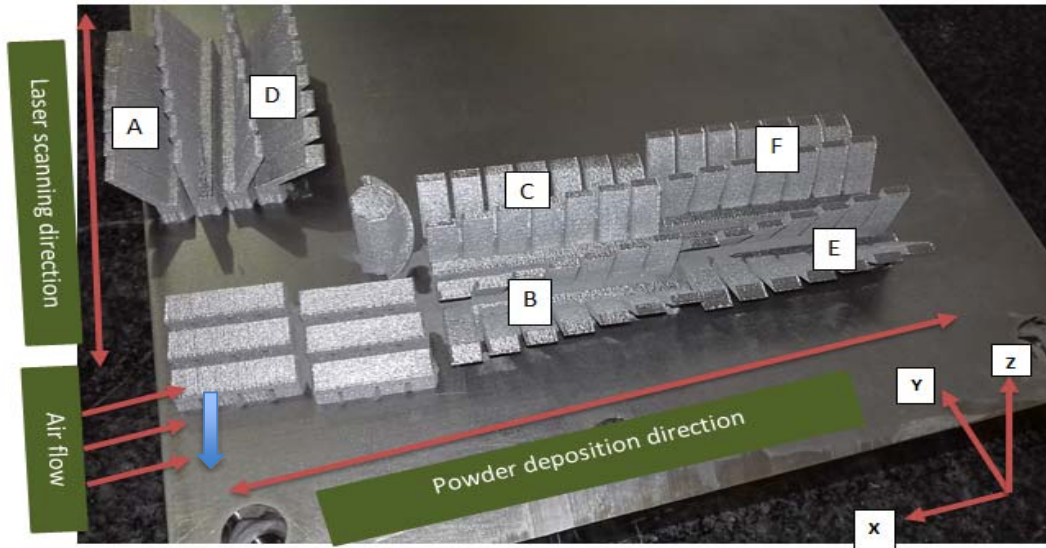


Figure 34: Build layout for samples build.

3.2.3. Mitutoyo Surftest SJ-210

After completing the building process, samples were submerged in an ultrasonic bath for 10 minutes with acetone to remove the impurities before performing surface characterisation. The surface roughness for the samples was measured according to ISO 427:1997 [96]. Mitutoyo Surftest SJ-210 instrument (Figure 35) is a surface roughness measuring device that was used to characterise different surface variations on the samples.

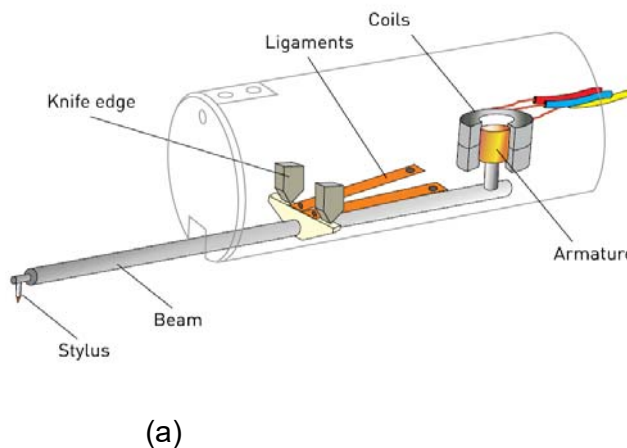


Figure 35: Schematic of surface roughness measuring instrument (a) and Mitutoyo SJ-210 Surftest roughness measurement instrument (b).

The stylus is the measuring tip of the instrument. This instrument works by gathering information through an amplified electrical signal to produce both numerical results and a graph of the surface profile. The calculations of Ra , Rz and Rq parameters by the Mitutoyo Surftest SJ-210 are based on the following equations:

$$Ra = \frac{1}{l} \int_0^l |y(x)| dx \quad (\text{Equation 1})$$

$$Rz = \frac{1}{n} (\sum_{i=1}^n p_i - \sum_{i=1}^n v_i) \quad (\text{Equation 2})$$

$$Rq = \sqrt{\frac{1}{n} \sum_{i=1}^n y_i^2} \quad (\text{Equation 3})$$

Where l is sampling length, p_i is the vertical distance from the highest peak and v_i the lowest valley within five sampling lengths. The main advantage of using a Mitutoyo Surftest SJ-210 instrument as a measuring tool is the ease of collecting data. This measuring instrument was only limited to physically gathering the surface texture values for Ra ; Rz and Rq for the upskin and downskin surfaces. The cut-off length that was used is 2.5 mm based on the standard [96]. During the characterisation the Mitutoyo Surftest SJ-210 stylus was made to traverse perpendicular to the lay direction to account for the stair-stepping effect.

3.2.4.3D Zeiss Smartzoom 5

The 3D Zeiss Smartzoom 5 optical microscope (Figure 36) was used to gather qualitative results by acquiring images of the surface roughness on the samples. The images were compared with the Mitutoyo Surftest SJ-210 measured results.

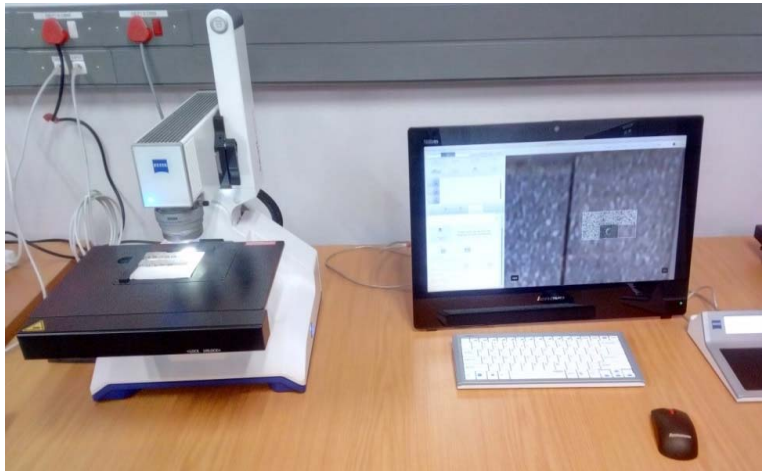


Figure 36: 3D Zeiss Smartzoom 5 microscope.

3.2.5. Scanning Electron Microscope

Scanning Electron NeoScope 5000 was used to qualitatively characterise the surface roughness of the samples. The samples were first submerged into an ultrasonic-bath for five minutes to remove impurities on the surface of the samples. The downskin-, upskin- and top surfaces were characterised on the SEM at 15 kV accelerating voltage and 15 mm working distance.

3.2.6. MicroCT

X-ray microcomputed tomography (microCT) is a non-destructive measuring technique used for testing and characterising AM fabricated specimens for accurate analysis of dimensions and porosity [98]. This tool can also be used to study the cell morphology and to evaluate internal and external surface roughness, overall structural integrity and the extent and distribution of internal defects [100]. For this study microCT was only limited to measure surface roughness height parameters also known as 3D parameters such as Sa, Sz, Sp, Sq and Ssk. X-ray microCT works on the principle of irradiating a sample with a beam of X-rays, measuring the subsequent absorption X-ray image, and repeatedly acquiring such images as the sample rotates [98], Figure 37. Surface roughness parameters were estimated by the method described in [99].

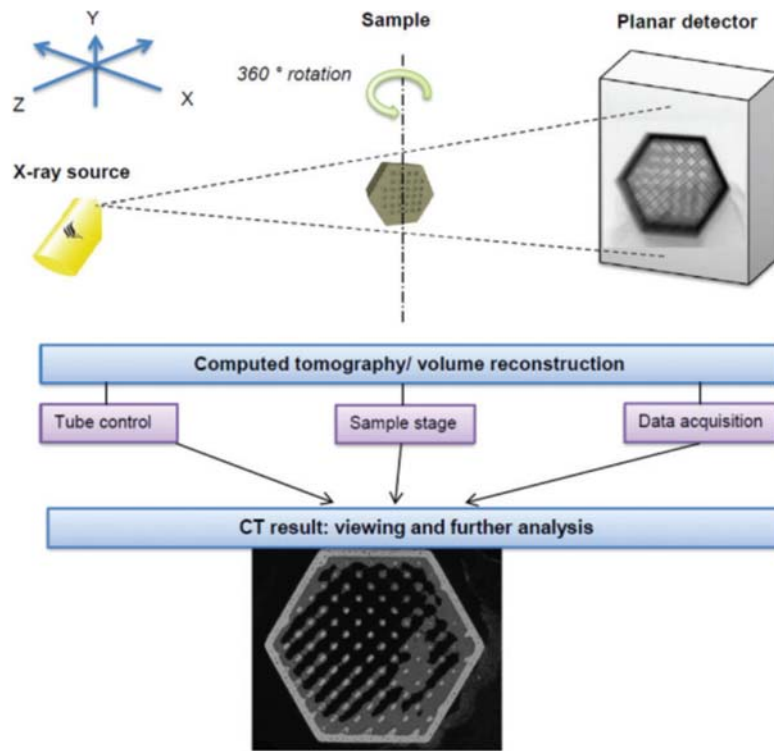


Figure 37: Schematic representations of MicroCT scan [98].

3.2.7. Statistical analysis

Average values and standard deviations of roughness values measured by Mitutoyo Surftest SJ-210 were calculated in Excel. Two-sample Student's t-test for independent samples (unpaired samples) was used to determine if there was a significant difference between the means of two sets (statistical significance was less than 0.05).

Summary

This chapter outlined the approach that was undertaken to execute the research objectives of this study. The method of fabricating a test artefact to characterise surface roughness is a common technique which has been used by other scholars. However, the previous chapter (chapter 2) failed to cover the amount of surface roughness values obtained when building using high laser power and high scanning speed at different orientations. The successful execution of this methodology will generate new information for building parts using high laser power and higher scanning speed on the Aeroswift platform.

Chapter 4: Results and discussion

This chapter presents and discusses the results obtained as per the research objectives. The surface roughness results were analysed for the test artefact for both upskin and downskin surfaces. In addition, a relationship between porosity and surface roughness for different inclination angles was investigated on the test artefact.

4.1. Characterisation of surface roughness on different inclination angles

The first characterisation was a quantitative analysis conducted using a Mitutoyo Surftest SJ-210. Each measured sample comprised of 14 downskin and 14 upskin surfaces. Each surface roughness was measured parallel to the long side six times in different areas of the surface and the results were averaged. The averaged roughness results were then plotted as a function of an angle. Subsequently, a qualitative study was conducted to validate the surface roughness measured results. This was achieved by using microCT and 3D Zeiss Smartzoom 5 digital microscope. Typical profiles of surface roughness are shown in Appendices 5–8.

4.1.1. 2D surface roughness characterisation

4.1.1.1. Measured Ra values for downskin and upskin surfaces

Figure 38 shows Ra values for sets A, B, C & D for downskin surface against the inclination angle. Ra is defined as the arithmetic mean height which defines the average roughness of a profile. The roughness parameter (Ra) is important in identifying variations of a surface [97]. Figure 38 shows a downward linear trend for surface roughness which improves as the sloping angle increases. The initial Ra value between 25° to 45° for all orientations attained the highest average compared between 50° and 90°. Ra average values with standard deviation are shown in Appendix 1 for sets A–B. A difference in Ra value was found between sets A, D (YZ-orientation), and sets B, C (XZ-orientation) that can be attributed to powder sticking to the surface and the stair-effect which was reported as becoming more pronounced at smaller angles and thus deteriorates surface quality, i.e. 25° to 45°. This is in

agreement with the findings in [14] that parts manufactured by the LPBF process with angles less than 45° are greatly influenced by stair-stepping effect. The effect of stair-effect on the sloping angle is illustrated in Figure 39.

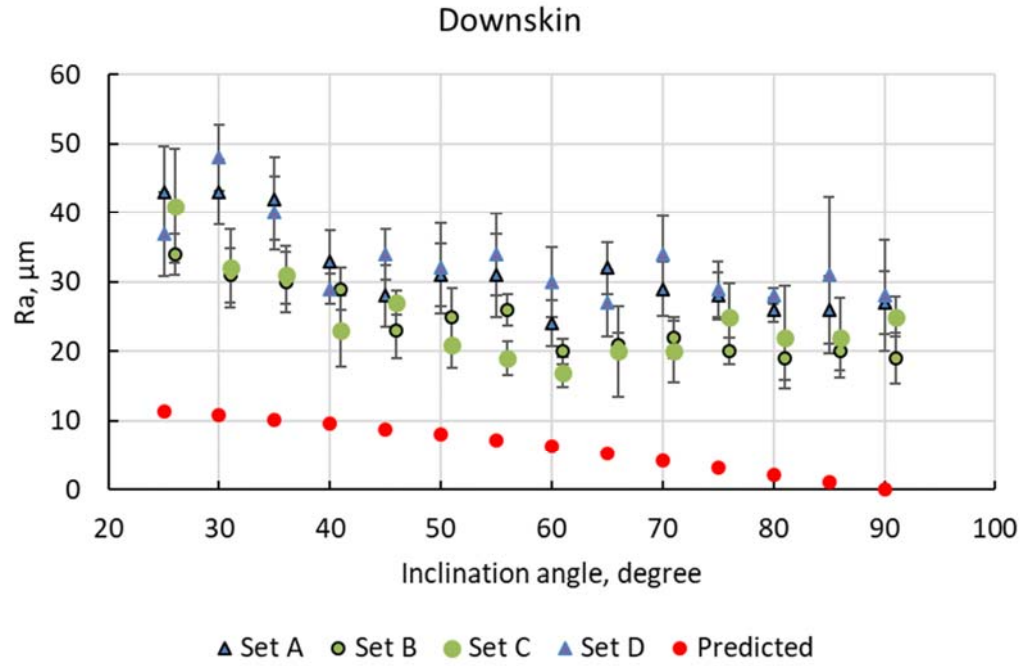


Figure 38: Ra values for downskin surface at different inclination angles.

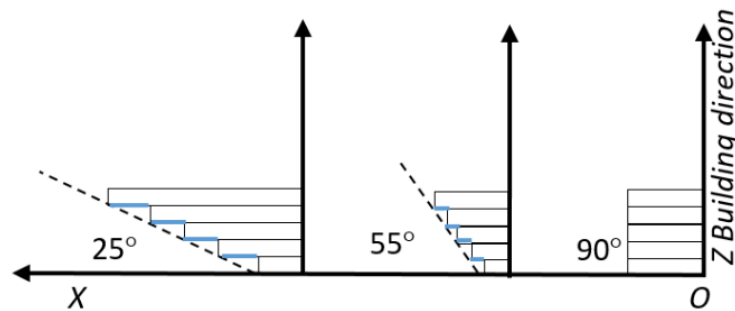


Figure 39: The illustration of stair-stepping effect for different sloping angles.

On the other hand, Figure 38 shows the predicted roughness value at 90° is 0 μm. The predicted roughness values were based on equation 4:

$$Ra_{predicted} = \frac{L_t}{4\cos(\alpha)} \quad (\text{Equation 4})$$

Where, Lt is the layer thickness, and α is the inclined angle. It was previously reported in [5] and [14] that Equation 4 neglects the round corners of the LPBF process; it assumes an ideal environment with perfectly sharp edges which make it not ideal for quantifying the degree of surface roughness.

There is no distinct difference in the trend on the level of surface roughness for the increasing sloping angles for the upskin surface in Figure 40. The formation of this kind of a trend can be mainly attributed to the stair-stepping effect for angles lower than 45° because the upskin surface does not directly solidify on top of loose powder particles unlike the downskin surface, shown Figure 41. However, for angles greater than 45° , R_a is increased due to trapped powder particles that adhere to the surface during laser processing which contributes to the increased surface roughness values.

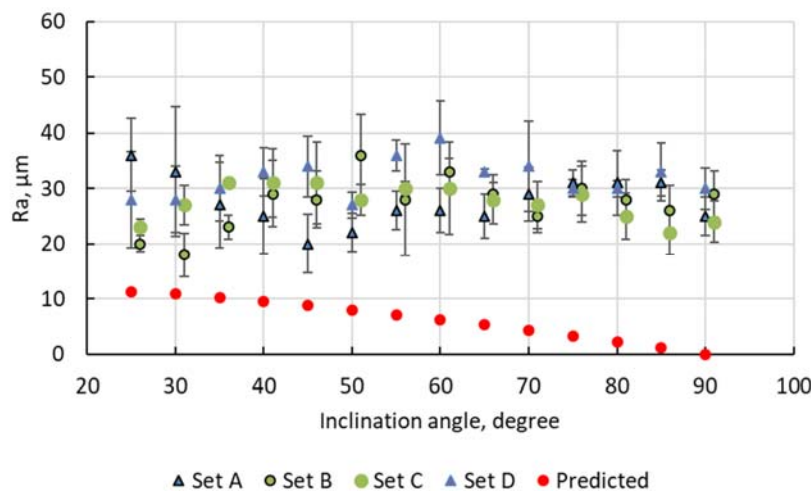
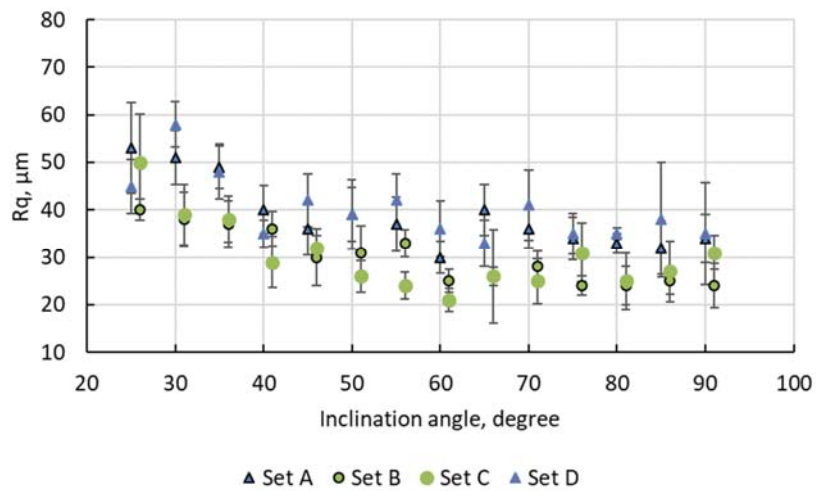


Figure 40: R_a values for the upskin surfaces.

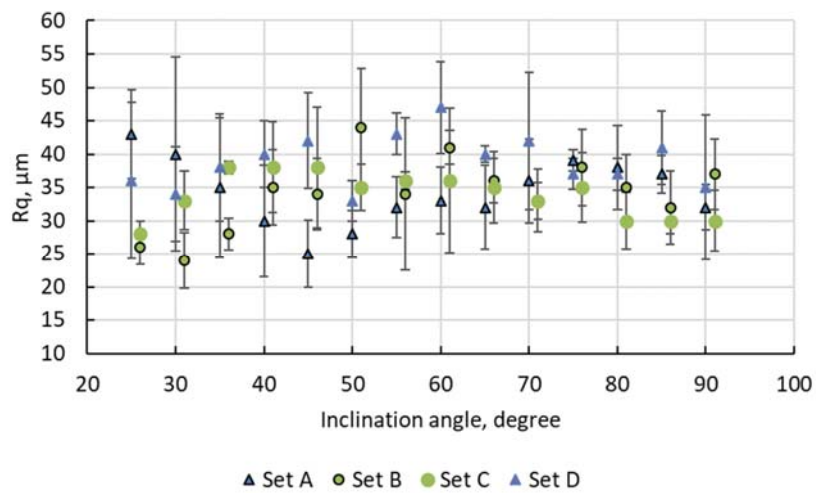
On the other hand, Ayad *et al.* [102] argues that using the R_a parameter alone is not sufficient to characterise surface roughness. Although R_a is the commonly used parameter, it only gives the overall description of the profile, but no information about the waviness and is not sensitive to small changes in the profile. Therefore, R_q and R_z are recommended in addition to characterising surface roughness [103].

4.1.1.2. Root mean square Rq

Root mean square (Rq) parameter evaluates the individual peak of a surface. Sedlacek *et al.* [103] added that Ra is not sensitive to profile deviations; therefore, making Rq the preferred parameter. However, the Rq value can also be approximated using the formula: $Rq \approx 1.25 Ra$. The average Rq values attained for samples are shown in Appendix 2. The relationship for both Rq and Ra parameters for the upskin and downskin surfaces can be confirmed in Figure 38, Figure 40–Figure 42 (a, b) correspondingly.



(a)



(b)

Figure 41: Rq values for both (a) downskin and (b) upskin surfaces.

4.1.1.3. Rz values for downskin and upskin surfaces

Figure 42 and Figure 43 illustrate the measured ten-point height amplitude parameter as a function of an angle for both upskin and downskin surfaces. Rz is also known as the roughness height. It measures the average between five highest peaks and five deepest valleys of the surface [97].

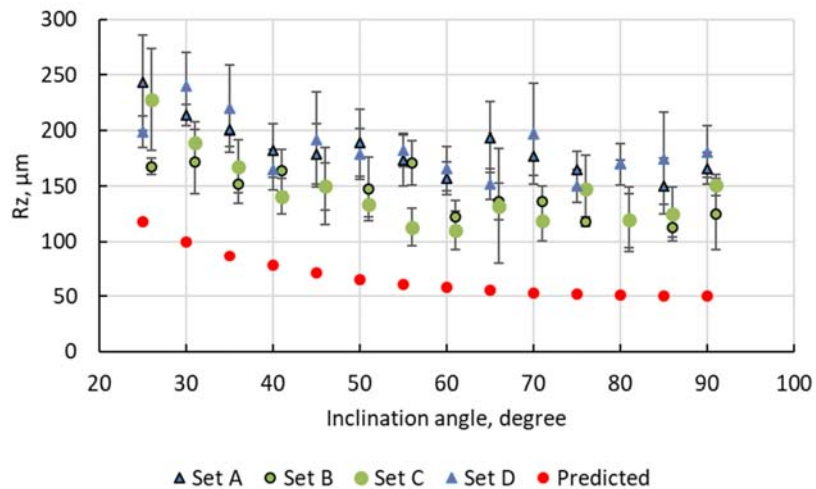


Figure 42: Ten-point height (Rz) representation for downskin surfaces.

As expected, although Ra and Rz are not comparable parameters, it can be observed that the surface with the highest Ra value had the largest height profile deviations (Rz). Ten-point height only covers surface irregularities such as the individual peaks and valleys on the samples. The average Rz values attained for the samples are shown in Appendix 3. On the whole, samples manufactured in the YZ direction (sets A and D) had higher roughness than XZ samples (sets B and C), see (Figure 42).

The height deviations for surface can also be analytically predicted using the following equation:

$$h = \frac{L_t}{\sin(\alpha)} \quad (\text{Equation 5})$$

Where h is the distance between consecutive step edges, L_t is the layer thickness, and α is the inclined angle. Rz values in Figure 42 and Figure 43 were calculated taking into account about 50% shrinkage of powder material and 50 μm distance

equated to the movement of the z-axis. However, the predicted values (see Appendix 4) do not take into account the amount of partially sintered particles that adhere to the surface which might have contributed to the difference in surface roughness.

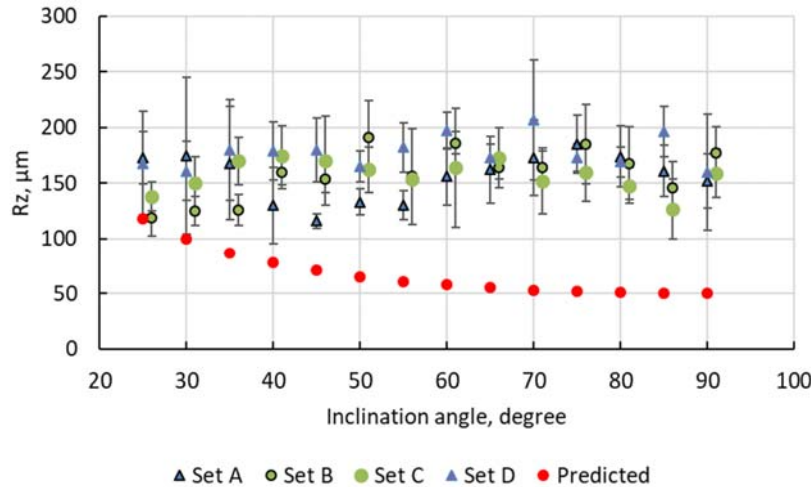


Figure 43: Measured ten-point height values for the upskin surface.

On the other hand, the trend in Figure 43 for the upskin surface does not show a clear decrease or increase in the roughness values as the sloping angle increases from 25° to 90°. This type of curve is comparable to the Ra and RMS values observed for the upskin surfaces in Figure 40 and Figure 43.

Strano *et al.* [5] and Krol and Tanski [52] explained that at low angles the particle size is smaller than the step edges. As the angle increases, the edges become smaller thus leading to a higher concentration of partially sintered particles resulting in increased poor surface quality.

4.1.2.3D surface roughness characterisation

4.1.2.1. Quantitative analysis for surface roughness by CT scans

The amplitude 2D parameters covered in the previous section give an idea of the surface deviation. However, this section will cover an in-depth evaluation using areal height parameters such as Sa, Sz, Sq, Sp and Ssk. Therefore, the analysis focussed on two orientations samples (A and B) which were orientated in the YZ-direction (set A) and XZ-direction (set B). The measured results were conducted on the downward

surface which in the previous section was found to have the worst surface roughness. In addition, these results were measured using microCT on an area of 6 mm × 12 mm. Sa can be represented by the following equation:

$$S_a = \frac{1}{A} \iint |Z(x, y)| dx dy \quad (\text{Equation 6})$$

where $Z(x, y)$ is the deviation of the manufactured surface from the designed values.

Root mean square deviation Sq evaluated over the complete 3D surface was also analysed to discriminate between surfaces produced at angles from 25 to 90 degrees:

$$S_q = \sqrt{\iint \frac{1}{A} Z^2(x, y) dx dy} \quad (\text{Equation 7})$$

Largest peak height (Sp), valley depth (Sv) and maximum height within the definition area were evaluated as:

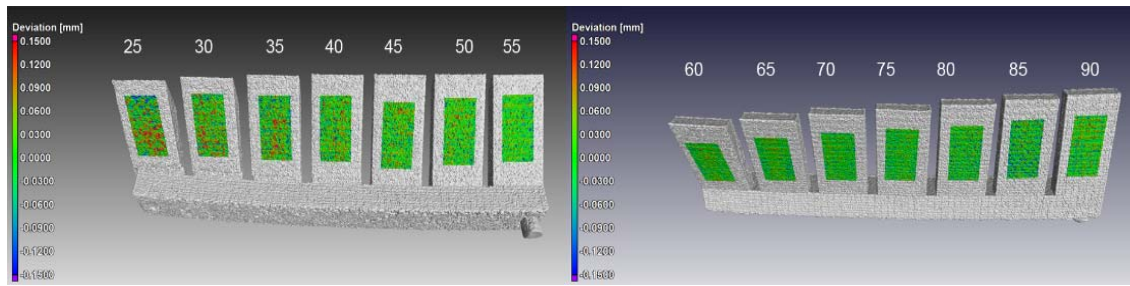
$$S_p = \max_A Z(x, y) \quad S_v = \min_A Z(x, y) \quad S_z = S_v + S_p \quad (\text{Equation 8})$$

Skewness of the surface (Ssk) that represents the degree of symmetry of the surface heights measured correspondingly designed surface, was calculated from deviation $Z(x, y)$ as:

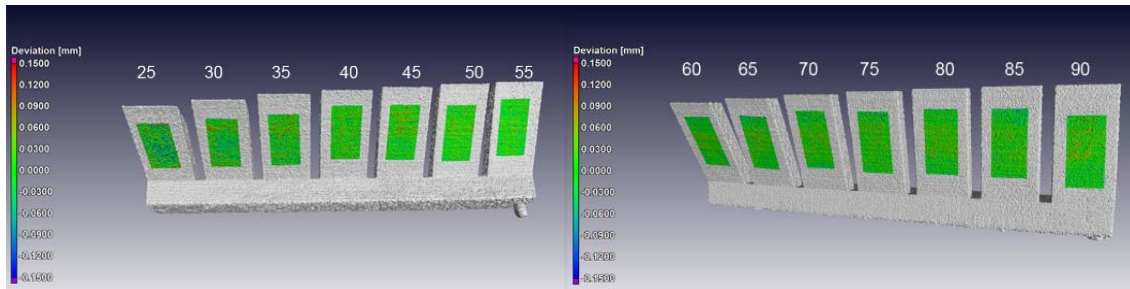
$$S_{sk} = \frac{1}{S_q^3} \left[\frac{1}{A} \iint Z^3(x, y) dx dy \right] \quad (\text{Equation 9})$$

It is important to note that the sign of the skewness indicates the predominance of peaks ($S_{sk} > 0$) or valleys ($S_{sk} < 0$) of the surface.

A representation of the surface roughness of downskin surfaces for sets A and B is shown in Figure 44 respectively as colour heights maps. Set A had higher roughness for all angles (Figure 44, Table 4).



(a)



(b)

Figure 44: MicroCT reconstruction of surfaces versus an inclination angle: set A (a) and set B (b).

It should also be noted that the S_a and S_q values are improved as the inclination angle is increased up to 55° , whereas roughness was more or less stable (Figure 45, Table 4). An angle of 25° for both set A ($90 \mu\text{m}$) and set B ($60 \mu\text{m}$) had the worst surface roughness with a linear decrease of S_q , which can be observed until angle 55° (Figure 45).

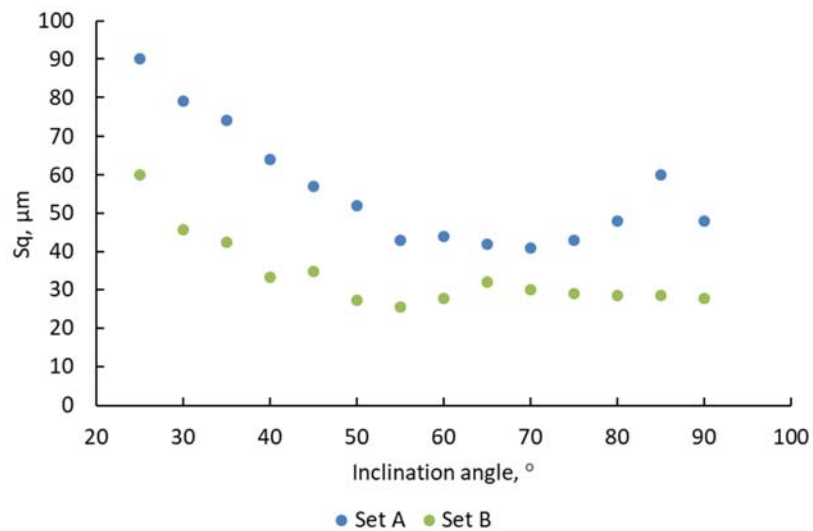


Figure 45: MicroCT measured root mean square deviation S_q evaluated over surfaces *versus* inclination angle.

Table 4: Area roughness of downskin surfaces as per CT scans

Inclination angle	Sa, μm		Sq, μm		Sp, μm		Sv, μm		Ssk	
	set A	set B	set A	set B	set A	set B	set A	set B	set A	set B
25°	83	54	90	60	347	195	304	185	0.4	-0.3
30°	73	39	79	46	262	209	320	152	0.4	0.2
35°	68	36	74	43	243	205	279	141	0.1	0.7
40°	56	27	64	33	239	140	266	140	0.2	0.9
45°	49	28	57	35	224	186	218	124	0.3	1.0
50°	45	22	52	27	177	143	201	98	0.1	1.0
55°	35	20	43	26	158	130	189	105	-0.3	0.5
60°	37	23	44	28	164	86	171	129	0	0.1
65°	35	26	42	32	187	117	188	151	-0.3	0
70°	35	25	41	30	151	110	173	117	-0.6	0.4
75°	36	24	43	29	140	142	176	130	-0.6	0.4
80°	41	24	48	29	168	147	195	112	-0.7	0.8
85°	52	23	60	29	155	91	218	123	-1.0	0.1
90°	41	23	48	28	192	154	158	84	0.2	1

The formation of the decreasing roughness with an increasing angle can be attributed to factors such as improved stair-stepping effect and diminishing heat dissipation into loose powder. In addition, Poyraz *et al.* [74] stated that poor surface quality can be attributed to the lack of heat dissipation for unsupported objects. On the other hand, set A shows the downward trend and set B, after angle increment from 40°, had roughness that was independent on inclination angle. However, the expected/normal was regained at 25° to 55° where the surface roughness decreased due to an increase of the building angle.

Another important observation is that the orientation of the samples also influenced the outcome of the results. When comparing the difference in roughness for set A and set B (Table 4), at an angle of 25°, set A reports a roughness value Sq of 90 μm compared with set B which reports 60 μm at the same angle of 25°. A similar observation can be made at a higher angle, i.e. 55° reports roughness of 43 μm for set A while set B reports 26 μm at the same angle of 55°. For vertical samples, Sq also for set A was 1.7 times higher in comparison with set B. This difference can be attributed to the scanning strategy that was used for manufacturing these samples. For set A, downskin roughness was formed by lateral sides (Figure 46a) and “bottom

parts” of the scanned tracks; in set B, start-stop surfaces of single track layers were associated with downskin surface (Figure 40b). Contouring was done after scanning the body sample that also contributed to the roughness.

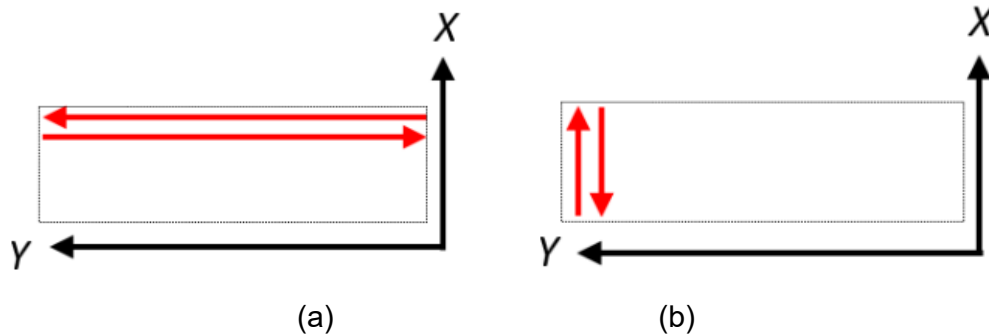


Figure 46: Illustration of the scanning strategy for set A (a) and set B (b), red arrows are scanning direction, grey lines are contouring.

An interesting observation was done when skewness of the surface was analysed: set B had predominant peaks (except 25°) – positive values of S_{sk} – with minimum at 65° inclination angle (Figure 47). For set A, from 25 to 50 degrees, peaks prevailed, then from 55° valleys started to predominate and S_{sk} had negative values up to 85°. Notch-like surface features of AM samples (such as valleys) can act as stress-concentration sites when the sample is loaded, and it is related to poor fatigue properties [103]. Conversely, peaks are not expected to act as stress concentrators. The maximum height of the surface that summarises the peak and valley height ($S_z = S_p + S_v$) is shown in Figure 48. By using microCT scans, S_z values of 300–600 μm were found for set A samples, and 200–400 μm for set B.

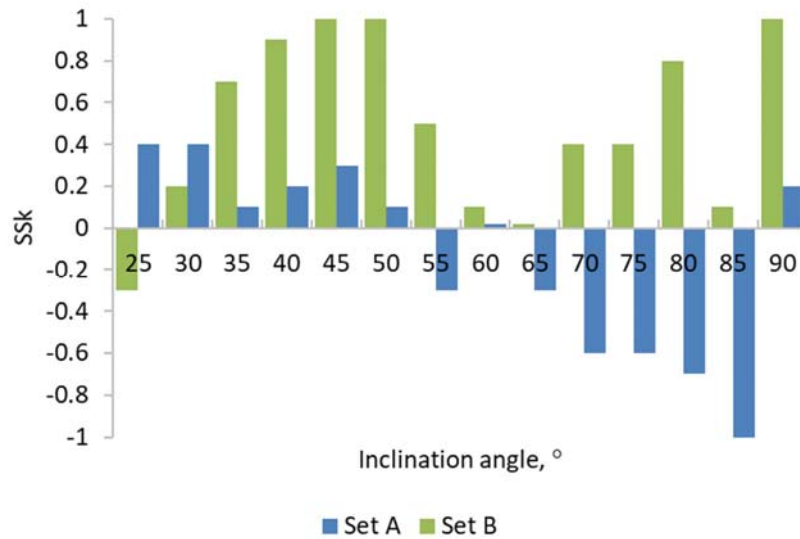


Figure 47: Ssk evaluated over surfaces versus inclination angle for sets A and B.

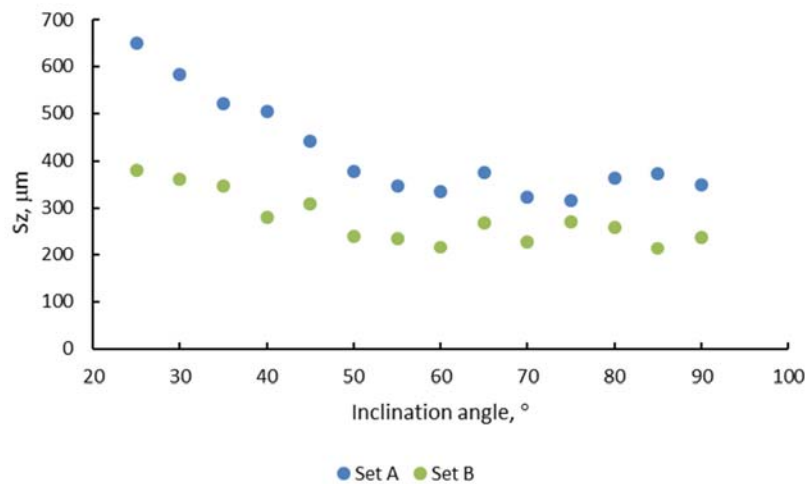


Figure 48: Maximum height Sz evaluated over surfaces versus inclination angle for sets A and B.

On the whole, surface roughness evaluated by CT scans was higher than measured by the contact-type surface roughness instrument. Both methods confirmed that for the chosen scanning strategy, optimal process-parameters and layer thickness, lower roughness was observed in set B, i.e. (XZ) orientation. Thus, it is preferable to build parts at XZ-orientation in order to get an improved surface finish.

4.1.2.2. Qualitative analysis for surface roughness by optical microscope

The increase in the level of surface roughness at low inclination is represented as colour heights in the form of peaks (red) and valleys (deep blue), Figure 49. The images were obtained using a 3D Smartzoom 5 digital microscope for three inclination angles (25° , 65° , 90°) for set A which achieved the worst surface roughness. Peaks and valleys are more pronounced at angle 25° in Figure 49 (a) and improve as the angle increases. Triantaphyllou *et al.* [107] explained that the increased roughness for downskin surfaces is a result of gravity and capillary forces where the melt pool sags into the unmelted powder particles. Furthermore, as the melt pool solidifies, it causes the surrounding unmelted powder particles to attach to the surface, thereby increasing roughness.

In Figure 50, the number of peaks and valleys are not as clearly visible when compared with Figure 49 for the downskin surface. The levels of surface roughness observed on the images agree with the plotted data for both upskin and downskin surfaces.

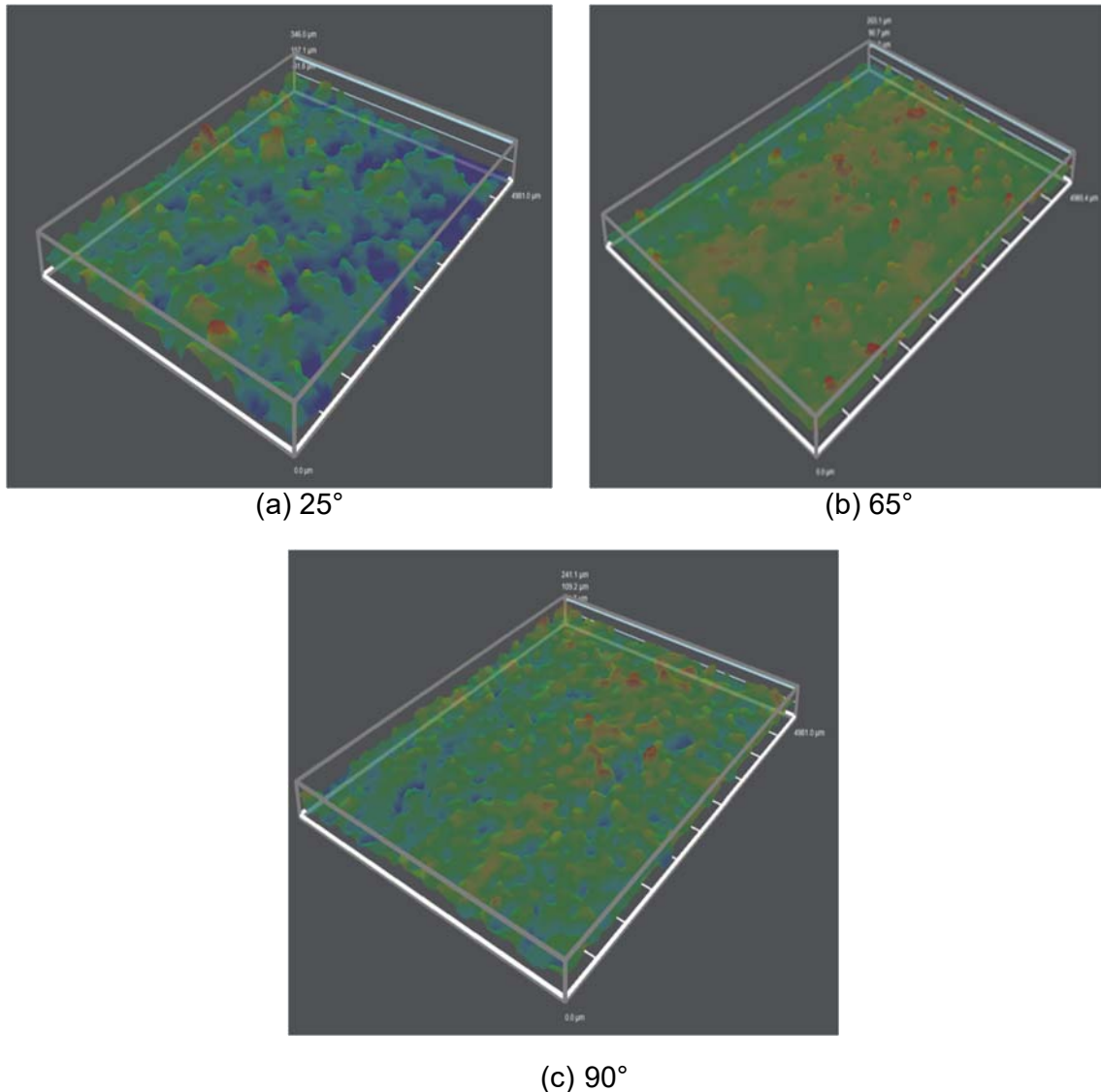


Figure 49: Illustration of surface roughness for the downskin surface for angles 25°, 65° & 90° respectively.

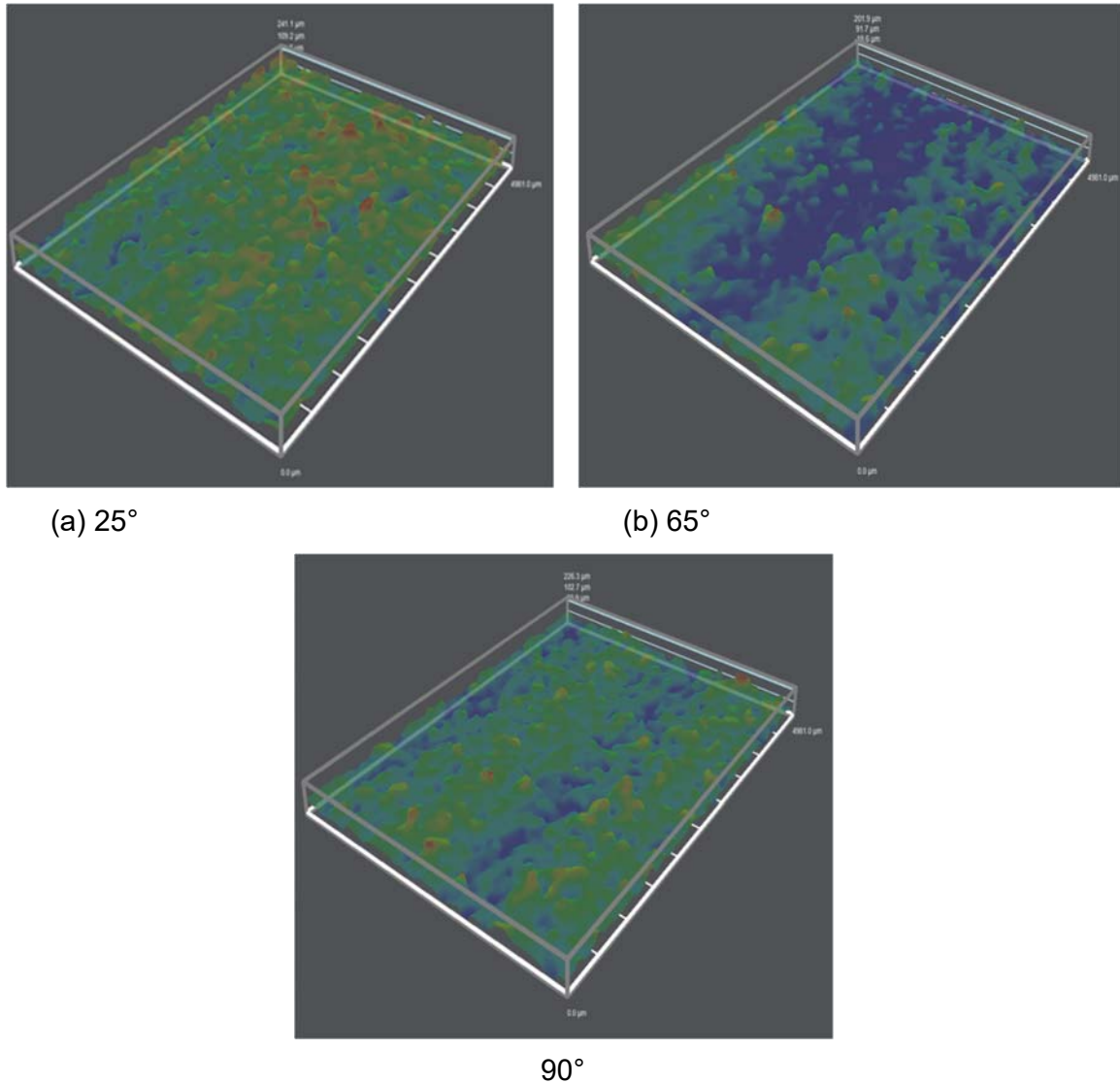


Figure 50: Illustration of surface irregularities using 3D Zeiss Smartzoom 5 digital microscope for angle 25°, 65° & 90° respectively.

4.1.2.3. Surface characterisation using SEM

The downskin surface images obtained using SEM, shown in Figure 51 and Appendix 11, are in agreement with the images shown in the previous section. The downskin surface images show higher agglomeration of powder particles at 25° which improved at an increased inclination angle of 90°. However, for the upskin surface, images show that powder agglomeration is the opposite of the downskin surface. Layers are clearly visible at 25° and 30° angles. However, at angle 90° powder particles can be observed as a dominant feature.

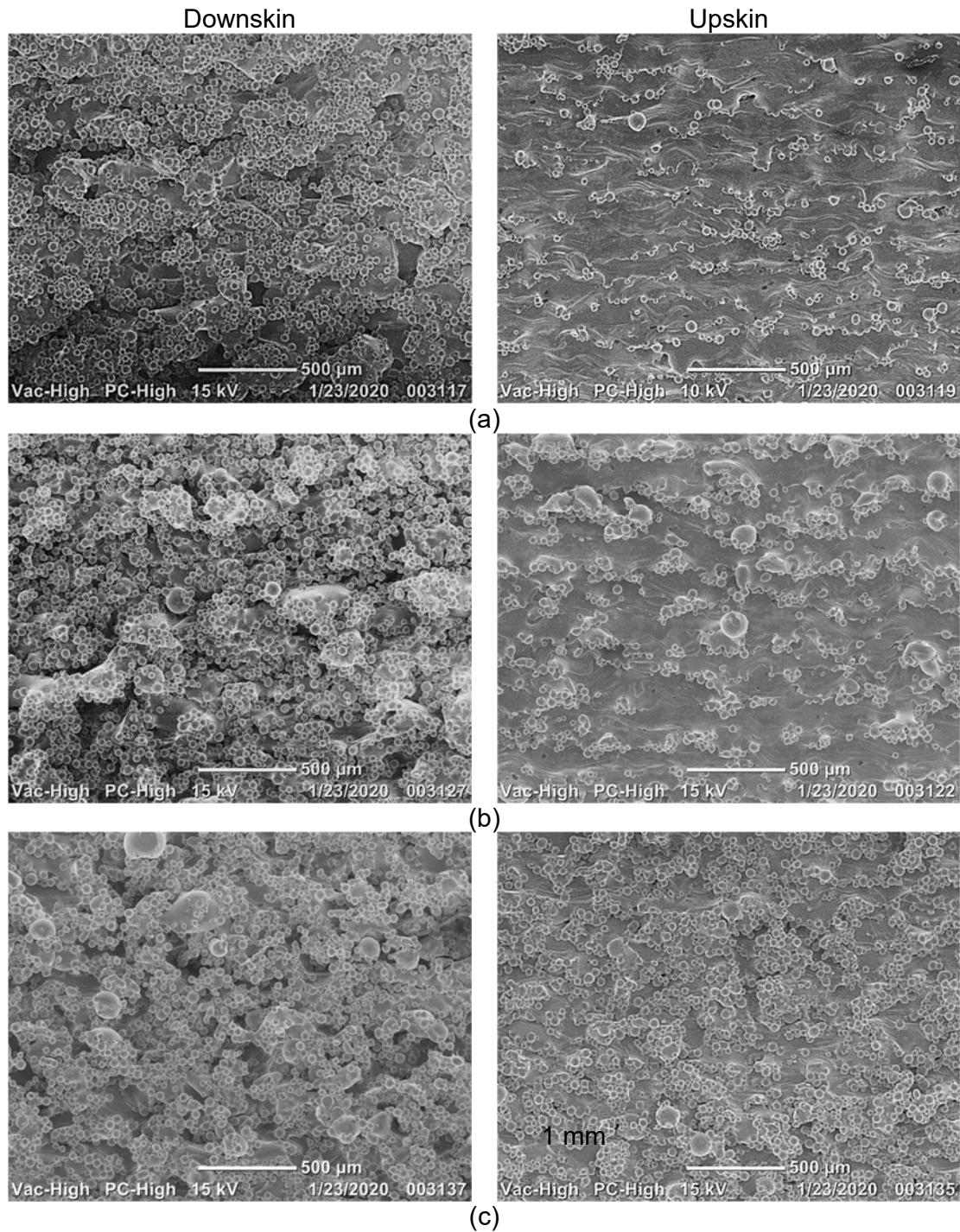


Figure 51: SEM images illustrating surface roughness for different inclination angles of 25° (a), 30° (b) and 90°(c) respectively.

4.2. Surface roughness and porosity

Figure 52 and Figure 53 show the images obtained on the optical microscope for cross-sections of sets A and B. The levels of surface roughness attained, as shown in the images, agree with the measured 2D and CT scanned results (Figure 42 and Figure 44). The images suggest that the surface roughness is also affected by the way the samples are orientated on the build plate during processing: surfaces that were formed along the long side (set A) have more rough surface in comparison with set B where surfaces were formed by ends and starts of the tracks and contour (Figure 46).

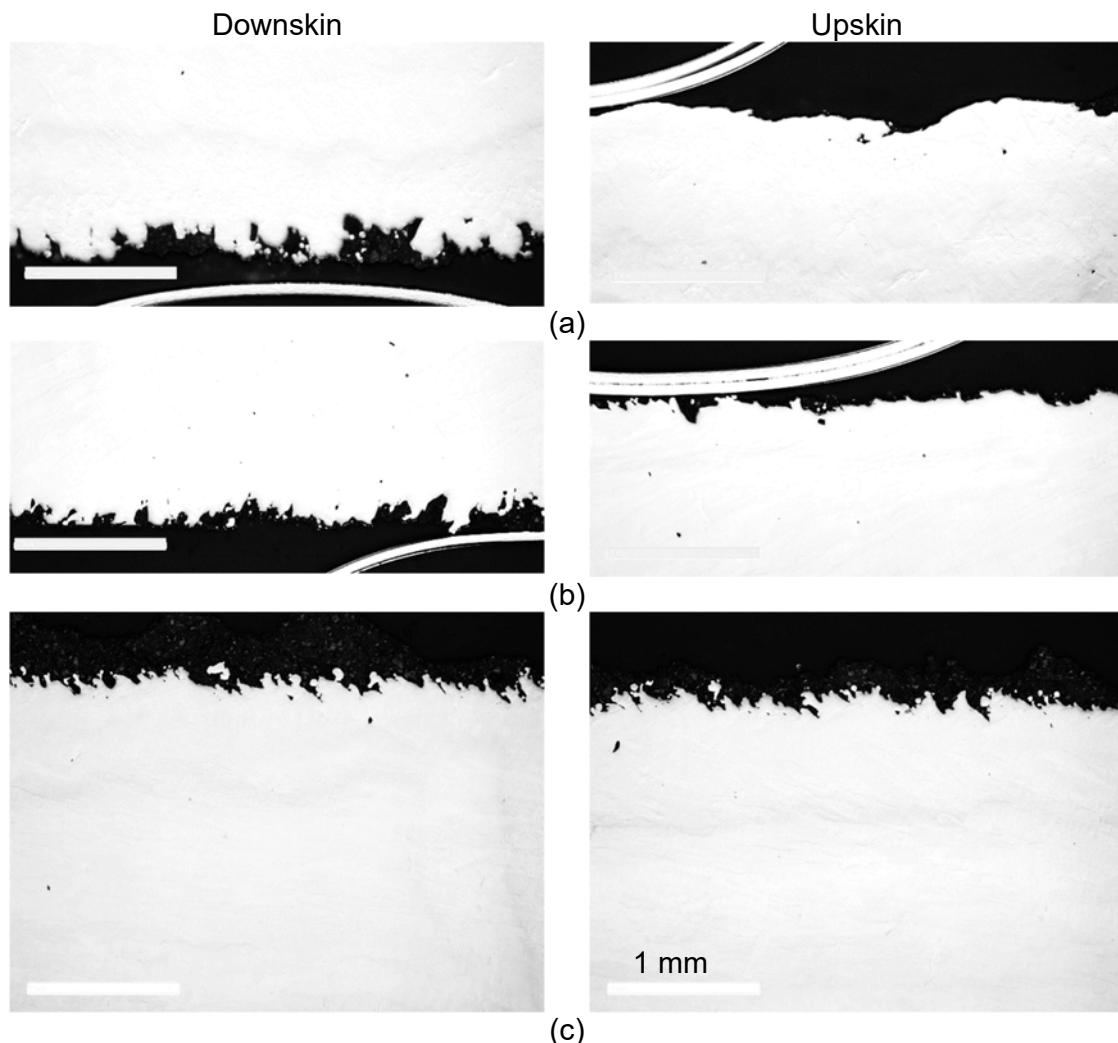


Figure 52: Optical microscope cross-sections of downskin surfaces for set A at inclinations of 25° (a), 55° (b) and 90° (c) respectively.

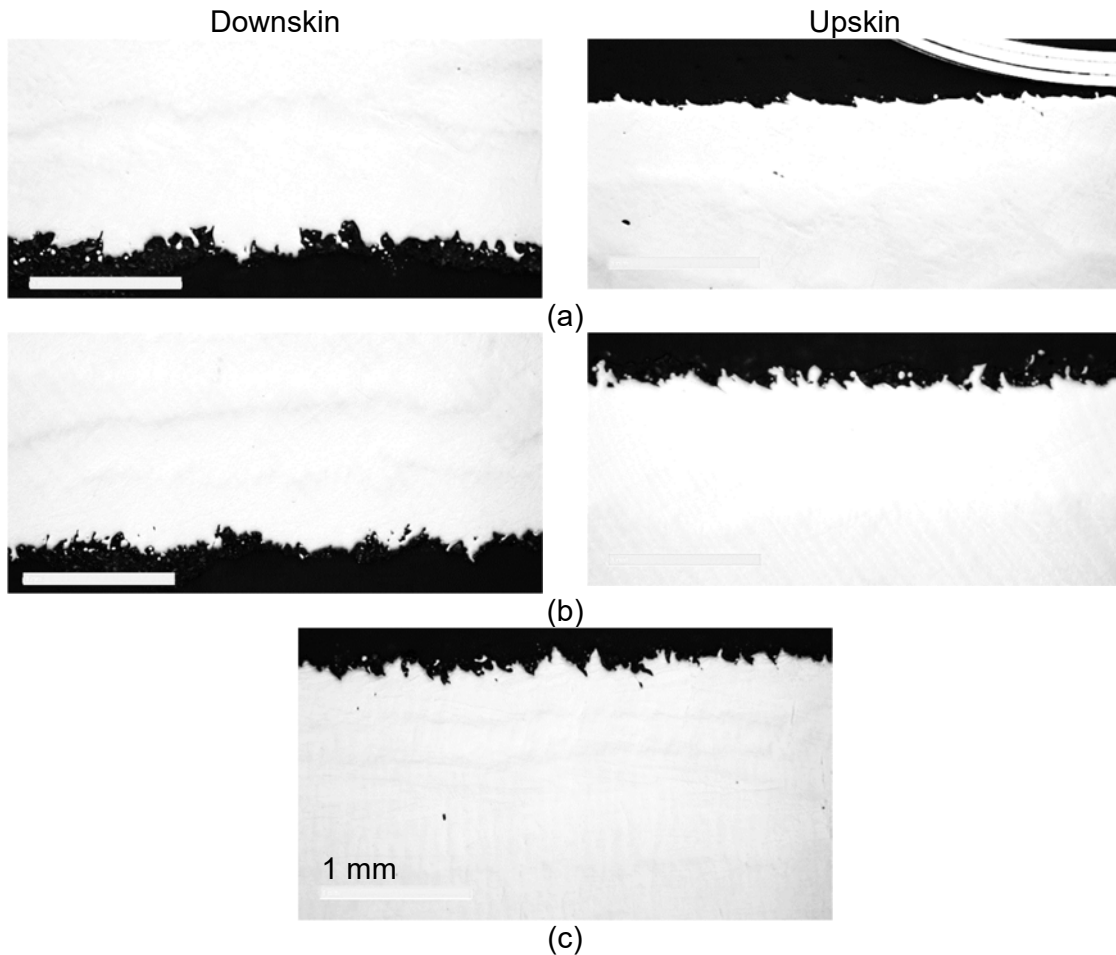


Figure 53: Optical microscope cross-sections of downskin surfaces for set B at inclinations of 25° (a), 55° (b) and 90° (c) respectively.

It is evident that Rz values can be used from a tolerance point of view – for estimating how much material needs to be removed, in the case of machining, for example.

The relationship between the porosity and inclination angle was determined by CT scans (Figure 54). CT scan results are shown in Appendices 9 and 10. Generally, porosity was small, but agglomerations of powder attached on upskin surface were classified as pores in set A. Set A near-downskin experienced porosity between 0.06 to 0.02% and set B had a maximum of 0.02 to 0.01%. It should be noted that the porosity improved as the angle increased from 25° to 55°. However, the porosity results for both set A and set B for all inclination angles are below 0.1% which suggests that the samples are dense. Figure 55b shows the measurement for pore

diameter compared to an inclination angle. For set A, the pore diameter ranged between 150–400 μm whereas sample B was 100–200 μm . These results agree with results received by cross-sectioning (Figure 52 and Figure 53). Overall, high roughness lead to near-surface porosity (Figure 56), but other parameters also influence the density of LPBF parts.

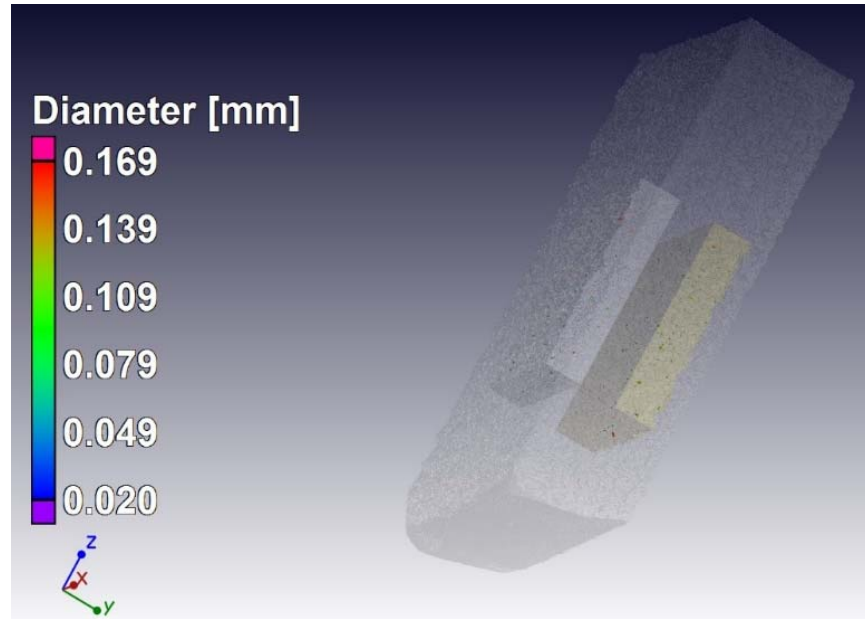
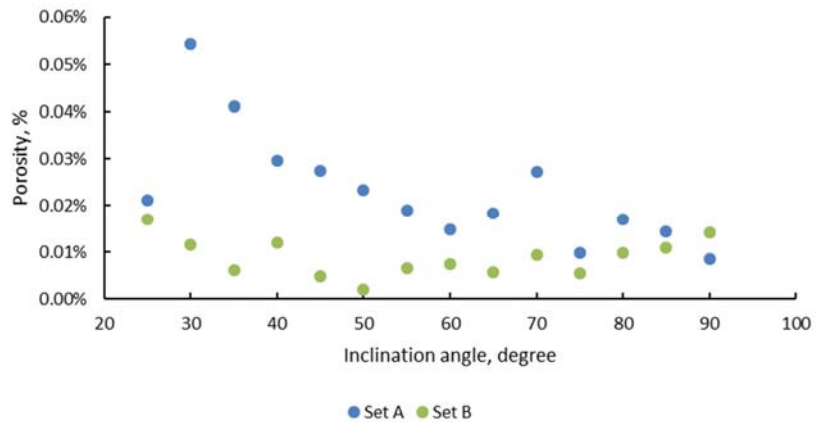
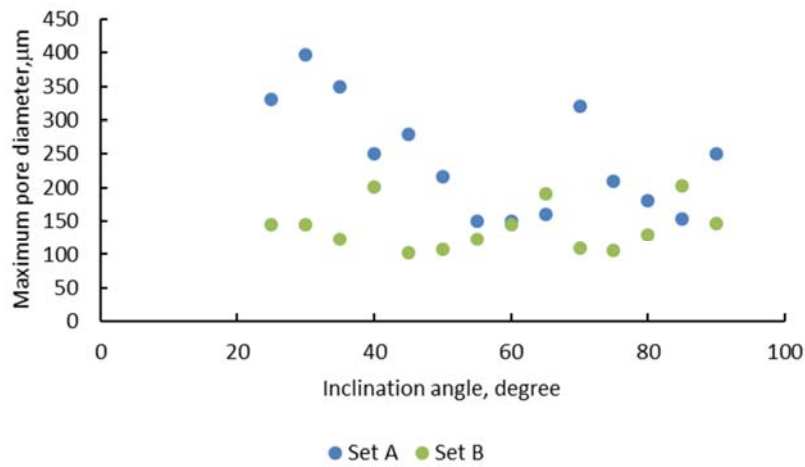


Figure 54: Defect analysis of near-upskin (left) and downskin (right) by CT scans.



(a)



(b)

Figure 55: Porosity and maximum pore size for near-downskin areas for samples A and B.

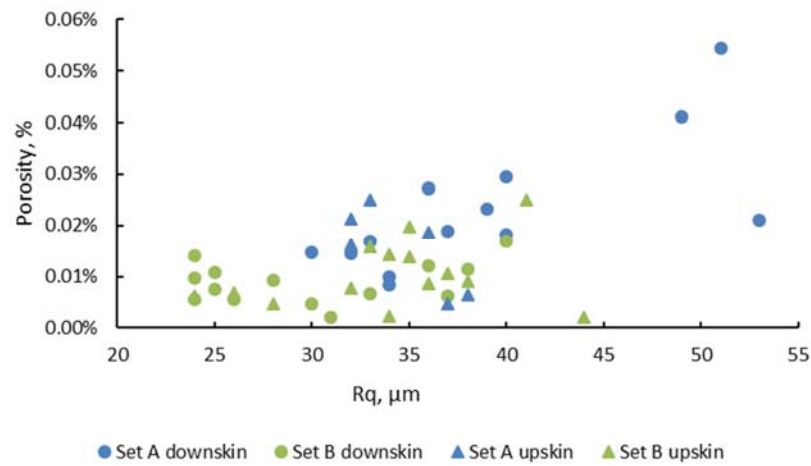


Figure 56: Porosity and Rq surface roughness for samples A and B.

As previously shown in [39], formation of single tracks at high scanning speed is a very sensitive process and can lead to instability of single tracks. It was also found that there is a consecutive reduction of the powder consolidation zone during scanning that leads to different geometrical sizes and shapes of single tracks and layer morphology that, in turn, cause inter-track or inter-layer porosity. But the overall porosity results affirm that it is possible to build using high scanning speed, higher laser power and larger layer thickness without greatly affecting density of the part (Figure 57). However, surface roughness of these parts is quite high.

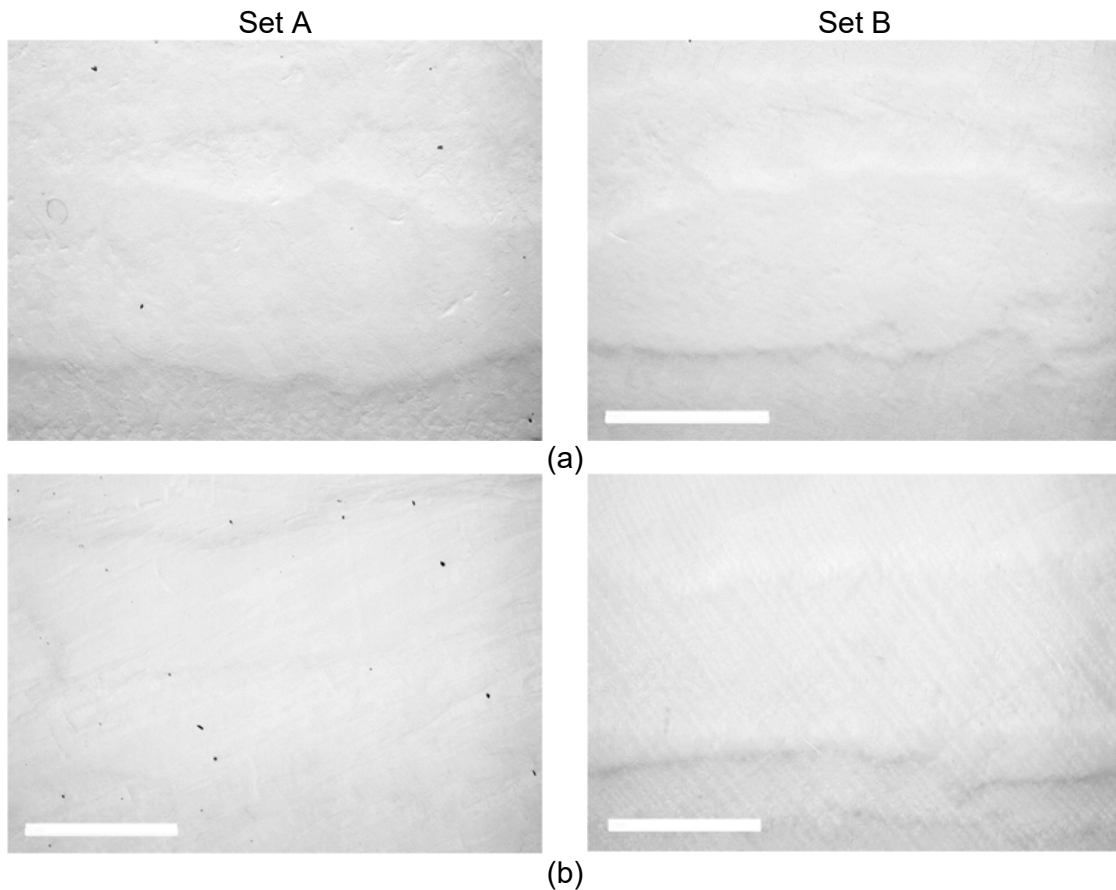


Figure 57: Cross-sections of sets A and B at inclinations of 25° (a) and 55° (b) respectively.

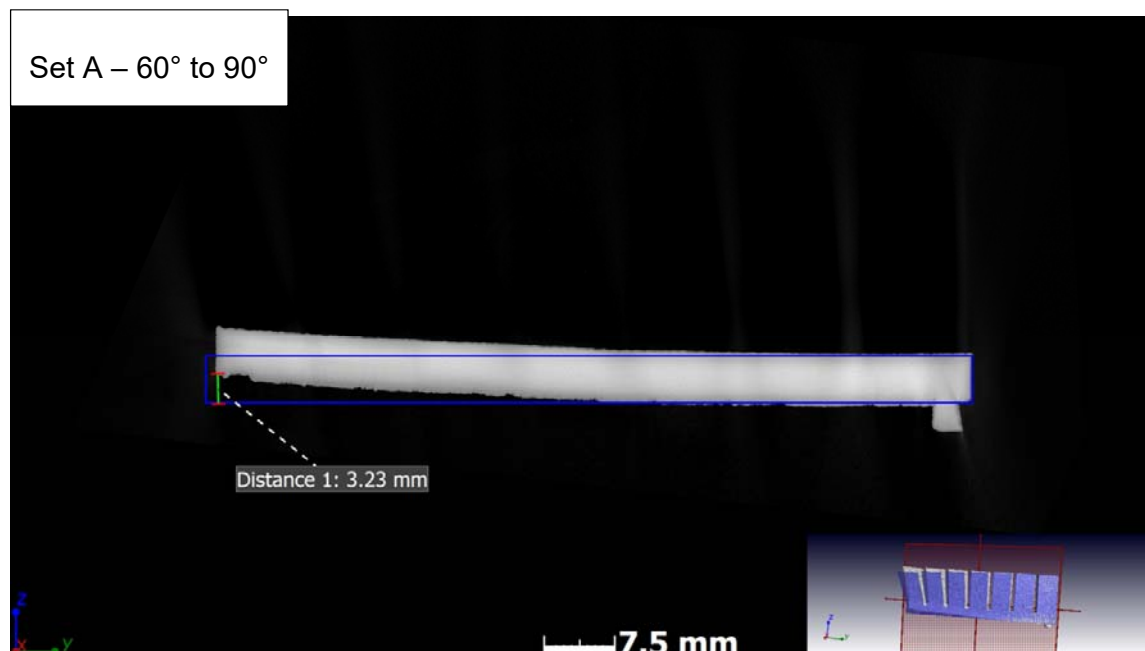
4.3. Deformation of the as-built samples

High residual stress leads to the deformation of samples during LPBF and after separation from the solid base plate, as shown in Figure 58. The blue colour on the design file shows that the actual parts have higher deformation for set A. It is known

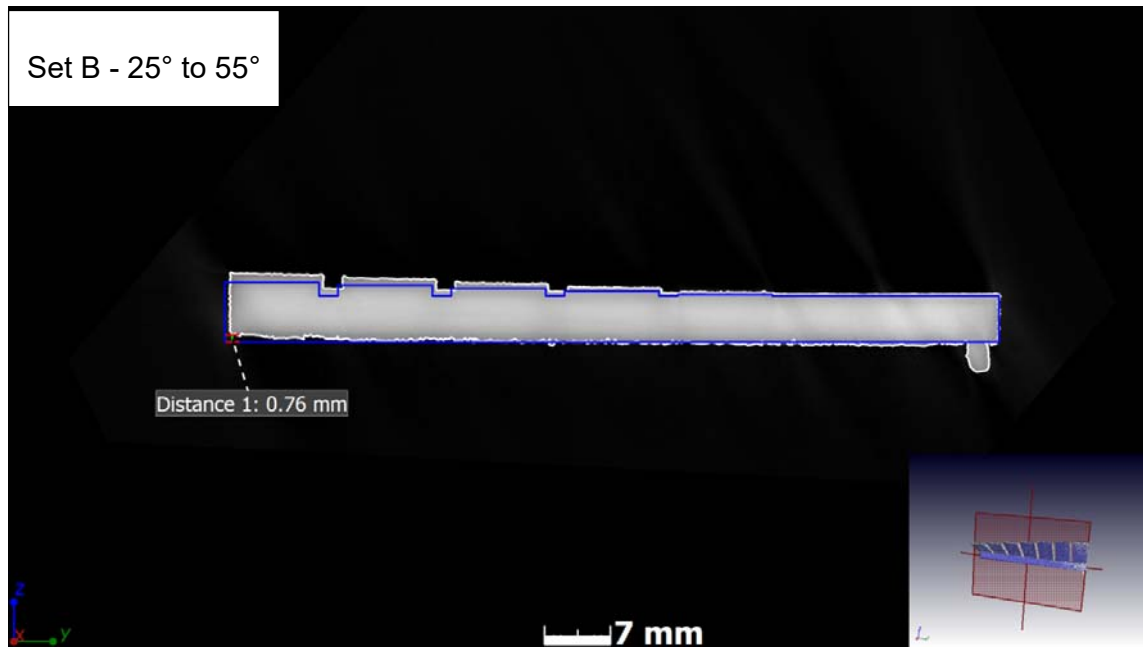
that maximal principle stress in LPBF samples develops along the scanning direction [105].



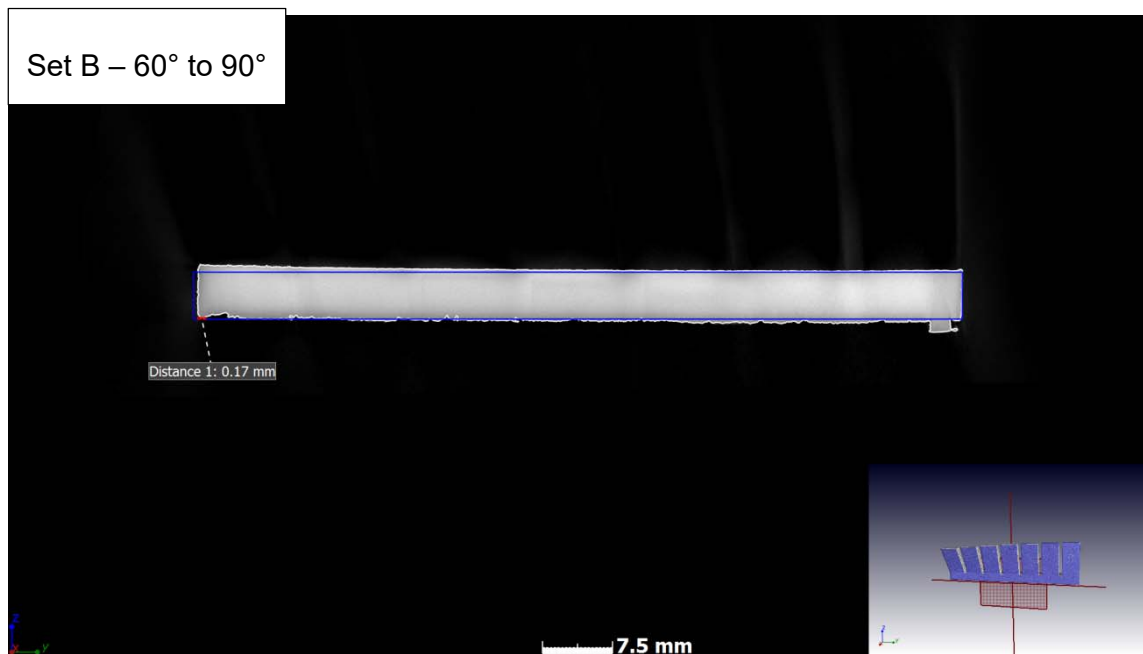
(a)



(b)



(c)



(d)

Figure 58: MicroCT scans of LPBF samples manufactured at different inclination angles versus designed shape coded with blue colour, from left to right – set A: 25–55° (a), 60–90° (b); set B: 25–55° (c), 60–90° (d).

In chapter 3 (Materials and Methods), it was shown that test artefacts were manufactured on solid blocks that were scanned in a similar way with parallelepipeds (Figure 34). Accumulation of residual stress in samples from set A, that were scanned along the long side (Y-direction in Figure 34), caused higher deformation in comparison with the set B after separation from the solid base plate: maximum warping of 3.92 mm & 3.23 mm in Z-direction was measured in set A *versus* 0.76 mm and 0.17 mm in set B. These findings are in agreement with Hussein *et al.* [21] that thermal gradients within the layer rise due to long track length of the laser beam whereas homogenous temperatures are produced within shorter lengths.

Summary

This chapter analysed the surface roughness measurements of test artefacts at four different orientations. Initially, four orientations were investigated, i.e. Set A and D (YZ-orientation); Set B and C (XZ-orientation). From there, two orientations (Set A and Set B) were chosen for in-depth investigation. It was determined that the surface roughness is affected by the inclination angle, and the surface for all orientations improves as the angle is increased. Overall, better roughness results were achieved on set B. This agrees with the 2D images obtained on the optical microscope where set A achieved the worst surface roughness together with surface pores close to the surface. Differences in roughness values, which were determined by profile measurements with roughness meter and CT scans, required further study. Deformations, void filling and filtering operations can influence results [108]. It must be noted that CT data were received with primary surface without filtering which can be the reason for higher values of surface roughness than measured by contact profilometer. The roughness for sets A and B showed that having optimised parameters did not have a great effect on the density of the samples. The overall porosity was found to be below 0.1% which suggests that the samples were fairly dense for all angles. When comparing deformations for set A (block with 25–55° samples and second block with 60–90°) and set B samples on how they were scanned during processing, set A deformations of 3.92 mm and 3.23 mm; while set B measured deformations of 0.76 mm and 0.17 mm respectively. This suggests that the way samples are scanned during processing influences the degree of deformation.

CHAPTER 5: CONCLUSION AND RECOMMENDATIONS

Conclusions

The surface roughness at low inclination angle (25° to 45°) for the downskin surface is mostly influenced by partially sintered powder particles. This is the result of melt pool solidifying on top of loose powder which sticks to the surface. The upskin surface is affected by powder particles at higher inclination angles. These findings were validated by the SEM. At lower inclination angles, surface roughness is affected by the stair-stepping effect for both the upskin and the downskin surface which improves as the inclination angle increases. This is attributed to the type of manufacturing technique used.

In terms of scanning direction: surface roughness is affected by the scanning direction. Samples should be orientated in such a way as to minimise the length of the tracks when using a bi-directional strategy in order to attain better surface quality and lower deformations.

Using only 2D parameters (R_a , R_q and R_z) to characterise surface roughness proved not to be sufficient to gather the required analysis. The use of other instruments for analysis, such as the SEM, OM, digital microscope and 3D surface roughness measurement by microCT, provided a better insight into understanding the changes occurring on the surface of the samples.

The study showed that the inclination angle does not affect the level of porosity when processing parameters are properly optimised. It was also determined that higher laser power and scanning speed are capable of producing dense samples with porosity levels of less than 0.1%. Higher levels of pores were found closer to sample surfaces with maximum pore diameter of $400\text{ }\mu\text{m}$ for set A and $200\text{ }\mu\text{m}$ for set B. The surface pores occurred as a result of a combination of powder sticking to the surface and melt pool instability due to higher processing parameters. In addition, cross-sectioned samples proved that the internal surfaces of the samples were dense although the single tracks were irregular as a result of processing parameters. The higher processing parameters combined with inclination angle only affected the level of surface quality.

Recommendations for future work

- Investigate contour parameters on the Aeroswift machine.
 - This will help improve the overall surface quality especially for lower inclination angle.
- Investigate the effect of scaling up of processing parameters, i.e. laser power, scan speed and layer thickness.
 - To further study ways of minimising the cause of surface pores on the manufactured samples
- Carry out research on more test artefacts on the Aeroswift machine.
 - This will help to understand the limitations of the Aeroswift machine such as minimum wall thickness and minimum diameters, etc.
- Investigate different types of scanning strategies.
 - This will improve the cooling rates and help to achieve better deformations.

REFERENCES

- [1] De Beer, D.J., Du Preez, W., Greyling, H., Prinsloo, F., Sciammarella, F. and Vermeulen, M.A., 2016, *South African Additive Manufacturing Strategy*. Department of Science and Technology, CSIR, April 2016.
- [2] Diegel, O., Singamneni, S., Reay, S. and Withell, A., 2010. Tools for sustainable product design: additive manufacturing. *Journal of Sustainable Development*, 3 (3), pp. 68-75.
- [3] Atzeni, E. and Salmi, A., 2012. Economics of additive manufacturing for end-usable metal parts. *The International Journal of Advanced Manufacturing Technology*, 62(9-12), pp.1147-1155.
- [4] De Beer, D.J., 2011. Establishment of rapid prototyping/additive manufacturing in South Africa. *Journal of the Southern African Institute of Mining and Metallurgy*, 111(3), pp.211-215.
- [5] Strano, G., Hao, L., Everson, R.M. and Evans, K.E., 2013. A new approach to the design and optimisation of support structures in additive manufacturing. *The International Journal of Advanced Manufacturing Technology*, 66(9-12), pp.1247-1254.
- [6] Panesar, A., Abdi, M., Hickman, D. and Ashcroft, I., 2018. Strategies for functionally graded lattice structures derived using topology optimisation for Additive Manufacturing. *Additive Manufacturing*, 19, pp.81-94.
- [7] Leutenecker-Twelsiek, B., Klahn, C. and Meboldt, M., 2016. Considering part orientation in design for additive manufacturing. *Procedia CIRP*, 50, pp.408-413.
- [8] Seepersad, C.C., 2014. Challenges and opportunities in design for additive manufacturing. *3D Printing and Additive Manufacturing*, 1(1), pp.10-13.
- [9] Thompson, M.K., Moroni, G., Vaneker, T., Fadel, G., Campbell, R.I., Gibson, I., Bernard, A., Schulz, J., Graf, P., Ahuja, B. and Martina, F., 2016. Design for Additive Manufacturing: Trends, opportunities, considerations, and constraints. *CIRP annals*, 65(2), pp.737-760.

- [10] Kumke, M., Watschke, H. and Vietor, T., 2016. A new methodological framework for design for additive manufacturing. *Virtual and Physical Prototyping*, 11(1), pp.3-19.
- [11] Mani, M., Witherell, P. and Jee, H., 2017, August. Design Rules for Additive Manufacturing: A Categorization. In: *ASME 2017 International Design Engineering Technical Conferences and Computers and Information in Engineering Conference* (pp. V001T02A035-V001T02A035). American Society of Mechanical Engineers.
- [12] Klahn, C., Leutenecker, B. and Meboldt, M., 2015. Design strategies for the process of additive manufacturing. *Procedia CIRP*, 36, pp.230-235.
- [13] Wang, D., Yang, Y., Yi, Z. and Su, X., 2013. Research on the fabricating quality optimization of the overhanging surface in SLM process. *The International Journal of Advanced Manufacturing Technology*, 65(9-12), pp.1471-1484.
- [14] Covarrubias, E.E. and Eshraghi, M., 2018. Effect of build angle on surface properties of nickel superalloys processed by selective laser melting. *JOM*, 70(3), pp.336-342.
- [15] Calignano, F., 2014. Design optimization of supports for overhanging structures in aluminium and titanium alloys by selective laser melting. *Materials & Design*, 64, pp.203-213.
- [16] Baskett, R., 2017. *Effects of support structure geometry on SLM induced residual stresses in overhanging features*. MSc thesis, California Polytechnic State University, San Luis Obispo, 102 p.
- [17] Cloots, M., Spierings, A. and Wegener, K., 2013, August. Assessing new support minimizing strategies for the additive manufacturing technology SLM. In *proc.: Solid Freeform Fabrication Symposium*, Austin, Texas (pp. 631-643).
- [18] ASTM F2792-12A Standard Terminology for Additive Manufacturing Technologies, ASTM International, 100 Barr Harbor Drive, West Conshohocken, PA 19428.

- [19] Triantaphyllou, A., Giusca, C.L., Macaulay, G.D., Roerig, F., Hoebel, M., Leach, R.K., Tomita, B. and Milne, K.A., 2015. Surface texture measurement for additive manufacturing. *Surface Topography: Metrology and Properties*, 3(2), p.024002.
- [20] Brackett, D., Ashcroft, I. and Hague, R., 2011, August. Topology optimization for additive manufacturing. In *Proceedings of the Solid freeform fabrication symposium*, Austin, TX (Vol. 1, pp.348-362). S.
- [21] Hussein, A., Hao, L., Yan, C., Everson, R. and Young, P., 2013. Advanced lattice support structures for metal additive manufacturing. *Journal of Materials Processing Technology*, 213(7), pp.1019-1026.
- [22] Gao, W., Zhang, Y., Ramanujan, D., Ramani, K., Chen, Y., Williams, C.B., Wang, C.C., Shin, Y.C., Zhang, S. and Zavattieri, P.D., 2015. The status, challenges, and future of additive manufacturing in engineering. *Computer-Aided Design*, 69, pp.65-89.
- [23] Gibson, I., Rosen, B., Stucker, B. 2015. *Additive Manufacturing Technologies 3D Printing, Rapid Prototyping and Direct Digital Manufacturing*, Springer, 498 p.
- [24] Moylan, S., Slotwinski, J., Cooke, A., Jurrens, K. and Donmez, M.A., 2012, August. Proposal for a standardized test artifact for additive manufacturing machines and processes. In *Proceedings of the 2012 annual international Solid freeform fabrication symposium* (pp.6-8). Austin, TX.
- [25] Manfredi, D., Calignano, F., Krishnan, M., Canali, R., Ambrosio, E.P., Biamino, S., Ugues, D., Pavese, M. and Fino, P., 2014. Additive manufacturing of Al alloys and aluminium matrix composites (AMCs). *In Light metal alloys applications*. InTech. DOI: 10.5772/58534.
- [26] Huang, S.H., Liu, P., Mokasdar, A. and Hou, L., 2013. Additive manufacturing and its societal impact: a literature review. *The International Journal of Advanced Manufacturing Technology*, 67(5-8), pp.1191-1203.

- [27] Levy, G.N., Schindel, R. and Kruth, J.P., 2003. Rapid manufacturing and rapid tooling with layer manufacturing (LM) technologies, state of the art and future perspectives. *CIRP Annals-Manufacturing Technology*, 52(2), pp.589-609.
- [28] Zhai, Y., Lados, D.A. and LaGoy, J.L., 2014. Additive manufacturing: making imagination the major limitation. *JOM*, 66(5), pp.808-816.
- [29] Bremen, S., Meiners, W. and Diatlov, A., 2012. Selective laser melting: a manufacturing technology for the future? *Laser Technik Journal*, 9(2), pp.33-38.
- [30] Dana, M., Zetkova, I. and Hanzl, P., 2016. Need for support structures depending on overhang size. *MM (Modern Machinery) Science Journal*, December, pp.1597-1601.
- [31] Pinkerton, A.J., 2016. Lasers in additive manufacturing. *Optics & Laser Technology*, 78, pp.25-32.
- [32] Lee, H., Lim, C.H.J. Low, M. J., Tham, N., Murukeshan, V. M., Kim Y-J., 2017. Lasers in Additive Manufacturing: A Review. *International Journal of Precision Engineering and Manufacturing-Green Technology*. 4 (3), pp.307-322.
- [33] Ready, J.F. and Farson, D.F. eds., 2001. *LIA handbook of laser materials processing*. Orlando: Laser Institute of America, 715 p.
- [34] Assunção, E., Quintino, L. and Miranda, R., 2010. Comparative study of laser welding in tailor blanks for the automotive industry. *The International Journal of Advanced Manufacturing Technology*, 49(1-4), pp.123-131.
- [35] Duley, W.W. 1998. Laser welding. New York: Wiley, pp.187-195.
- [36] Tian, Y., Tomus, D., Rometsch, P. and Wu, X., 2017. Influences of processing parameters on surface roughness of Hastelloy X produced by selective laser melting. *Additive Manufacturing*, 13, pp.103-112.
- [37] Bian, Q., Tang, X., Dai, R., Wang, Q. and Zeng, M., 2017. Investigation on the transient phenomena during the evolution of melt pool. *Energy Procedia*, 142, pp.3876-3881.

- [38] Cheng, B., Loeber, L., Willeck, H., Hartel, U., Tuffile, Ch., 2019. Computational investigation of melt pool process dynamics and pore formation in laser powder bed fusion. *Journal of Materials Engineering and Performance*, 28 (11), pp.1544-1024.
- [39] Yadroitsev, I. Direct manufacturing of 3D-objects by selective laser melting of metal powders, Saarbrücken: LAP Lambert Academic Publishing AG & Co, 297 p.
- [40] Manfredi, D., Calignano, F., Krishnan, M., Canali, R., Ambrosio, E.P., Biamino, S., Ugues, D., Pavese, M. and Fino, P., 2014. Additive manufacturing of Al alloys and aluminium matrix composites (AMCs). *Light Metal Alloys Applications*, 11, pp.3-34.
- [41] Vock, S., Klöden, B., Kirchner, A., Weißgärber, T., Kieback, B., 2019. Powders for powder bed fusion: a review. *Progress in Additive Manufacturing*, 4(4), pp. 383-397.
- [42] Zhang, J., Gu, D., Yang, Y., Zhang, H., Chen, H., Dai, D., Lin, K. 2019. Influence of particle size on laser absorption and scanning track formation mechanisms of pure tungsten powder during selective laser melting. *Engineering*, 5(4), pp.736-745.
- [43] Liu, B., Wildman, R., Tuck, C., Ashcroft, I. and Hague, R., 2011. *Investigation the effect of particle size distribution on processing parameters optimisation in selective laser melting process*. Additive Manufacturing Research Group, Loughborough University, pp.227-238.
- [44] Antony, K. and Arivazhagan, N., 2015. Studies on energy penetration and Marangoni effect during laser melting process. *Journal of Engineering Science and Technology*, 10(4), pp. 509-525.
- [45] Di, W., Yongqiang, Y., Xubin, S. and Yonghua, C., 2012. Study on energy input and its influences on single-track, multi-track, and multi-layer in SLM. *The International Journal of Advanced Manufacturing Technology*, 58(9-12), pp.1189-1199.

- [46] Shipley, H., McDonnell, D., Culleton, M., Coull, R., Lupoi, R., O'Donnell, G. and Trimble, D., 2018. Optimisation of process parameters to address fundamental challenges during selective laser melting of Ti-6Al-4V: A review. *International Journal of Machine Tools and Manufacture*, 128, pp.1-20.
- [47] Kruth, J.P., Levy, G., Klocke, F. and Childs, T.H.C., 2007. Consolidation phenomena in laser and powder-bed based layered manufacturing. *CIRP annals*, 56(2), pp.730-759.
- [48] Yadroitsev, I. and Smurov, I., 2010. Selective laser melting technology: from the single laser melted track stability to 3D parts of complex shape. *Physics Procedia*, 5, pp.551-560.
- [49] Yadroitsev, I. and Smurov, I., 2011. Surface morphology in selective laser melting of metal powders. *Physics Procedia*, 12, pp.264-270.
- [50] Sun, D., Gu, D., Lin, K., Ma, J., Chen, W., Huang, J., Sun, X. and Chu, M., 2019. Selective laser melting of titanium parts: Influence of laser process parameters on macro- and microstructures and tensile property. *Powder Technology*, 342, pp.371-379.
- [51] Tolochko, N.K., Mozzharov, S.E., Yadroitsev, I.A., Laoui, T., Froyen, L., Titov, V.I., Ignatiev, M.B., 2004. Balling processes during selective laser treatment of powders. *Rapid Prototyping Journal*, 10(2), pp.78-87.
- [52] Krol, M. and Tański, T., 2016. Surface quality research for selective laser melting of Ti-6Al-4V alloy. *Archives of Metallurgy and Materials*, 61(3), pp.1291-1296.
- [53] Dai, D., Gu, D., Zhang, H., Xiong, J., Ma, C., Hong, C. and Poprawe, R., 2018. Influence of scan strategy and molten pool configuration on microstructures and tensile properties of selective laser melting additive manufactured aluminum based parts. *Optics & Laser Technology*, 99, pp.91-100.
- [54] Dong, Z., Liu, Y., Wen, W., Ge, J. and Liang, J., 2019. Effect of hatch spacing on melt pool and as-built quality during Selective Laser Melting of stainless steel: modeling and experimental approaches. *Materials*, 12(1), p.50.

- [55] Zhang, L.C. and Attar, H., 2016. Selective laser melting of titanium alloys and titanium matrix composites for biomedical applications: a review. *Advanced Engineering Materials*, 18(4), pp.463-475.
- [56] Jhabvala, J., Boillat, E., Antignac, T. and Glardon, R., 2010. On the effect of scanning strategies in the selective laser melting process. *Virtual and physical prototyping*, 5(2), pp.99-109.
- [57] Hanzl, P., Zetek, M., Bakša, T. and Kroupa, T., 2015. The influence of processing parameters on the mechanical properties of SLM Parts. *Procedia Engineering*, 100, pp.1405-1413.
- [58] Qiu, C., Adkins, N.J. and Attallah, M.M., 2013. Microstructure and tensile properties of selectively laser-melted and of HIPed laser-melted Ti-6Al-4V. *Materials Science and Engineering: A*, 578, pp.230-239.
- [59] Yasa, E., Kruth, J.P. and Deckers, J., 2011. Manufacturing by combining selective laser melting and selective laser erosion/laser re-melting. *CIRP annals*, 60(1), pp.263-266.
- [60] Yadroitsev, I., Yadroitsava, I. and Smurov, I., 2011. Strategy of fabrication of complex shape parts based on the stability of single laser melted track. In *Laser-based Micro-and Nanopackaging and Assembly V* (Vol.7921, p.79210C). International Society for Optics and Photonics.
- [61] du Plessis, A., Yadroitsava, I., Yadroitsev, I., 2020. Effects of defects on mechanical properties in metal additive manufacturing: A review focusing on X-ray tomography insights. *Materials & Design*, 187, 108385.
- [62] Herzog, D., Seyda, V., Wycisk, E. and Emmelmann, C., 2016. Additive manufacturing of metals. *Acta Materialia*, 117, pp.371-392.
- [63] Du Plessis, A., 2019. Effects of process parameters on porosity in laser powder bed fusion revealed by X-ray tomography. *Additive Manufacturing*, 30, p.100871.

- [64] Qiu, C., Adkins, N.J. and Attallah, M.M., 2013. Microstructure and tensile properties of selectively laser-melted and of HIPed laser-melted Ti-6Al-4V. *Materials Science and Engineering: A*, 578, pp.230-239.
- [65] Qiu, C., Panwisawas, C., Ward, M., Basoalto, H.C., Brooks, J.W. and Attallah, M.M., 2015. On the role of melt flow into the surface structure and porosity development during selective laser melting. *Acta Materialia*, 96, pp.72-79.
- [66] Yadroitsev, I., Thivillon, L., Bertrand, P. and Smurov, I., 2007. Strategy of manufacturing components with designed internal structure by selective laser melting of metallic powder. *Applied Surface Science*, 254(4), pp.980-983.
- [67] Aboulkhair, N.T., Everitt, N.M., Ashcroft, I. and Tuck, C., 2014. Reducing porosity in AISi10Mg parts processed by selective laser melting. *Additive Manufacturing*, 1, pp.77-86.
- [68] Du Plessis, A., Yadroitsev, I., Yadroitsava, I. and Le Roux, S.G., 2018. X-Ray microcomputed tomography in additive manufacturing: A review of the current technology and applications. *3D Printing and Additive Manufacturing*, 5(3), pp.227-247.
- [69] Liang, X., Chen, Q., Cheng, L., Yang, Q. and To, A., 2017. A modified inherent strain method for fast prediction of residual deformation in additive manufacturing of metal parts. In *Proceedings of Solid Freeform Fabrication (SFF) Conference*.
- [70] Hagedorn-Hansen, D., Bezuidenhout, M.B., Dimitrov, D.M. and Oosthuizen, G.A., 2017. The effects of selective laser melting scan strategies on deviation of hybrid parts. *South African Journal of Industrial Engineering*, 28(3), pp.200-212.
- [71] Järvinen, J.P., Matilainen, V., Li, X., Piili, H., Salminen, A., Mäkelä, I. and Nyrhilä, O., 2014. Characterization of effect of support structures in laser additive manufacturing of stainless steel. *Physics Procedia*, 56(56), pp.p72-81.
- [72] Tounsi, R. and Vignat, F., 2017. New concept of support structures in Electron Beam Melting manufacturing to reduce geometric defects. *15e Colloque National AIP-Priméca. La Plagne (73) – 12 au 14 avril 2017*.

- [73] Yadroitsev, I. and Yadroitsava, I., 2015. Evaluation of residual stress in stainless steel 316L and Ti6Al4V samples produced by selective laser melting. *Virtual and Physical Prototyping*, 10(2), pp.67-76.
- [74] Poyraz, O., Yasa, E., Akbulut, G., Orhangul, A. and Pilatin, S., 2015. Investigation of support structures for direct metal laser sintering (DMLS) of IN625 parts. In *Proceedings of Solid Freeform Fabrication (SFF) Symposium*, Austin, TX.
- [75] Zeng, K., 2015. Optimization of support structures for selective laser melting.
- [76] Morgan, H.D., Cherry, J.A., Jonnalagadda, S., Ewing, D. and Sienz, J., 2016. Part orientation optimisation for the additive layer manufacture of metal components. *The International Journal of Advanced Manufacturing Technology*, 86(5-8), pp.1679-1687.
- [77] Cooper, K., Steele, P., Cheng, B. and Chou, K., 2017. Contact-free support structures for part overhangs in powder-bed metal additive manufacturing. *Inventions*, 3(1), p.2.
- [78] Kajima, Y., Takaichi, A., Nakamoto, T., Kimura, T., Kittikundecha, N., Tsutsumi, Y., Nomura, N., Kawasaki, A., Takahashi, H., Hanawa, T. and Wakabayashi, N., 2018. Effect of adding support structures for overhanging part on fatigue strength in selective laser melting. *Journal of the Mechanical Behaviour of Biomedical Materials*, 78, pp.1-9.
- [79] Jhabvala, J., Boillat, E., André, C. and Glardon, R., 2012. An innovative method to build support structures with a pulsed laser in the selective laser melting process. *The International Journal of Advanced Manufacturing Technology*, 59(1-4), pp.137-142.
- [80] Gordon, E.R., Shokrani, A., Flynn, J.M., Goguelin, S., Barclay, J. and Dhokia, V., 2016. A surface modification decision tree to influence design in additive manufacturing. In *Sustainable Design and Manufacturing 2016* (pp.423-434). Springer, Cham.

- [81] Jiang, J., Stringer, J., Xu, X. and Zhong, R.Y., 2018. Investigation of printable threshold overhang angle in extrusion-based additive manufacturing for reducing support waste. *International Journal of Computer Integrated Manufacturing*, pp.1-9.
- [82] Graziosi, S., Rosa, F., Casati, R., Solarino, P., Vedani, M. and Bordegoni, M., 2017. Designing for metal additive manufacturing: A case study in the professional sports equipment field. *Procedia Manufacturing*, 11, pp.1544-1551.
- [83] Piscopo, G., Salmi, A. and Atzeni, E., 2019. On the quality of unsupported overhangs produced by laser powder bed fusion. *International Journal of Manufacturing Research*, 14(2), pp.198-216.
- [84] Design for Additive Metal Manufacturing. Additive Metal Manufacturing Inc. www.additivemet.com
- [85] Chen, Z., Wu, X., Tomus, D. and Davies, C.H., 2018. Surface roughness of Selective Laser Melted Ti-6Al-4V alloy components. *Additive Manufacturing*, 21, pp.91-103.
- [86] Fox, J.C., Moylan, S.P. and Lane, B.M., 2016. Effect of process parameters on the surface roughness of overhanging structures in laser powder bed fusion additive manufacturing. *Procedia CIRP*, 45, pp.131-134.
- [87] Mertens, R., Clijsters, S., Kempen, K. and Kruth, J.P., 2014. Optimization of scan strategies in selective laser melting of aluminum parts with downfacing areas. *Journal of Manufacturing Science and Engineering*, 136(6), p.061012.
- [88] Barari, A., Kishawy, H.A., Kaji, F. and Elbestawi, M.A., 2017. On the surface quality of additive manufactured parts. *The International Journal of Advanced Manufacturing Technology*, 89(5-8), pp.1969-1974.
- [89] Calignano, F., 2018. Investigation of the accuracy and roughness in the laser powder bed fusion process. *Virtual and Physical Prototyping*, 13 (2), pp.97-104.

- [90] Gebisa, A.W. and Lemu, H.G., 2017, December. A case study on topology optimized design for additive manufacturing. In IOP Conference Series: Materials Science and Engineering (Vol. 276, No.1, p.012026). IOP Publishing.
- [91] Boschetto, A., Bottini, L. and Veniali, F., 2018. Surface roughness and radiusing of Ti6Al4V selective laser melting-manufactured parts conditioned by barrel finishing. The International Journal of Advanced Manufacturing Technology, 94(5-8), pp.2773-2790.
- [92] Mathoho, I., 2017. Enhancing the integrity of machined titanium alloy (Doctoral dissertation, University of Johannesburg).
- [93] Uhlmann, E., Kersting, R., Klein, T.B., Cruz, M.F. and Borille, A.V., 2015. Additive manufacturing of titanium alloy for aircraft components. Procedia CIRP, 35, pp.55-60.
- [94] Buchbinder, D., Schleifenbaum, H.B., Heidrich, S., Meiners, W. and Bültmann, J., 2011. High power selective laser melting (HP SLM) of aluminum parts. Physics Procedia, 12, pp.271-278.
- [95] Townsend, A., Senin, N., Blunt, L., Leach, R.K. and Taylor, J.S., 2016. Surface texture metrology for metal additive manufacturing: a review. Precision Engineering, 46, pp.34-47.
- [96] ISO, E., 1997. 4287–Geometrical Product Specifications (GPS)–Surface Texture: Profile Method–Terms, Definitions and Surface Texture Parameters. International Organization for Standardization: Geneva, Switzerland.
- [97] Gadelmawla, E.S., Koura, M.M., Maksoud, T.M.A., Elewa, I.M. and Soliman, H.H., 2002. Roughness parameters. Journal of Materials Processing Technology, 123(1), pp.133-145.
- [98] Du Plessis, A., le Roux, S.G., Els, J., Booysen, G. and Blaine, D.C., 2015. Application of microCT to the non-destructive testing of an additive manufactured titanium component. Case Studies in Nondestructive Testing and Evaluation, 4, pp.1-7.

- [99] du Plessis, A., Sperling, Ph., Beerlink, A., Kruger, O., Tshabalala, L., Hoosain, Sh., le Roux, S.G., 2018. Standard method for microCT-based additive manufacturing quality control 3: Surface roughness. *MethodsX*, 5, pp.1111-1116.
- [100] Karne, A., Kallonen, A., Matilainen, V.P., Piili, H. and Salminen, A., 2015. Possibilities of CT scanning as analysis method in laser additive manufacturing. *Physics Procedia*, 78, pp.347-356.
- [101] Pyka, G., Kerckhofs, G., Papantoniou, I., Speirs, M., Schrooten, J. and Wevers, M., 2013. Surface roughness and morphology customization of additive manufactured open porous Ti6Al4V structures. *Materials*, 6(10), pp.4737-4757.
- [102] Ayad, M.F., Rosenstiel, S.F. and Hassan, M.M., 1996. Surface roughness of dentin after tooth preparation with different rotary instrumentation. *The Journal of Prosthetic Dentistry*, 75(2), pp.122-128.
- [103] Sedlaček, M., Podgornik, B. and Vižintin, J., 2009. Influence of surface preparation on roughness parameters, friction and wear. *Wear*, 266(3-4), pp.482-487.
- [104] Chan, K. S., 2015. Characterization and analysis of surface notches on Ti-alloy plates fabricated by additive manufacturing techniques. *Surf. Topogr.: Metrol. Prop.* 3, pp.044006, doi:10.1088/2051-672X/3/4/044006
- [105] Van Zyl, I., Yadroitsava, I., Yadroitsev, I., 2016 Residual stress in Ti6Al4V objects produced by direct metal laser sintering. *The South African Journal of Industrial Engineering*, 27 (4), pp.134-141.
- [106] Taylor, R.P., 1989. Surface roughness measurements on gas turbine blades. Volume 1: Turbomachinery. doi:10.1115/89-gt-285.
- [107] Triantaphyllou, A., Giusca, C.L., Macaulay, G.D., Roerig, F., Hoebel, M., Leach, R.K., Tomita, B. and Milne, K.A., 2015. Surface texture measurement for additive manufacturing. *Surface Topography: Metrology and Properties*, 3(2), p.024002.
- [108] Thompson, A. Surface texture measurement of metal additively manufactured parts by X-ray computed tomography. Thesis submitted to the University of Nottingham for the degree of Doctor of Philosophy, 2018, 292 p.

APPENDIX 1. R_a: measured surface roughness results (mean ± standard deviation, µm)*

Angle (°)	Downskin				Upskin			
	Set A	Set B	Set C	Set D	Set A	Set B	Set C	Set D
25	43±6.7	34±3	41±8.3	37±6.1	36±6.5	20±1.5 ^A	23±1.5 ^A	28±8.7 ^B
30	43±4.7	31±3.9 ^A	32±5.6	48±4.8 ^{B C}	33±11.6	18±3.9	27±3.5 ^B	28±6 ^B
35	42±6	30±4.3 ^A	31±4.2	40±5.3 ^{B C}	27±7.7	23±2.2	31±0.6 ^B	30±5.9 ^B
40	33±4.4	29±3.1	23±5.1 ^A	29±2.2 ^C	25±6.8	29±6	31±6.1	33±4.3 ^A
45	28±4.5	23±4	27±1.7	34±3.6 ^{A B C}	20±5.3	28±5.1	31±7.4	34±5.5 ^A
50	31±4.5	25±4.1 ^A	21±3.4 ^A	32±6.5 ^{B C}	22±3.5	36±7.3 ^A	28±2.8 ^{A B}	27±2.3 ^{A B}
55	31±6	26±2.3	19±2.4 ^{A B}	34±5.9 ^{B C}	26±3.5	28±10.1	30±1.3	36±2.8 ^{A C}
60	24±3.3	20±1.8 ^A	17±2.2 ^A	30±5 ^{B C}	26±4	33±2.5 ^A	30±8.3	39±6.6 ^A
65	32±3.8	21±1.7 ^A	20±6.5 ^A	27±4.8 ^B	25±4	29±2.1	28±4.4	33±0.5 ^{A B}
70	29±3.9	22±2.9 ^A	20±4.4 ^A	34±5.6 ^{B C}	29±4.9	25±2.9	27±4.2	34±8.1
75	28±3.4	20±1.9 ^A	25±4.8	29±4 ^B	31±2.3	30±4.9	29±5	30±1.6
80	26±1.8	19±3.1 ^A	22±7.4	28±1.2 ^B	31±5.9	28±3.6	25±4.1 ^A	30±1.5
85	26±4.9	20±2.7	22±5.8	31±11.3	31±2.3	26±4.6	22±3.9 ^A	33±5.2 ^C
90	27±4.5	19±3.7 ^A	25±2.9	28±8 ^B	25±3.5	29±4.2	24±3.7 ^B	30±3.7

* statistically significant difference (p<0.05), t-test for corresponding groups (A, B, C)

APPENDIX 2. Rq: measured surface roughness results (mean \pm standard deviation, μm) *

Angle (°)	Downskin				Upskin			
	A	B	C	D	A	B	C	D
25	53 \pm 9.5	40 \pm 2.2	50 \pm 10.2	45 \pm 5.7	43 \pm 6.7	26 \pm 2.6 ^A	28 \pm 1.9 ^A	36 \pm 11.7
30	51 \pm 5.7	38 \pm 5.7 ^A	39 \pm 6.4	58 \pm 4.7 ^{B C}	40 \pm 14.6	24 \pm 4.2	33 \pm 4.4 ^B	34 \pm 7.1 ^B
35	49 \pm 4.4	37 \pm 4.9 ^A	38 \pm 4.9 ^A	48 \pm 5.8 ^{B C}	35 \pm 10.5	28 \pm 2.4	38 \pm 0.9 ^B	38 \pm 8 ^B
40	40 \pm 5.1	36 \pm 3.6	29 \pm 5.4 ^A	35 \pm 2.8 ^C	30 \pm 8.4	35 \pm 5.6	38 \pm 6.8	40 \pm 5 ^A
45	36 \pm 5.5	30 \pm 6	32 \pm 2.5	42 \pm 5.6 ^{B C}	25 \pm 5.1	34 \pm 5.4	38 \pm 9.1	42 \pm 7.2 ^A
50	39 \pm 5.7	31 \pm 5.6 ^A	26 \pm 3.4 ^A	39 \pm 7.3 ^C	28 \pm 3.6	44 \pm 8.8 ^A	35 \pm 3.5 ^{A B}	33 \pm 3 ^B
55	37 \pm 5.7	33 \pm 2.8	24 \pm 2.8 ^{A B}	42 \pm 5.6 ^{B C}	32 \pm 4.6	34 \pm 11.5	36 \pm 1.3	43 \pm 3.1 ^{A C}
60	30 \pm 3.4	25 \pm 2.4 ^A	21 \pm 2.4 ^A	36 \pm 5.8 ^{B C}	33 \pm 5	41 \pm 2.5 ^A	36 \pm 10.9	47 \pm 6.9 ^A
65	40 \pm 5.4	26 \pm 1.9 ^A	26 \pm 9.9 ^A	33 \pm 4.9 ^B	32 \pm 6.3	36 \pm 3.3	35 \pm 5.3	40 \pm 1.3
70	36 \pm 4	28 \pm 3.3 ^A	25 \pm 4.8 ^A	41 \pm 7.4 ^{B C}	36 \pm 6.3	33 \pm 2.8	33 \pm 4.7	42 \pm 10.3
75	34 \pm 4.4	24 \pm 2 ^A	31 \pm 6.2	35 \pm 4.3 ^B	39 \pm 1.6	38 \pm 5.7	35 \pm 5.2	37 \pm 2.3
80	33 \pm 2	24 \pm 4 ^A	25 \pm 6	35 \pm 1.2 ^{B C}	38 \pm 6.3	35 \pm 4.9	30 \pm 4.3 ^A	37 \pm 2.4 ^C
85	32 \pm 5.6	25 \pm 2.7	27 \pm 6.4	38 \pm 12.1	37 \pm 2.8	32 \pm 5.5	30 \pm 2 ^A	41 \pm 5.5 ^{B C}
90	34 \pm 5	24 \pm 4.7 ^A	31 \pm 3.5	35 \pm 10.8	32 \pm 3.4	37 \pm 5.3	30 \pm 4.6 ^B	35 \pm 10.8

* statistically significant difference ($p < 0.05$), t-test for corresponded group (A, B, C)

APPENDIX 3. Rz: measured surface roughness results (mean \pm standard deviation, μm)*

Angle (°)	Downskin				Upskin			
	A	B	C	D	A	B	C	D
25	243 \pm 43.1	168 \pm 7.5 ^A	228 \pm 45.4	199 \pm 13.8 ^{A B}	173 \pm 23.4	119 \pm 17 ^A	138 \pm 12.9 ^A	168 \pm 46.7
30	214 \pm 9.5	172 \pm 28.7 ^A	189 \pm 18.6	240 \pm 29.8 ^{B C}	175 \pm 70.4	125 \pm 12.7	150 \pm 23.5	161 \pm 26.7
35	201 \pm 15.5	152 \pm 17.6 ^A	168 \pm 24.1	220 \pm 39.2 ^B	168 \pm 50.9	126 \pm 14.2	170 \pm 21.4 ^B	180 \pm 45 ^B
40	182 \pm 24.2	164 \pm 19.4	141 \pm 16.2 ^A	165 \pm 18.2	130 \pm 34.1	160 \pm 14.7	175 \pm 26.8 ^A	179 \pm 26.4 ^A
45	179 \pm 27.3	150 \pm 34.6	150 \pm 21.4	192 \pm 43	116 \pm 6.7	154 \pm 12.6 ^A	170 \pm 39.9	180 \pm 28.7 ^A
50	189 \pm 30.3	148 \pm 28.7 ^A	134 \pm 11.9 ^A	179 \pm 22.9 ^C	133 \pm 11.7	191 \pm 32.8 ^A	162 \pm 20.3	165 \pm 13.6 ^A
55	174 \pm 23.6	171 \pm 20	113 \pm 16.9 ^{A B}	182 \pm 14.2 ^C	130 \pm 12.9	156 \pm 43.3	154 \pm 3 ^A	182 \pm 22.2 ^A
60	157 \pm 14.8	122 \pm 15.5 ^A	110 \pm 17.4 ^A	166 \pm 20.2 ^{B C}	156 \pm 25.6	186 \pm 10.1	164 \pm 53.6	197 \pm 16.3 ^A
65	194 \pm 32	136 \pm 16.5 ^A	132 \pm 52.5 ^A	152 \pm 13.7	162 \pm 29.6	164 \pm 10.5	173 \pm 27.1	173 \pm 11.9
70	177 \pm 17.4	136 \pm 14.2 ^A	119 \pm 18.7 ^A	197 \pm 45.1 ^{B C}	173 \pm 33.7	164 \pm 14.8	152 \pm 29.7	207 \pm 53.9
75	165 \pm 16.3	118 \pm 4.6 ^A	148 \pm 30.1	150 \pm 14.6 ^B	185 \pm 26.1	185 \pm 35.9	160 \pm 26.3	173 \pm 12.4
80	170 \pm 18.6	119 \pm 24.6 ^A	120 \pm 29.1 ^A	170 \pm 4 ^{B C}	174 \pm 27.2	168 \pm 32.5	148 \pm 15.8	169 \pm 13.7
85	150 \pm 25.4	113 \pm 8.8 ^A	125 \pm 24	175 \pm 41 ^C	161 \pm 22.9	146 \pm 23	127 \pm 26.9 ^A	196 \pm 22.6 ^{B C}
90	166 \pm 14.4	125 \pm 31.8	151 \pm 9.7	181 \pm 23.3 ^B	152 \pm 24.3	177 \pm 23.3	159 \pm 21.9	160 \pm 52.2

* statistically significant difference ($p < 0.05$), t-test for corresponded group (A, B, C)

APPENDIX 4. Predicted values of the roughness

Angle (°)	Layer thickness (μm)	Equation 4 – Ra (μm)	Equation 5 – h (μm)
25	50	11.33	118.366
30	50	10.827	100.046
35	50	10.242	87.211
40	50	9.578	77.819
45	50	8.842	70.739
50	50	8.039	65.295
55	50	7.175	61.059
60	50	6.256	57.753
65	50	5.289	55.184
70	50	4.283	53.221
75	50	3.243	51.773
80	50	2.179	50.778
85	50	1.099	50.194
90	50	0.009	50.000

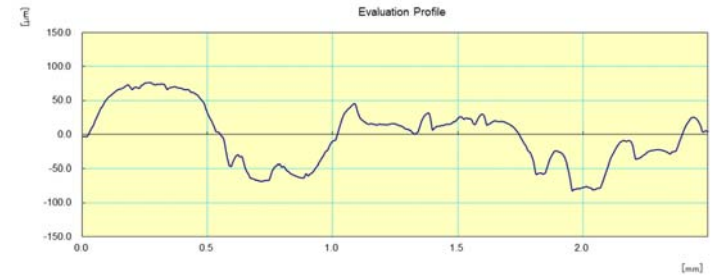
APPENDIX 5. Typical profiles of surface roughness results for Set A

Angle (°)

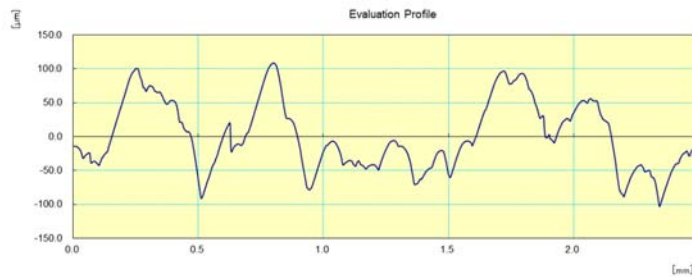
Downskin

Upskin

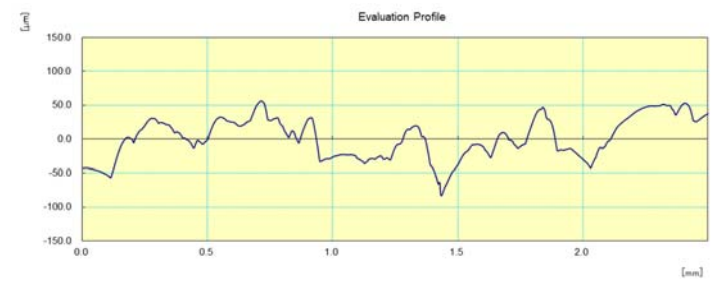
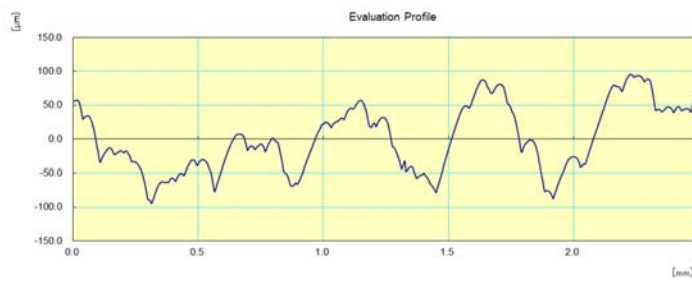
25



30



35



Angle (°)

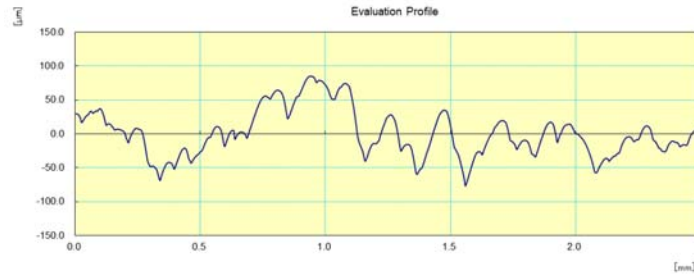
Downskin

Upskin

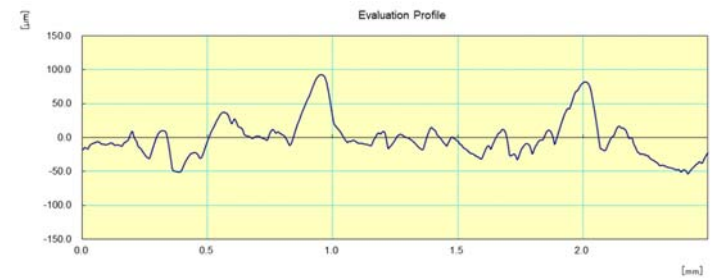
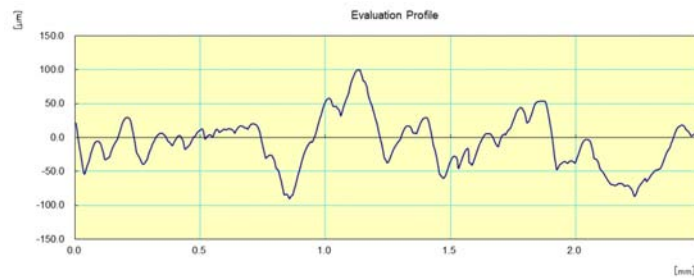
40



45



50

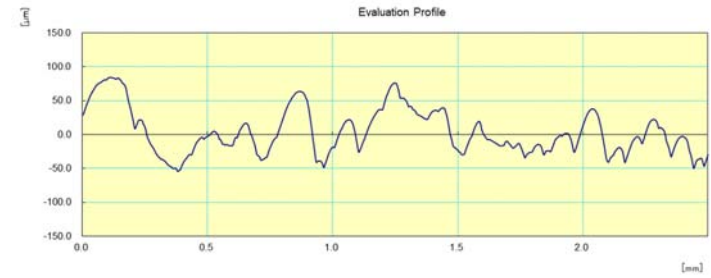


Angle (°)

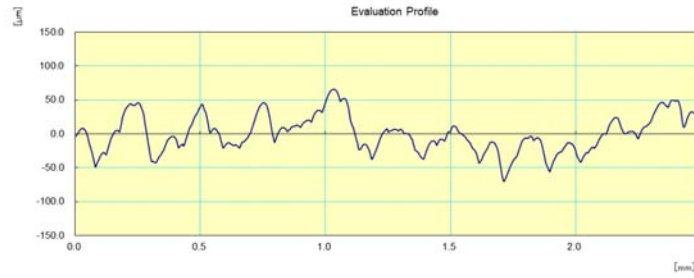
Downskin

Upskin

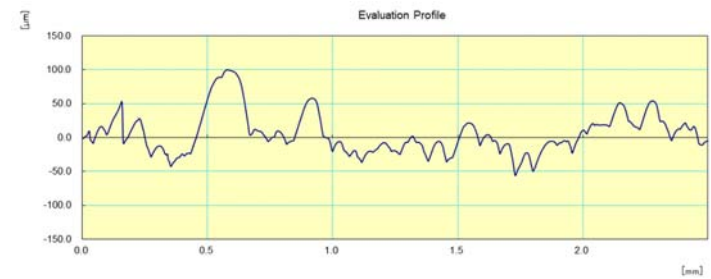
55



60



65

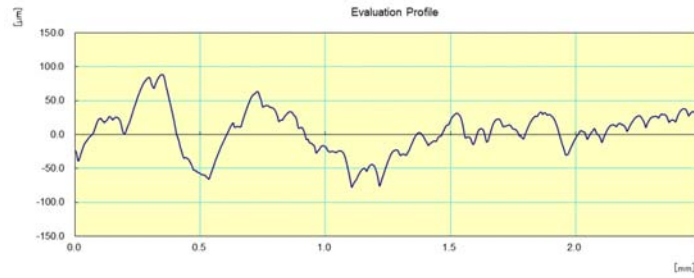


Angle (°)

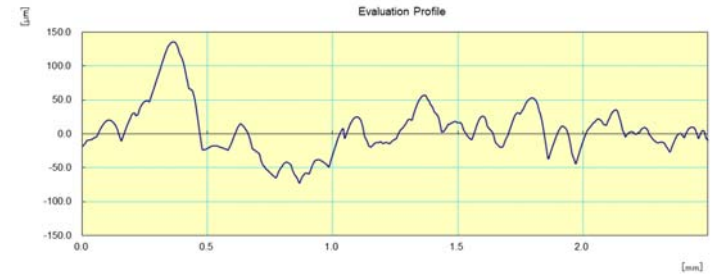
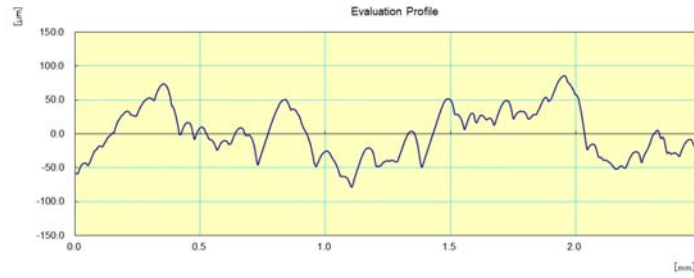
Downskin

Upskin

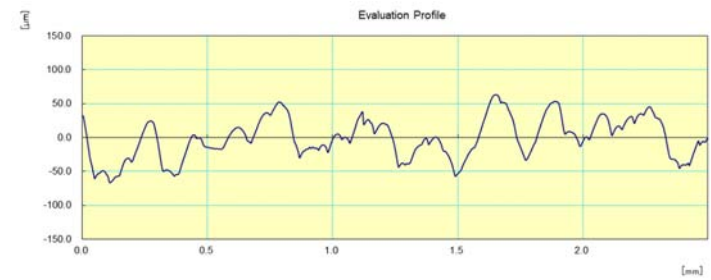
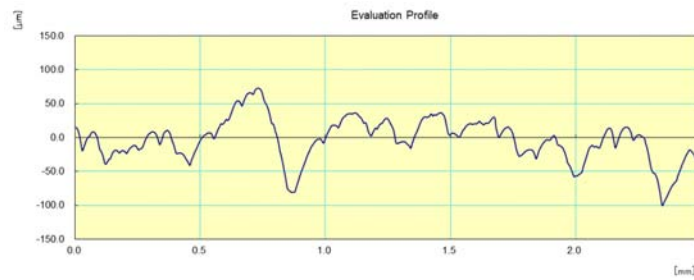
70



75



80



Angle (°)

85

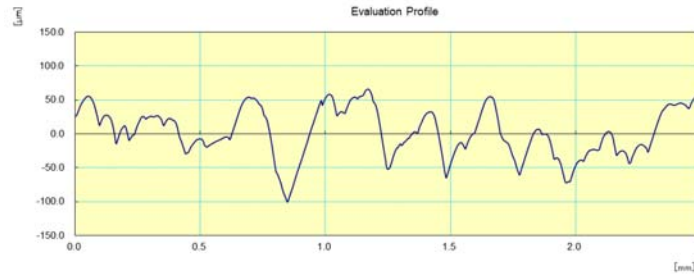
Downskin



Upskin



90



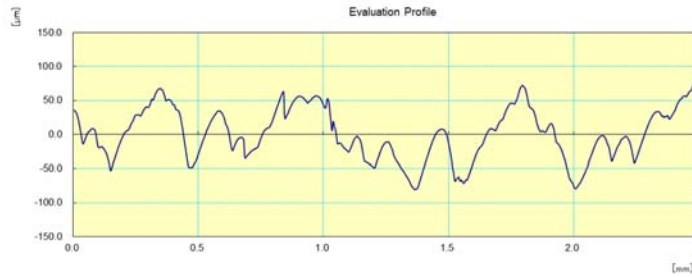
APPENDIX 6. Typical profiles of surface roughness results for Set B

Angle (°)

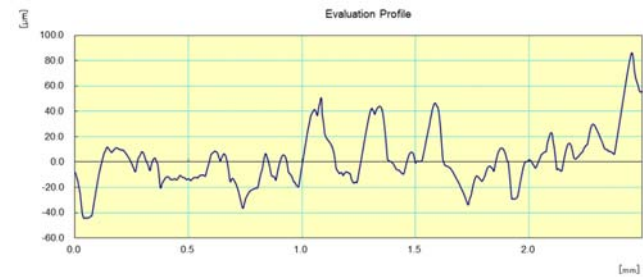
Downskin

Upskin

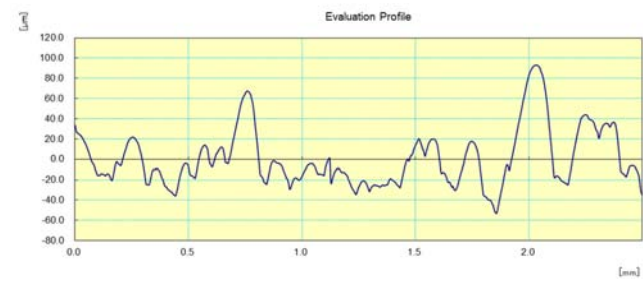
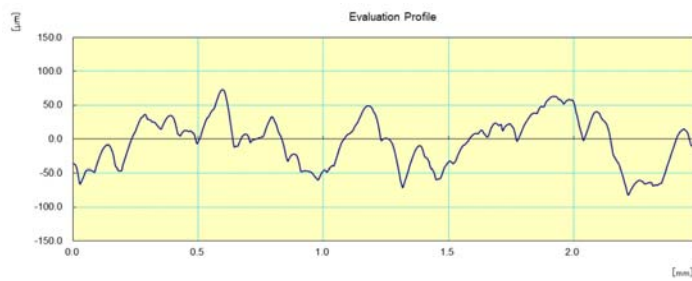
25



30



35

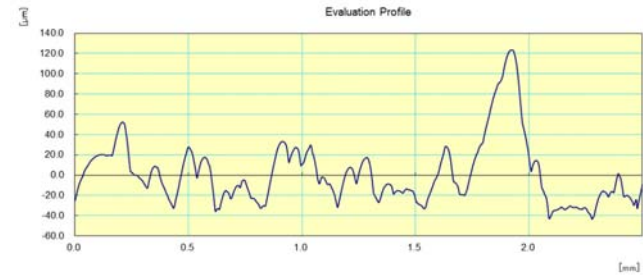


Angle (°)

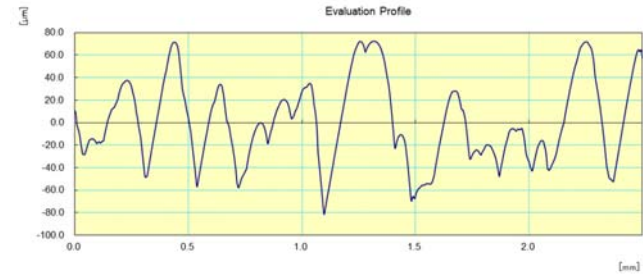
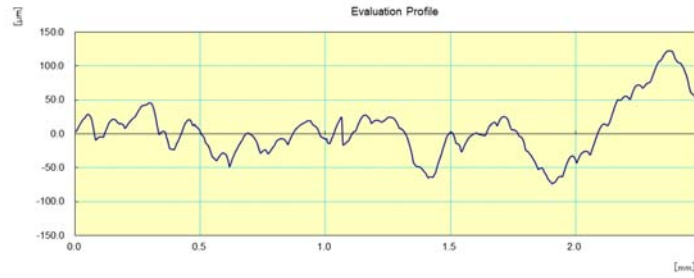
Downskin

Upskin

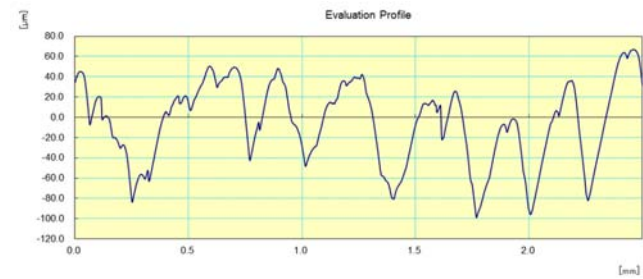
40



45



50

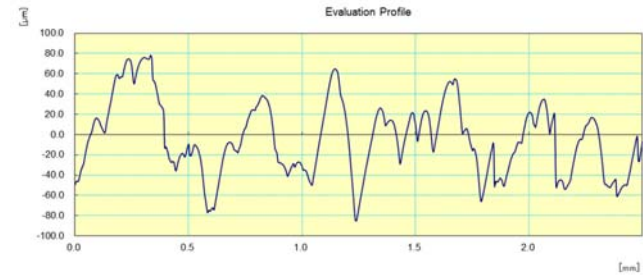
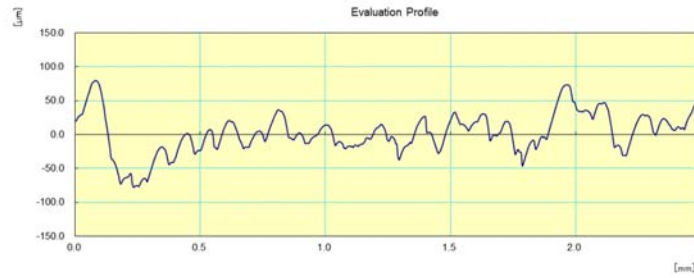


Angle (°)

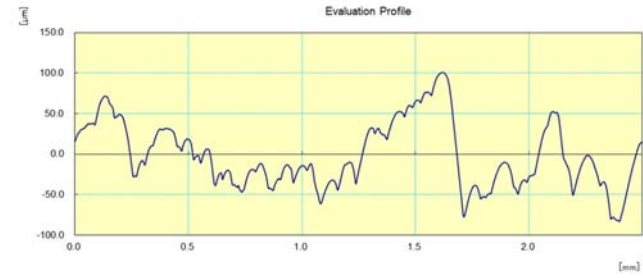
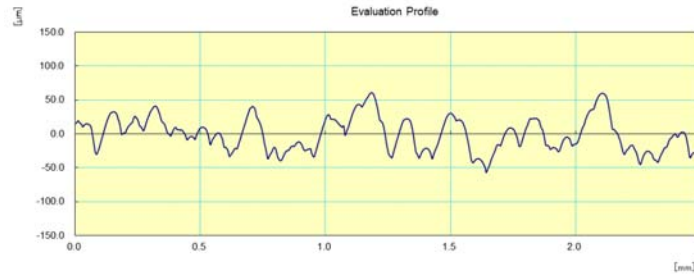
Downskin

Upskin

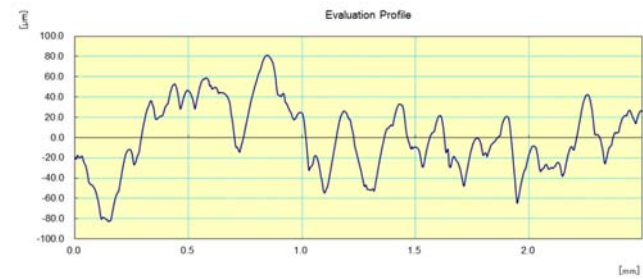
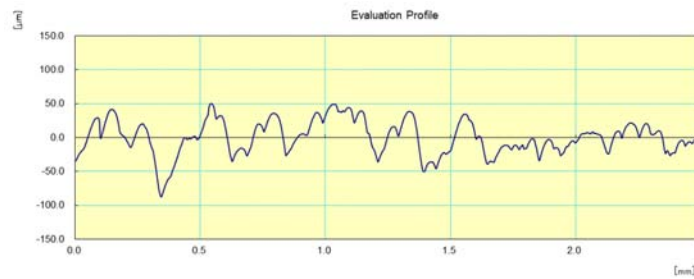
55



60



65

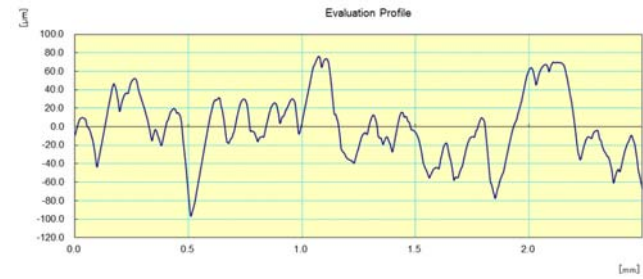


Angle (°)

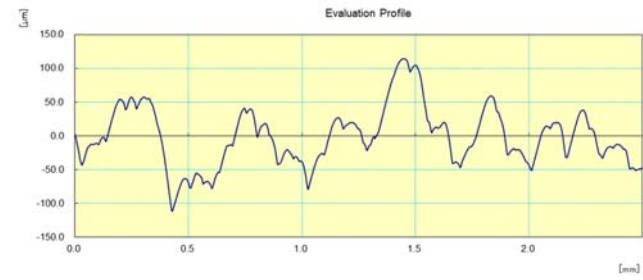
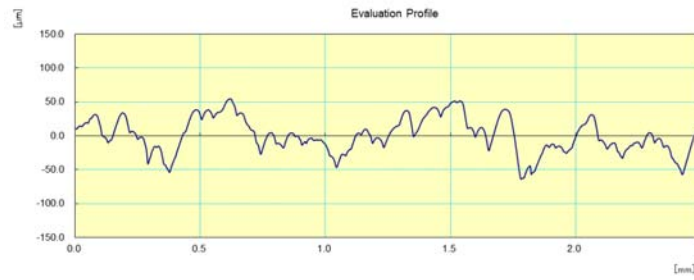
Downskin

Upskin

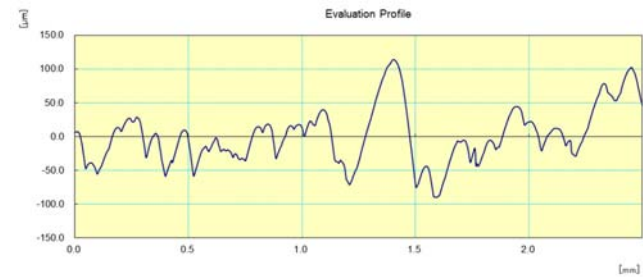
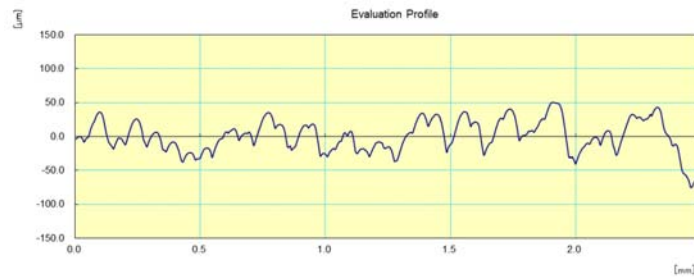
70



75



80

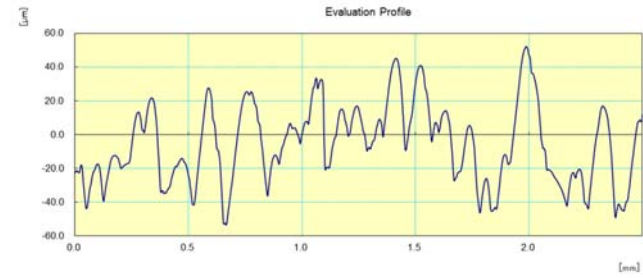


Angle (°)

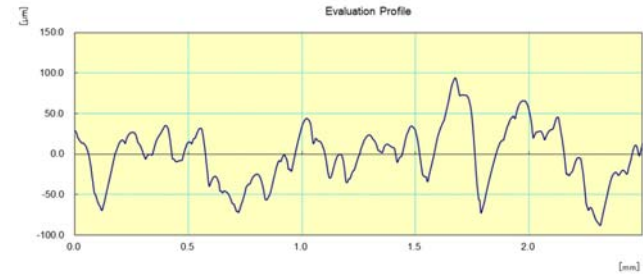
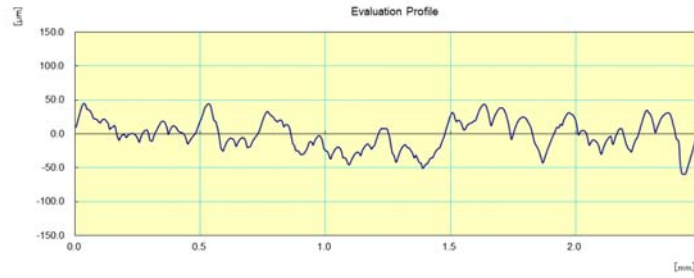
Downskin

Upskin

85



90



APPENDIX 7. Typical profiles of surface roughness results for Set C

Angle (°)

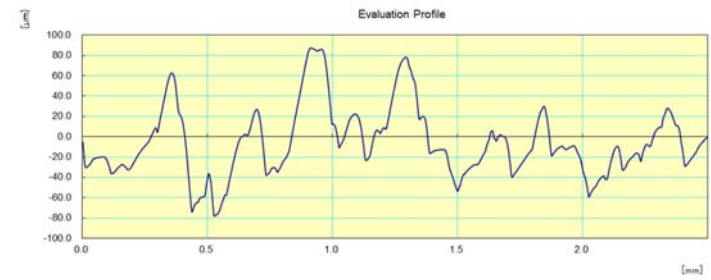
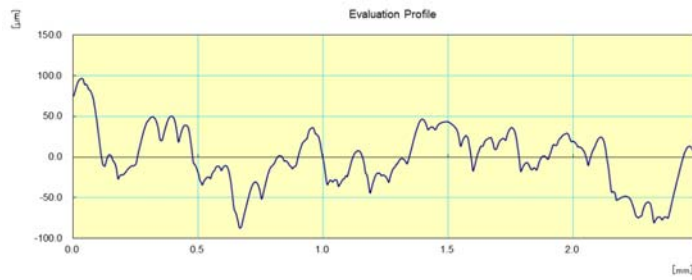
Downskin

Upskin

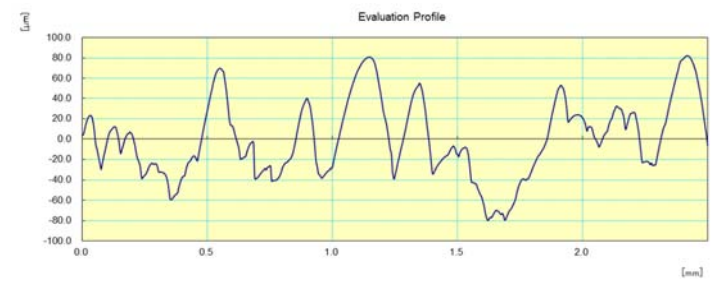
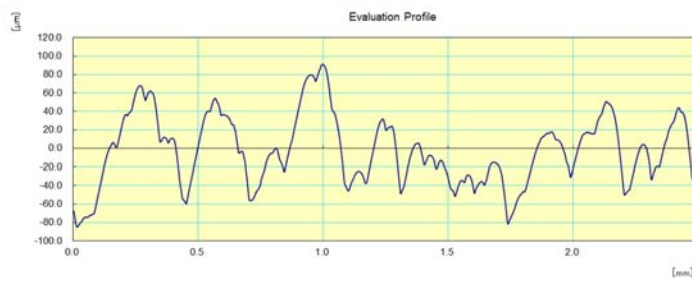
25



30



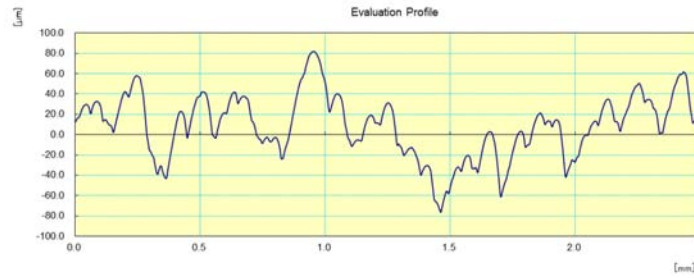
35



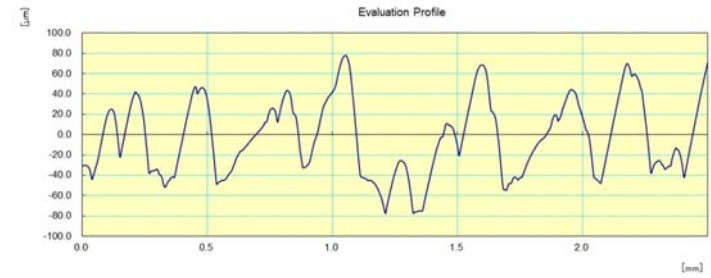
Angle (°)

40

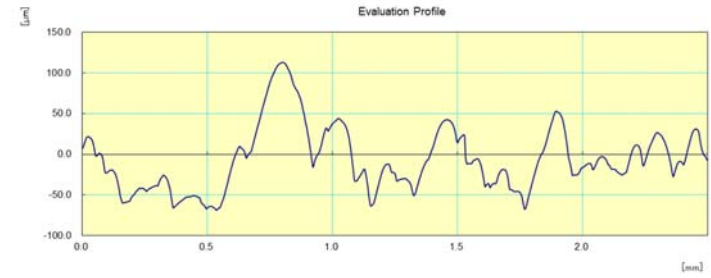
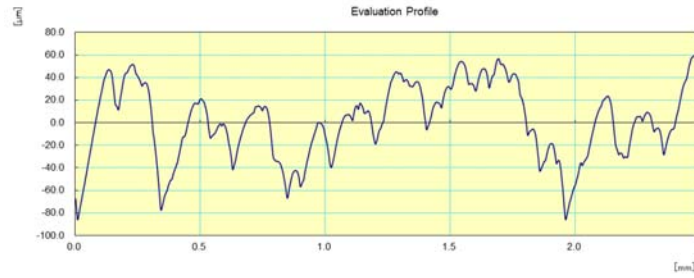
Downskin



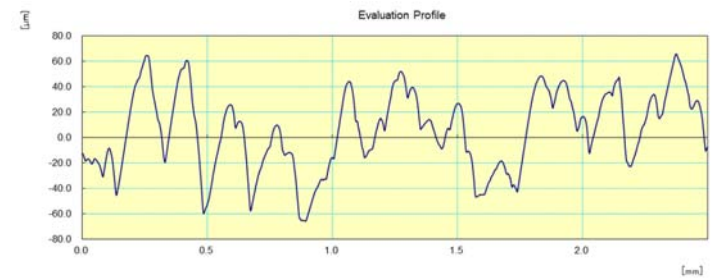
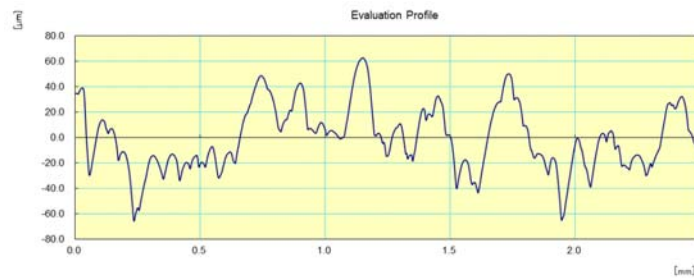
Upskin



45



50



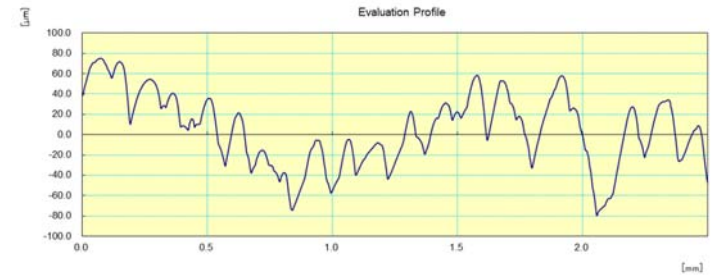
Angle (°)

55

Downskin



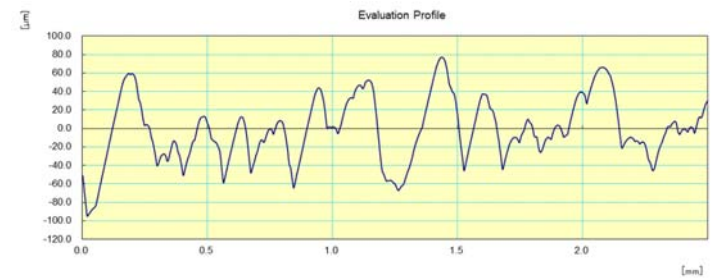
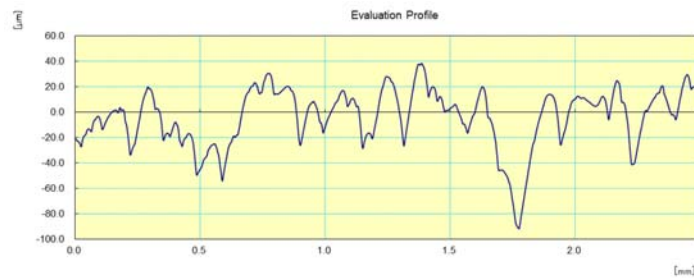
Upskin



60



65



Angle (°)

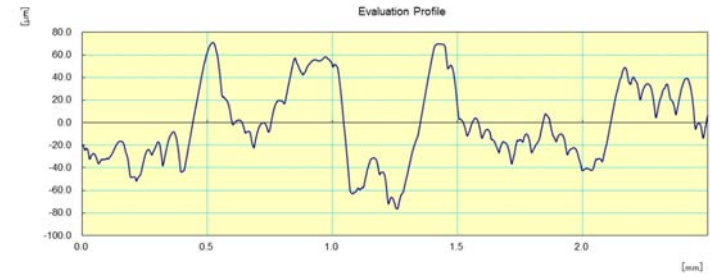
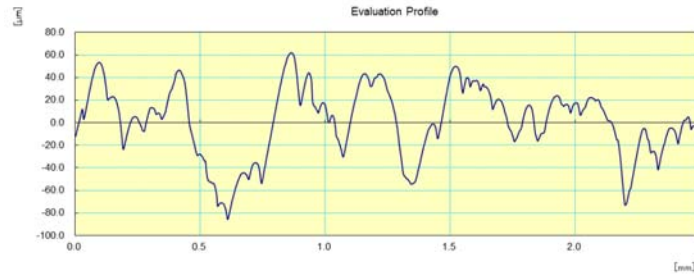
Downskin

Upskin

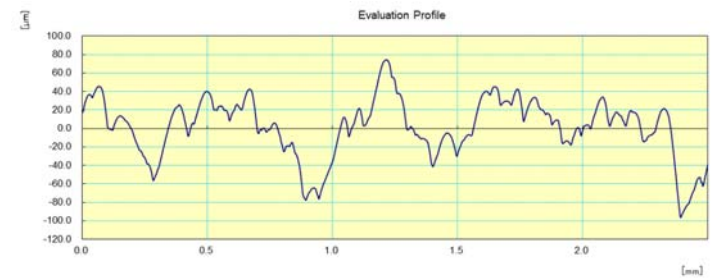
70



75



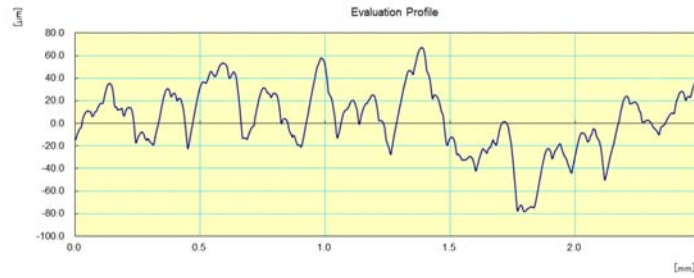
80



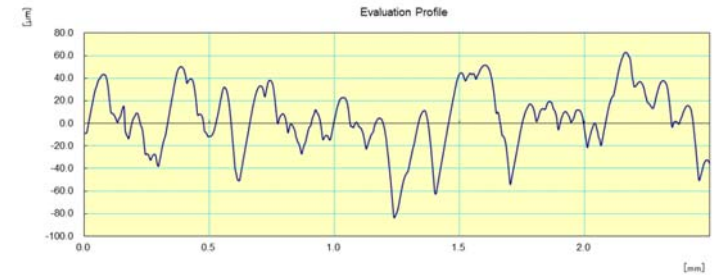
Angle (°)

85

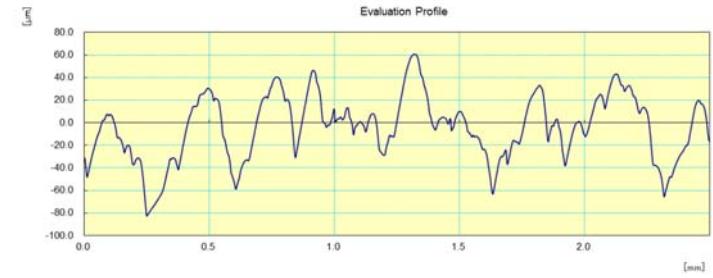
Downskin



Upskin



90



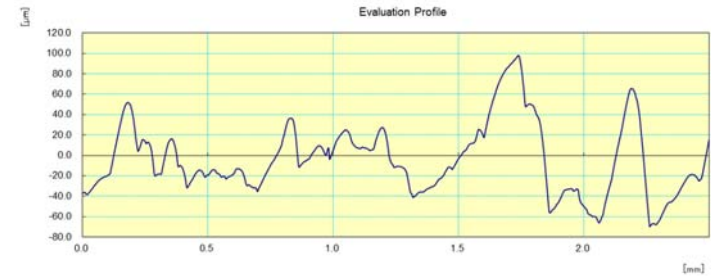
APPENDIX 8. Typical profiles of surface roughness results for Set D

Angle (°)

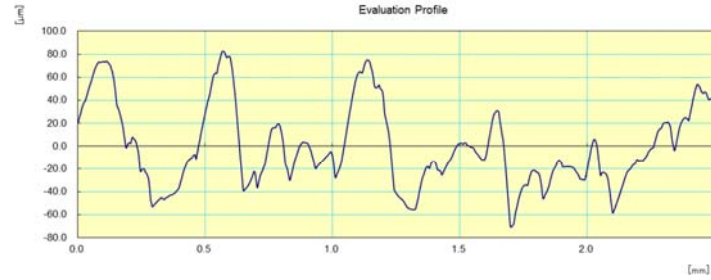
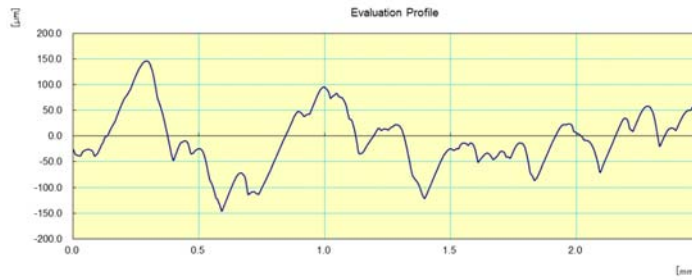
Downskin

Upskin

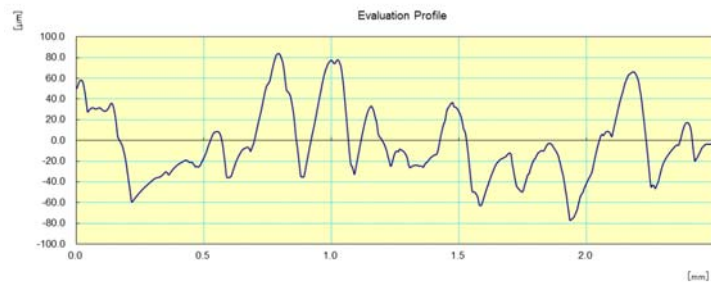
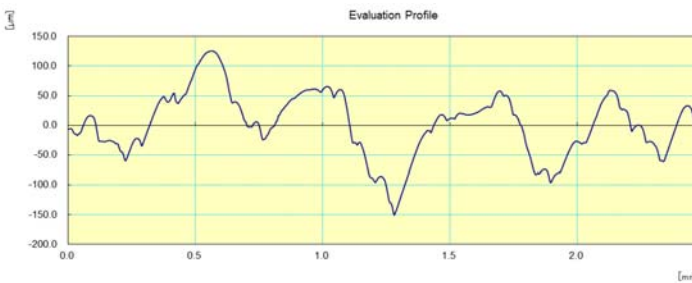
25



30



35

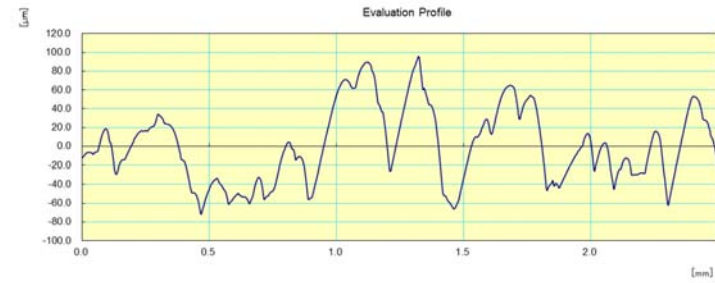
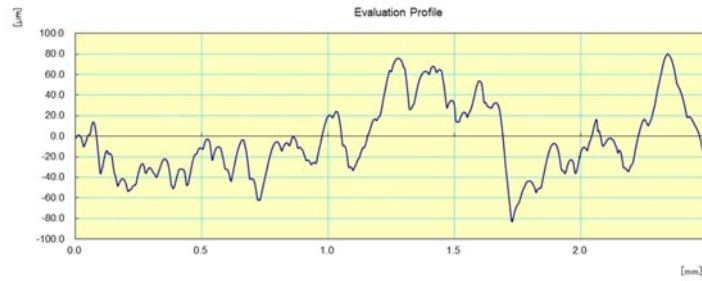


Angle (°)

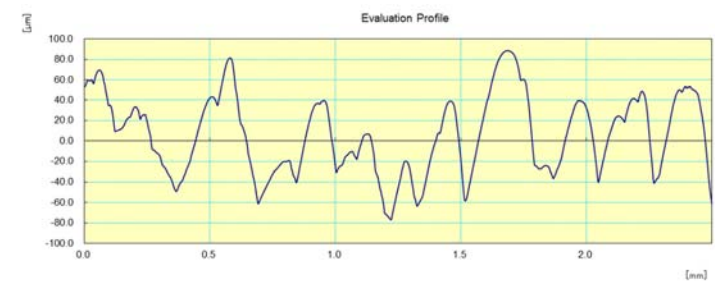
Downskin

Upskin

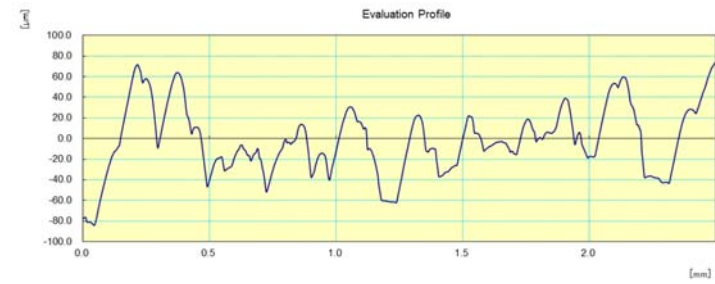
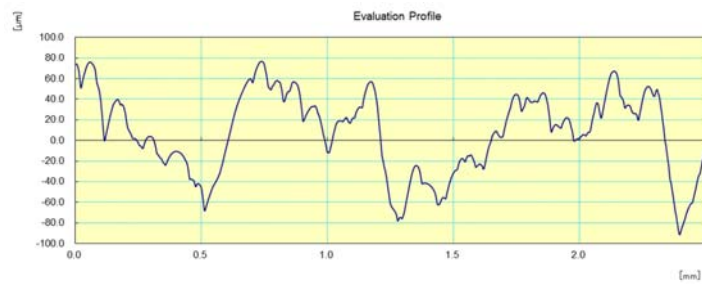
40



45



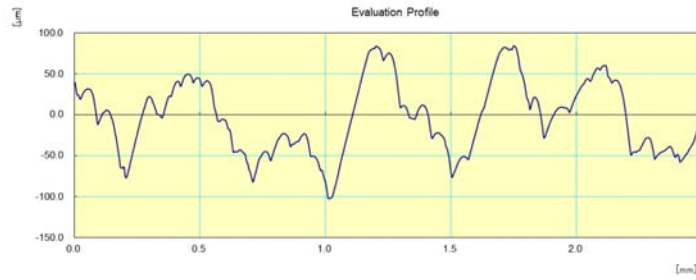
50



Angle (°)

55

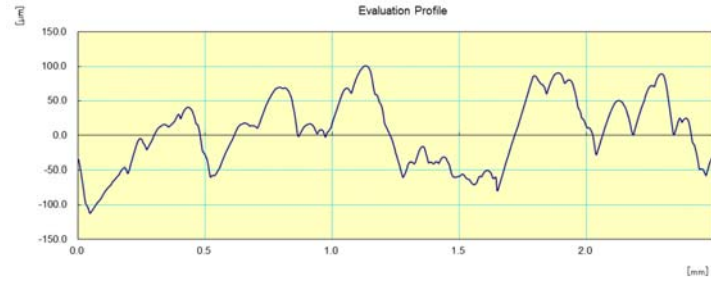
Downskin



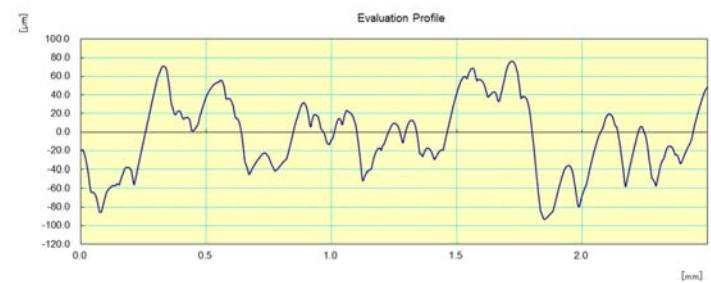
Upskin



60



65

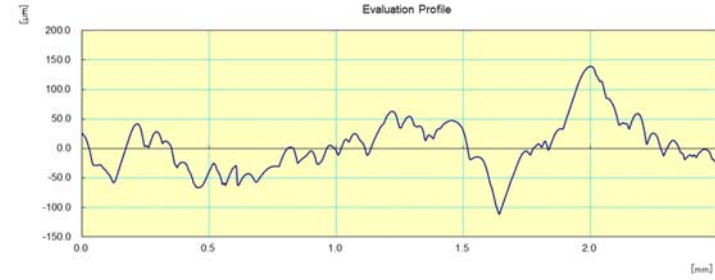
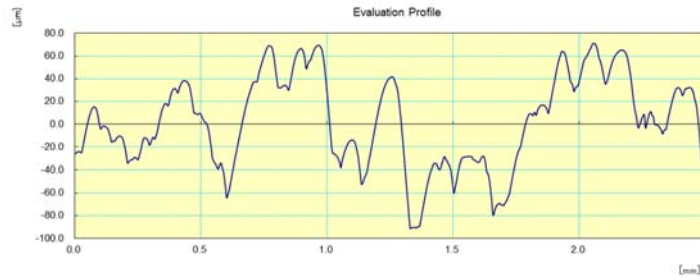


Angle (°)

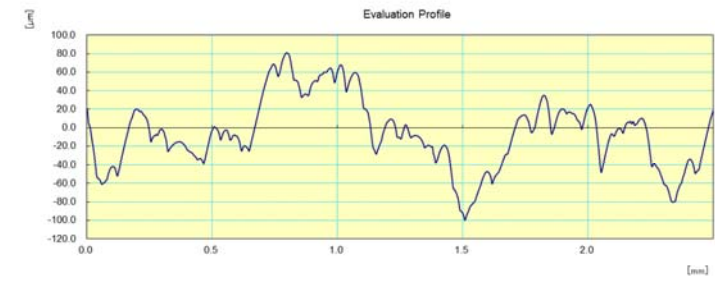
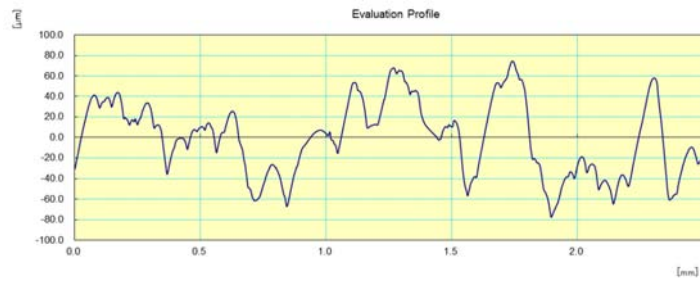
Downskin

Upskin

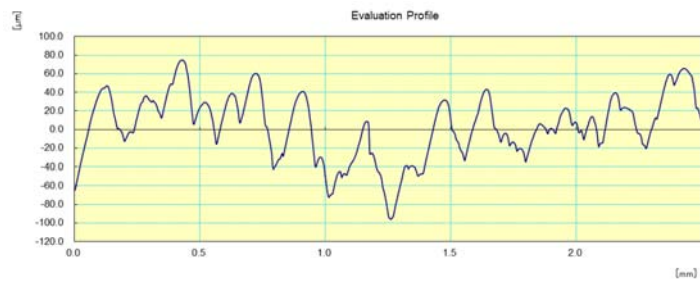
70



75



80

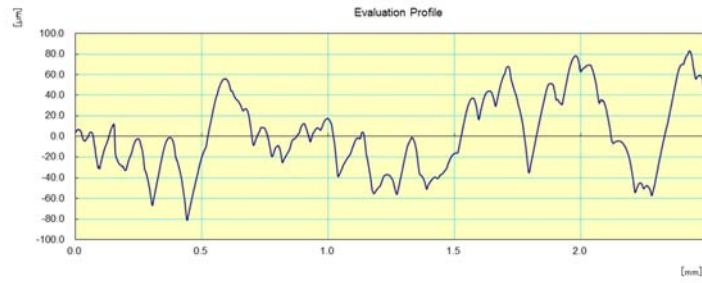


Angle (°)

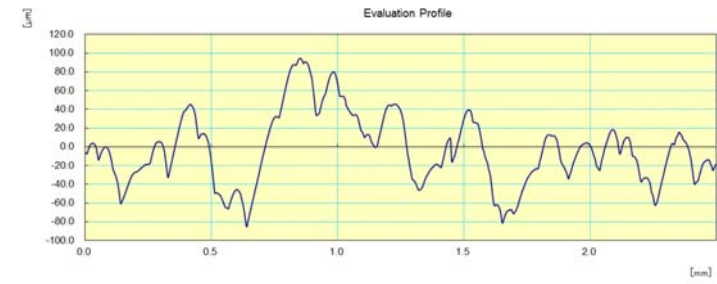
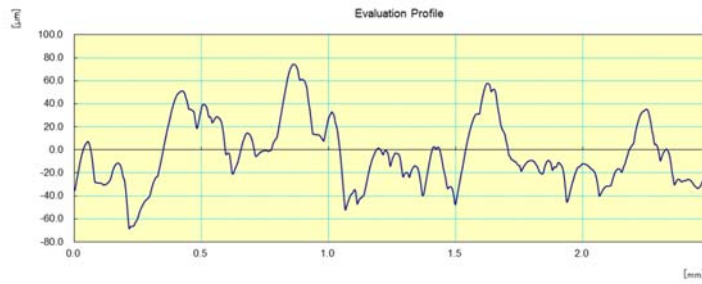
Downskin

Upskin

85



90



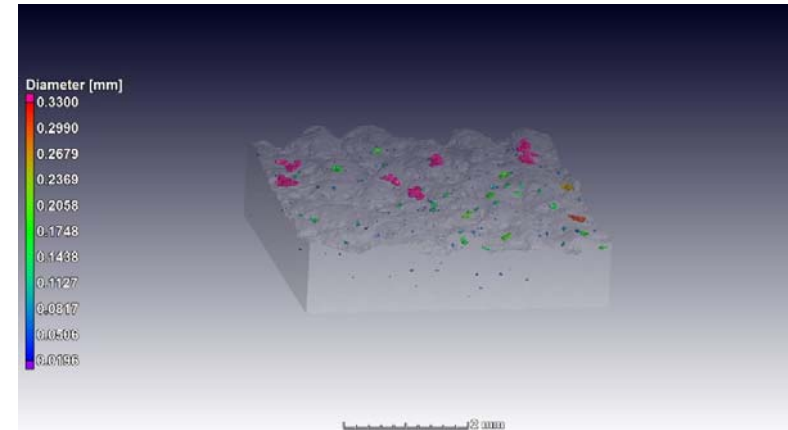
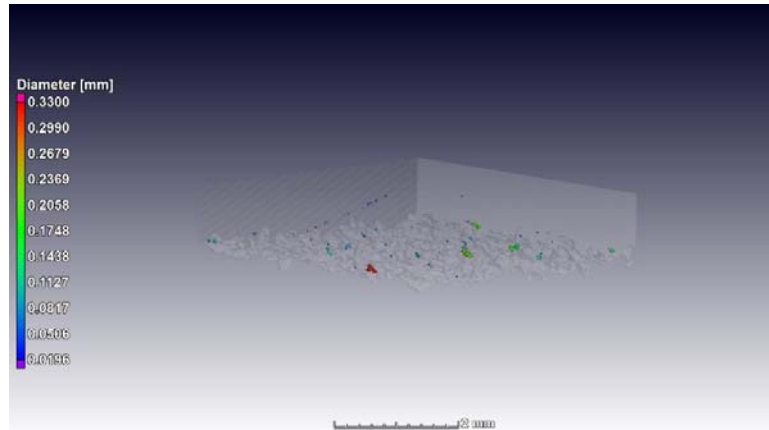
APPENDIX 9. Porosity in areas near downskin and upskin surfaces in sample A

Angle (°)

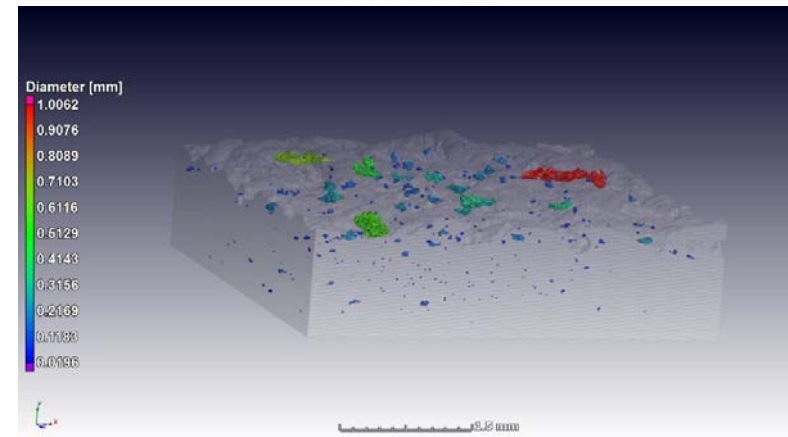
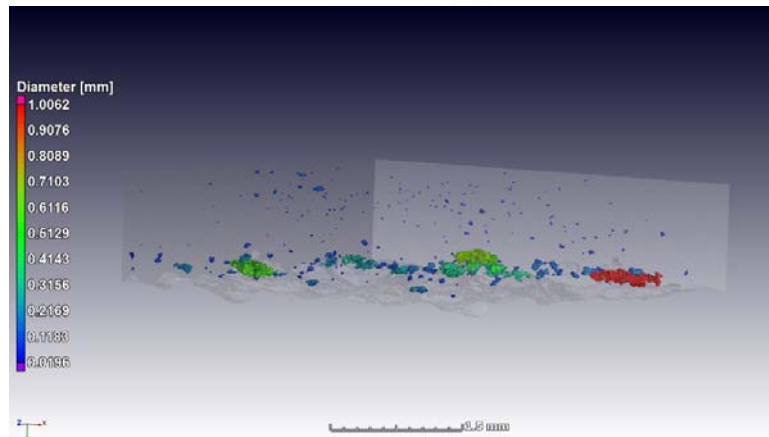
Downskin set A

Upskin set A

25



30

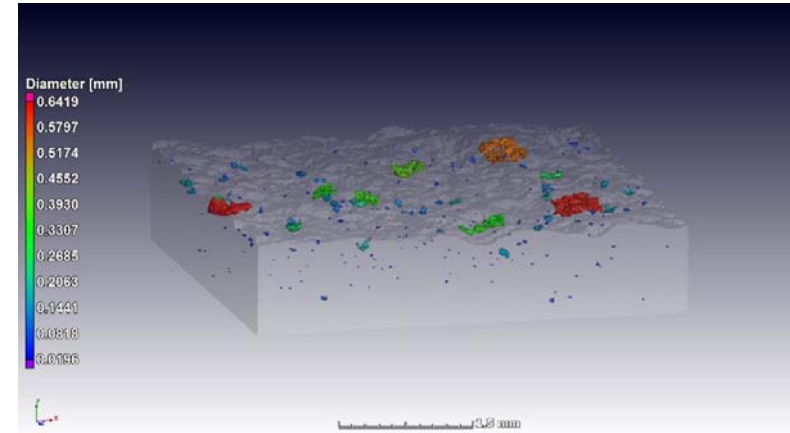
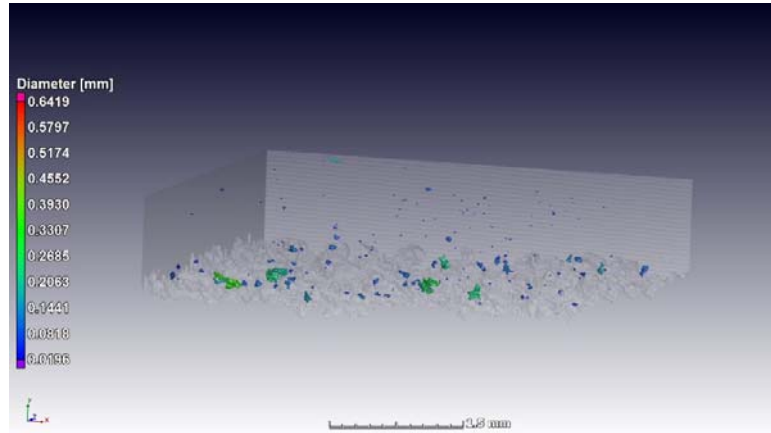


Angle (°)

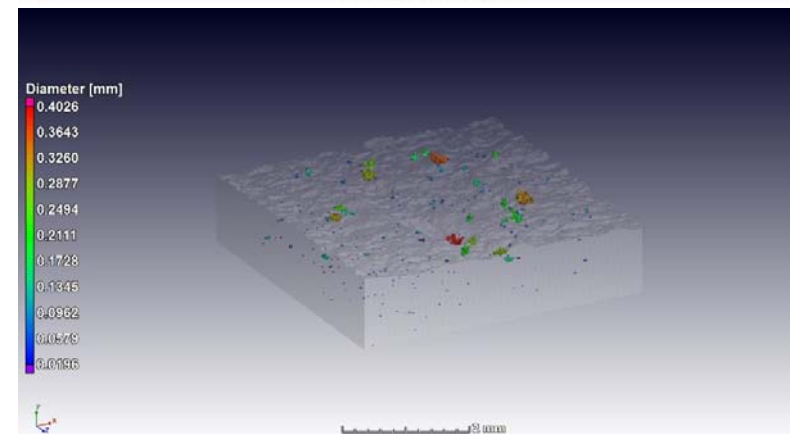
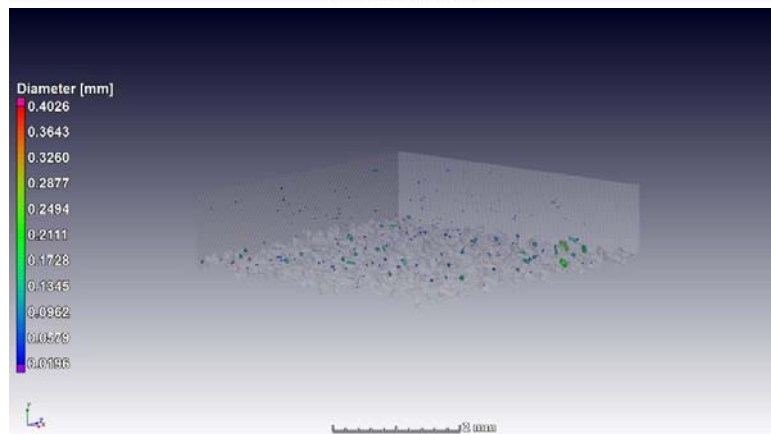
Downskin set A

Upskin set A

35



40

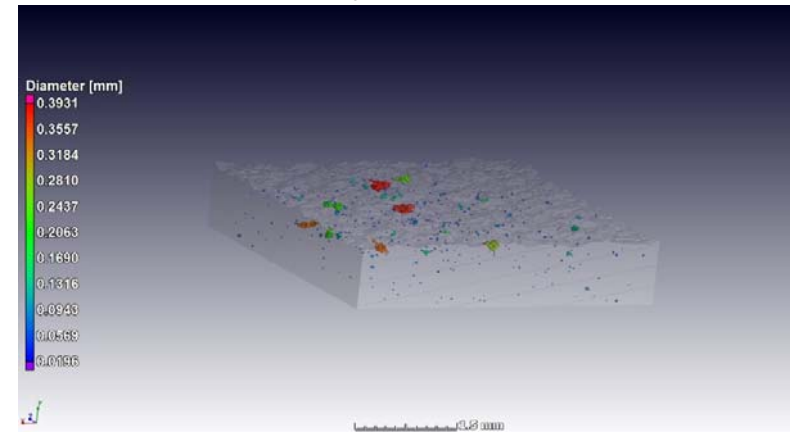
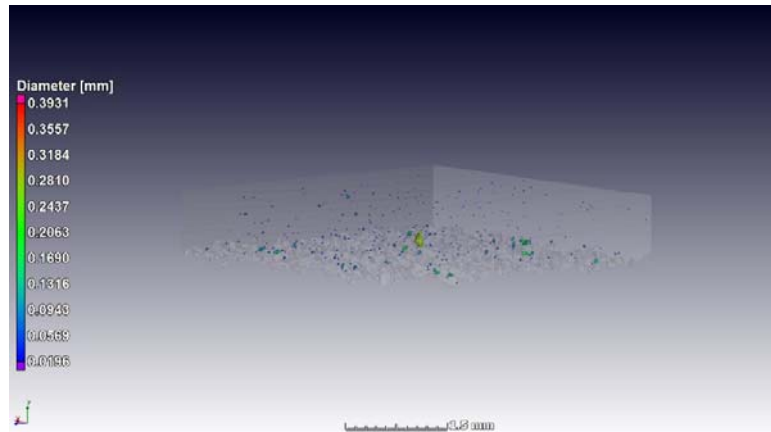


Angle (°)

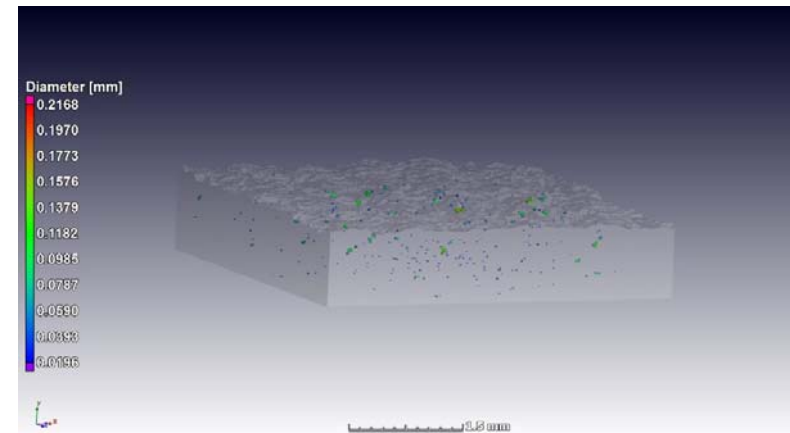
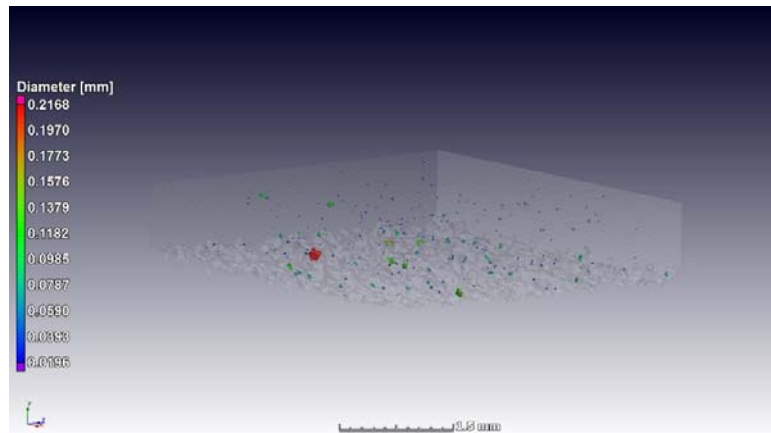
Downskin set A

Upskin set A

45



50

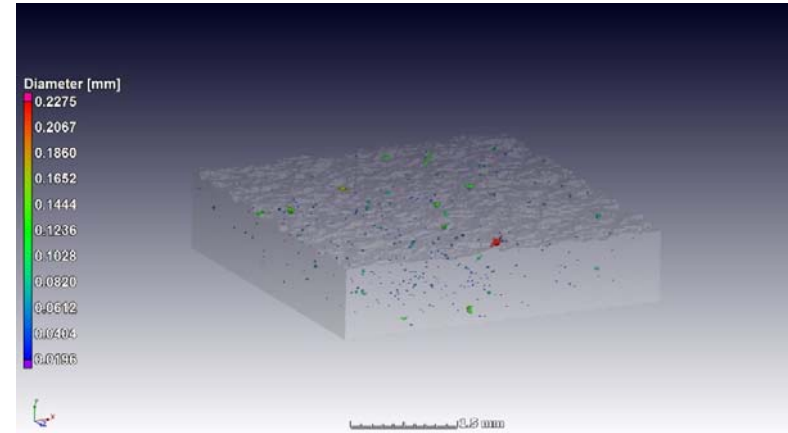
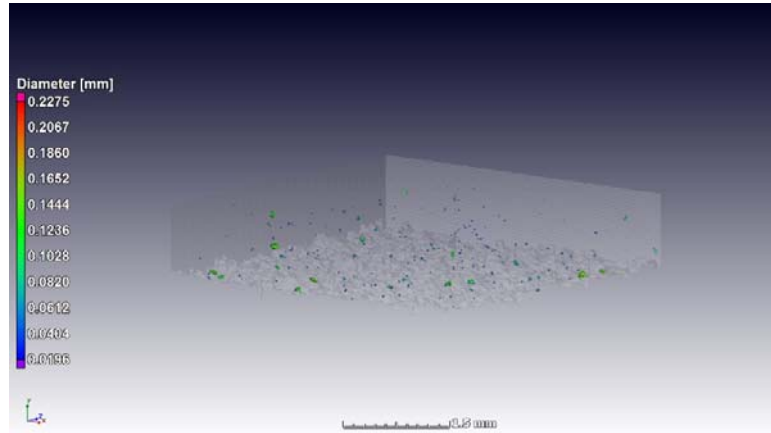


Angle (°)

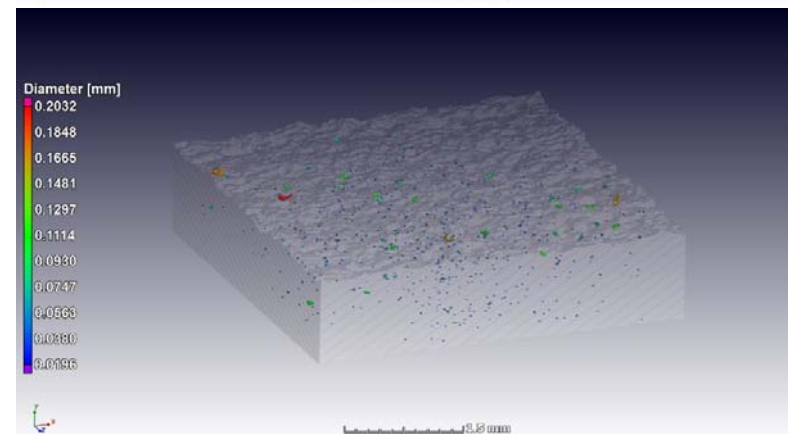
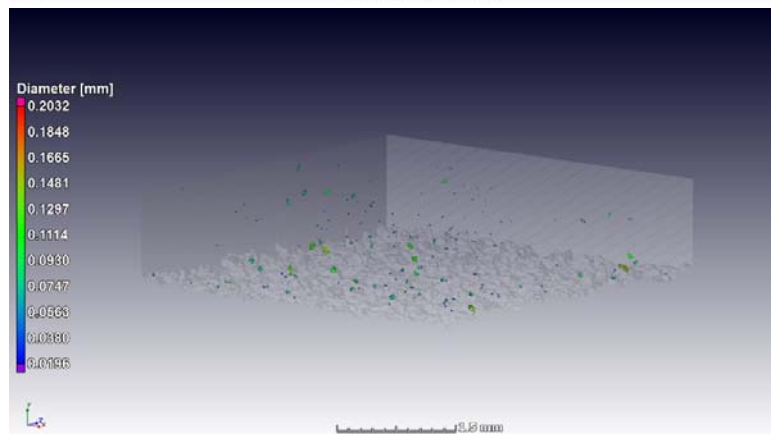
Downskin set A

Upskin set A

55



60

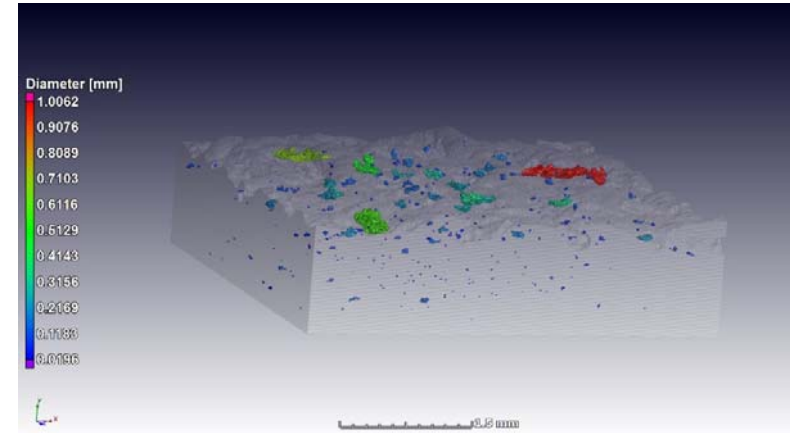
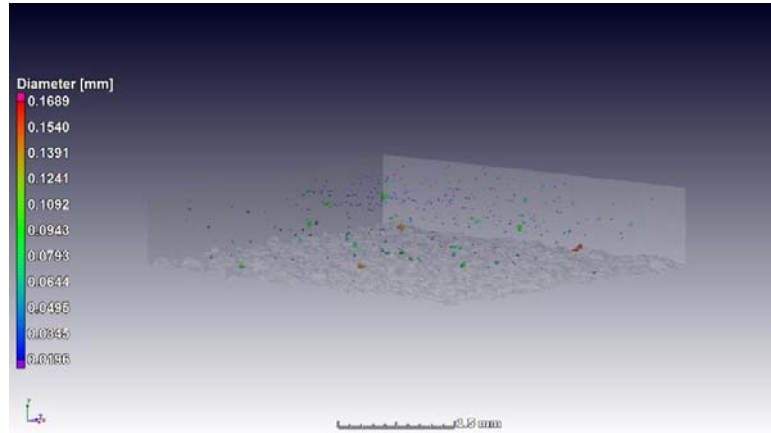


Angle (°)

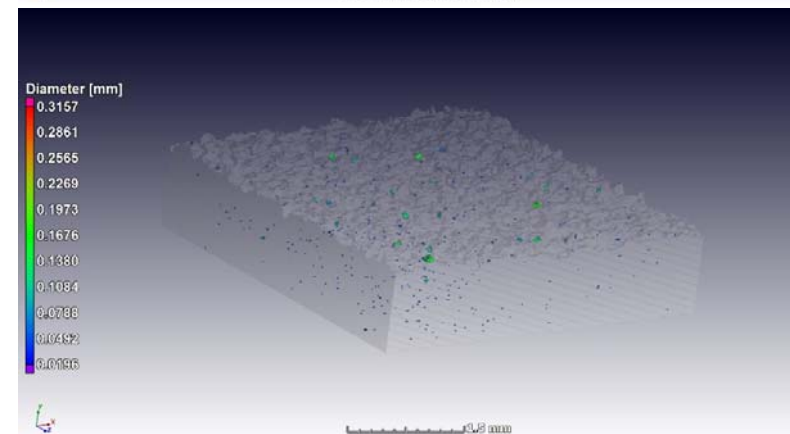
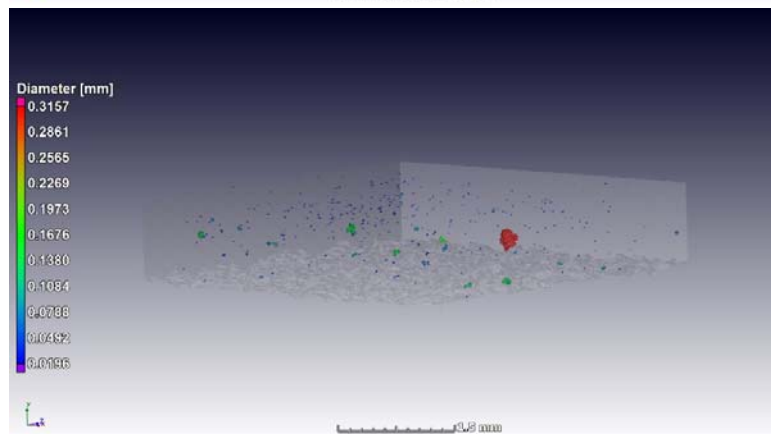
Downskin set A

Upskin set A

65



70

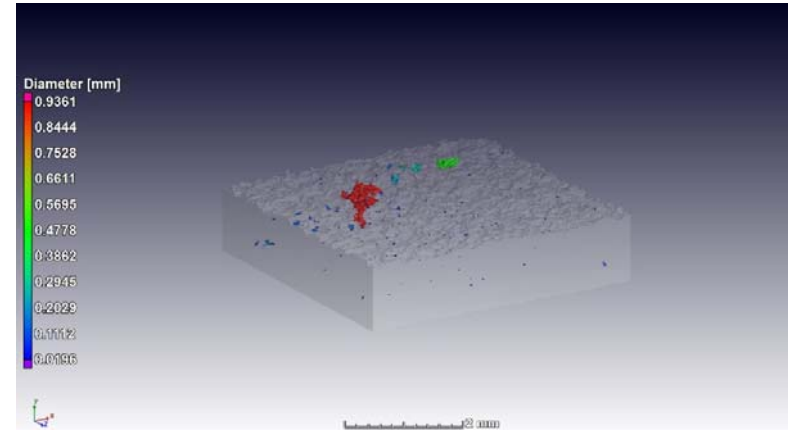
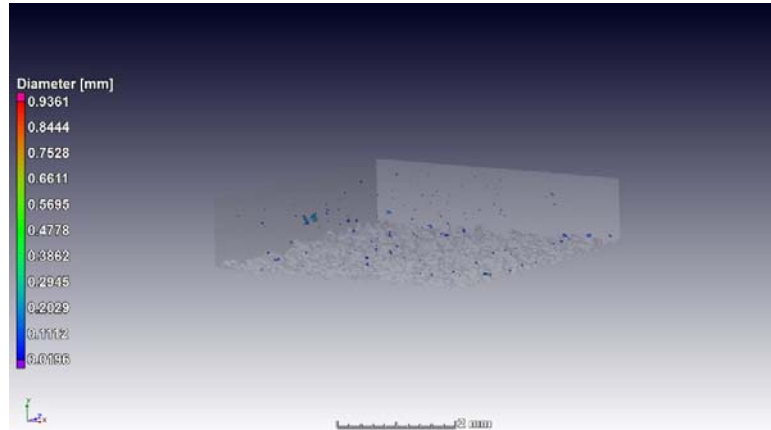


Angle (°)

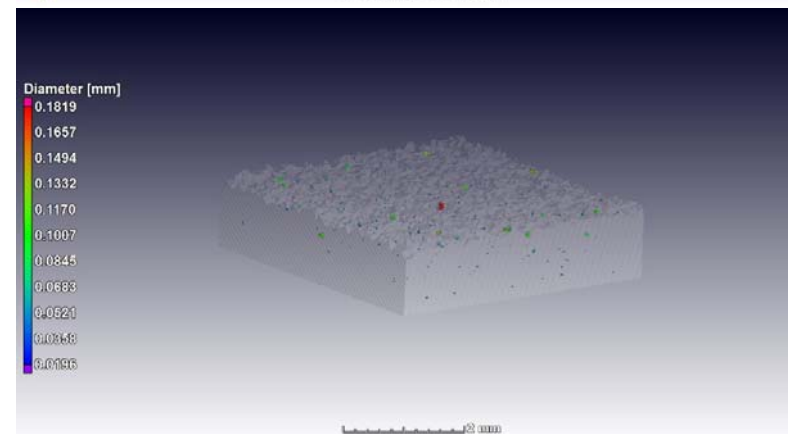
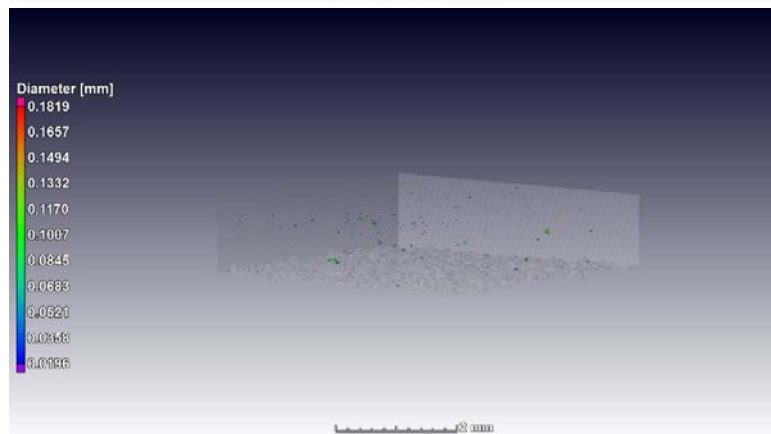
Downskin set A

Upskin set A

75



80

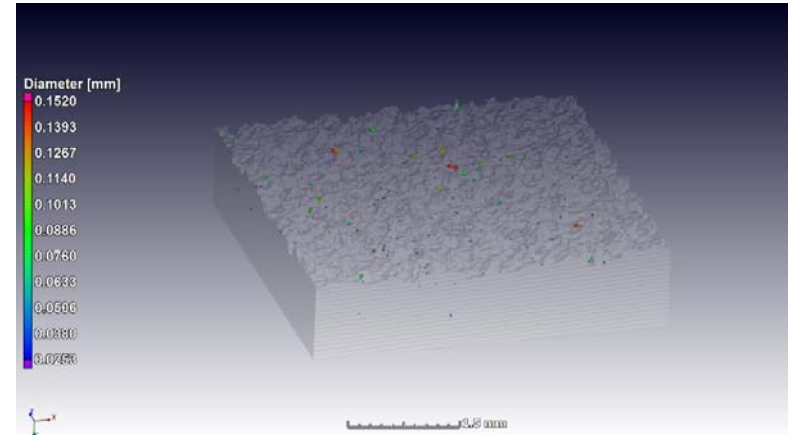
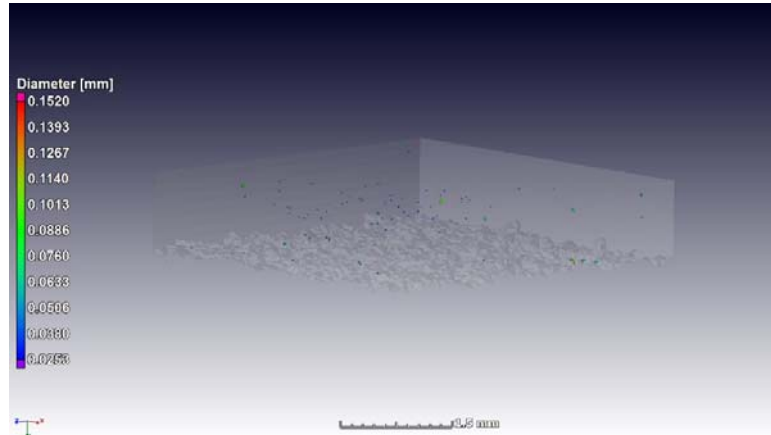


Angle (°)

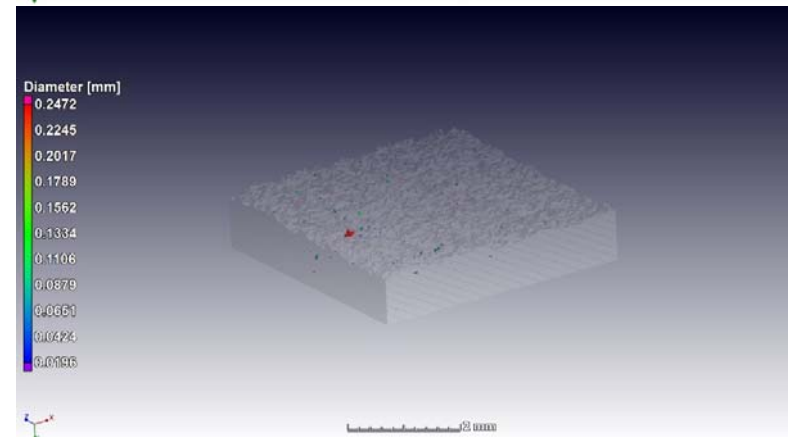
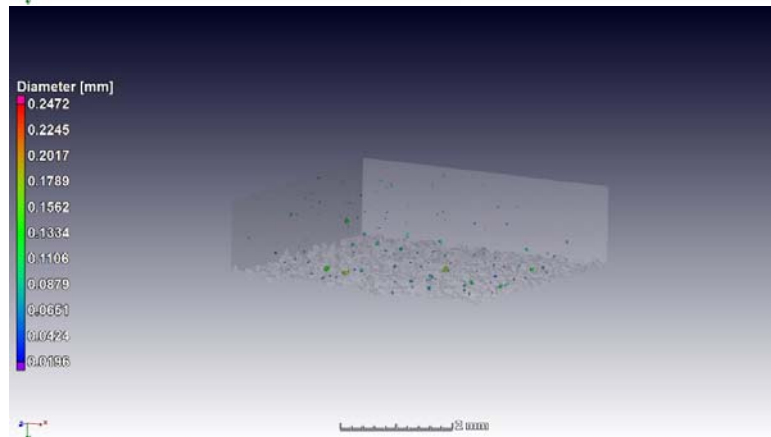
Downskin set A

Upskin set A

85



90



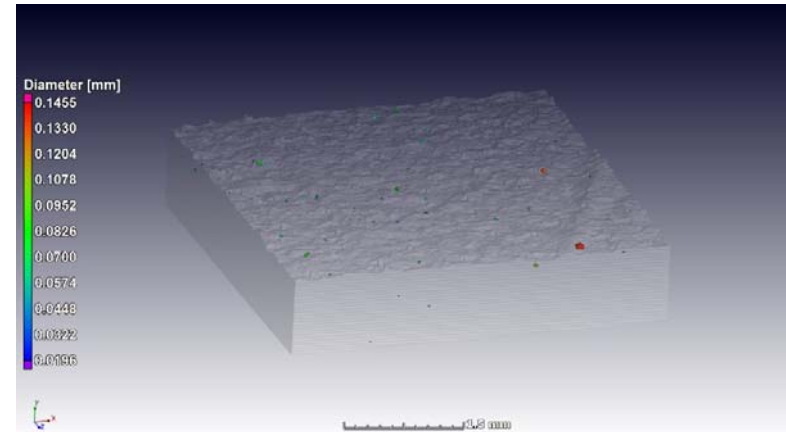
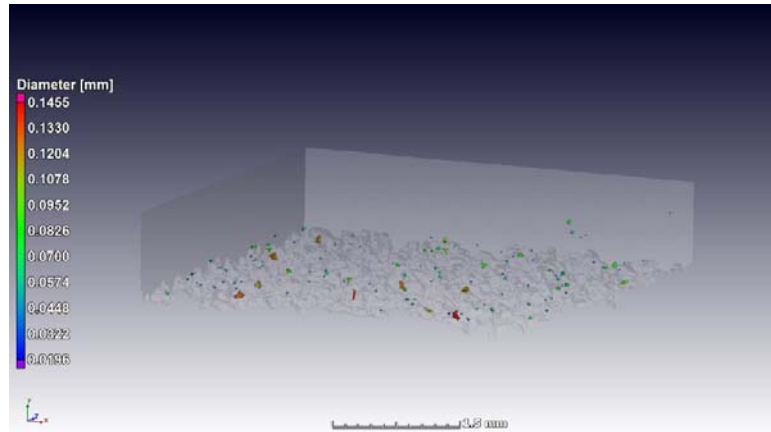
APPENDIX 10. Porosity for areas near downskin and upskin surfaces in sample B

Angle (°)

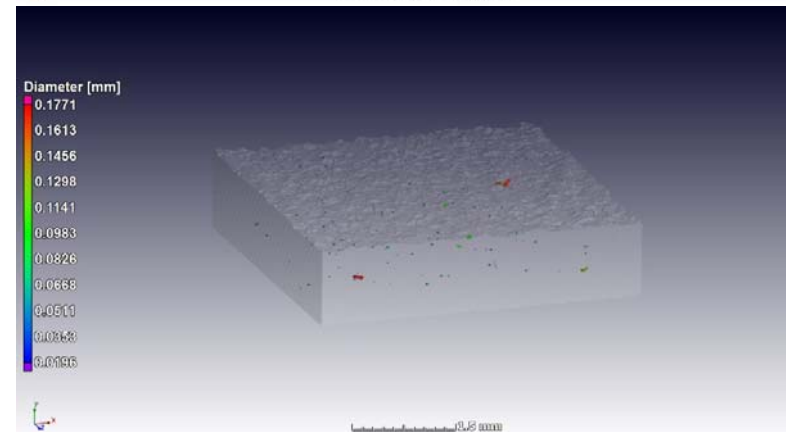
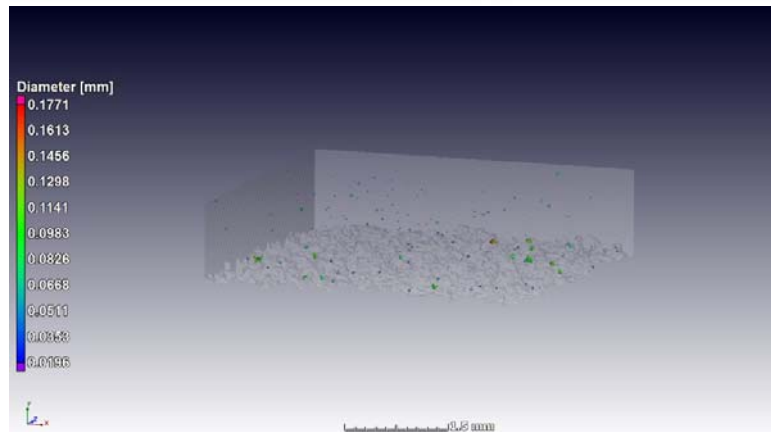
Downskin set B

Upskin set B

25



30

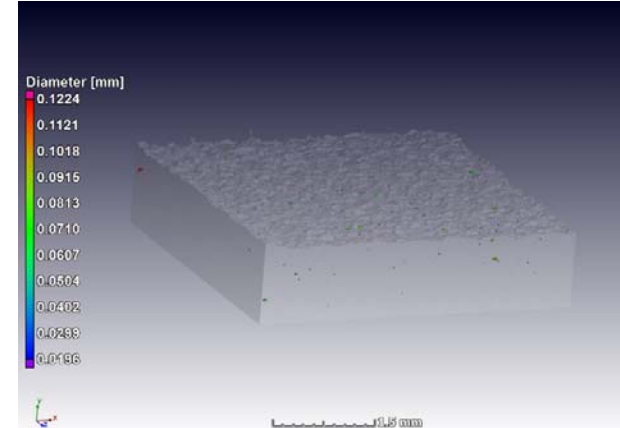
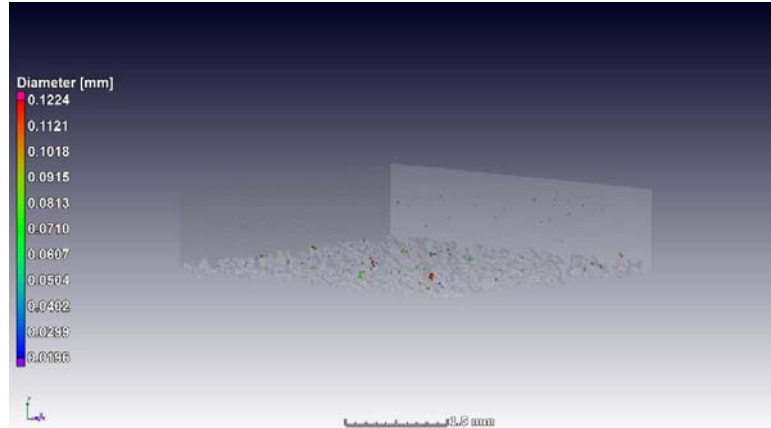


Angle (°)

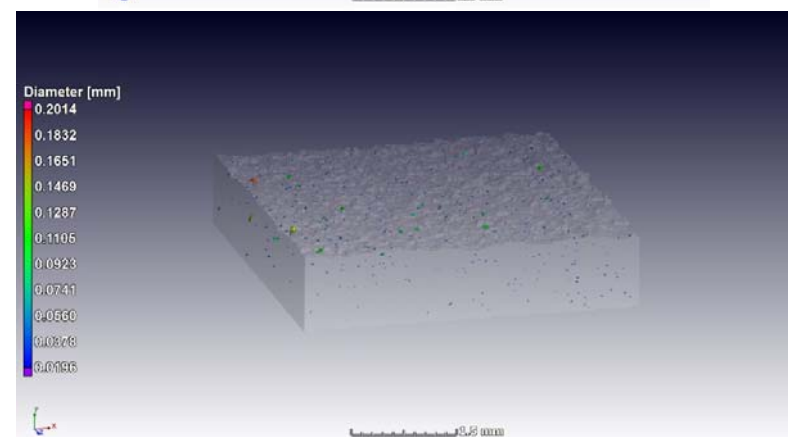
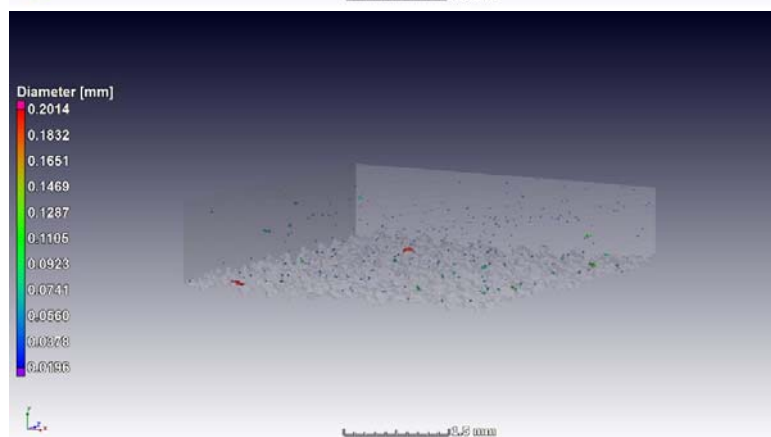
Downskin set B

Upskin set B

35



40

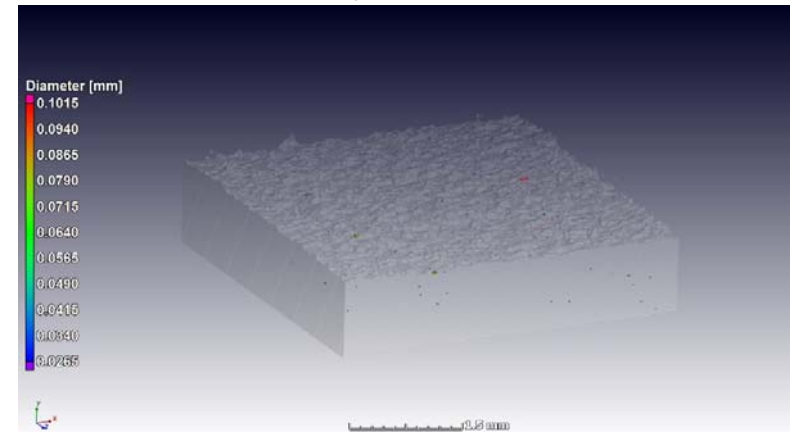
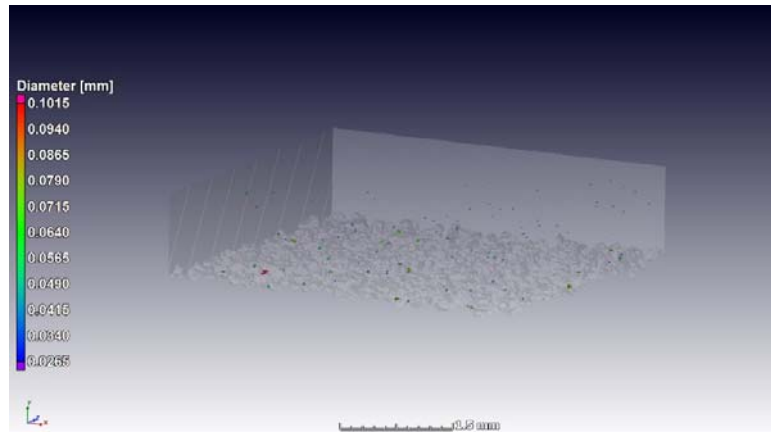


Angle (°)

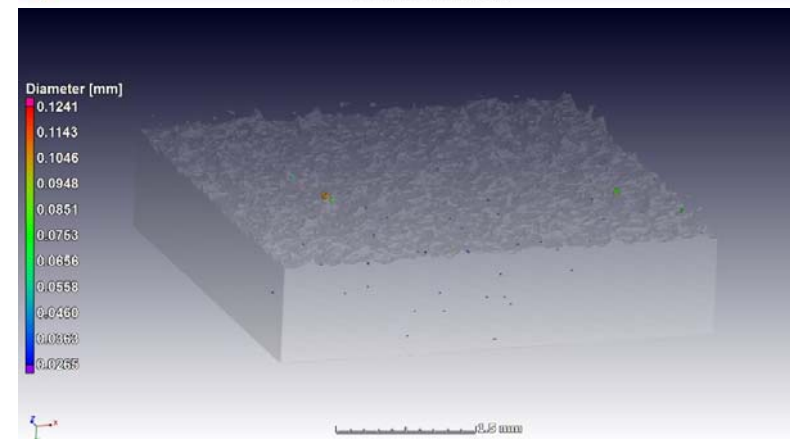
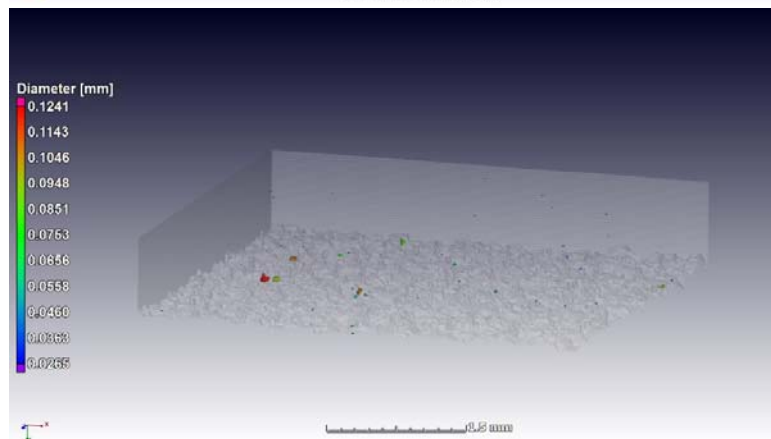
Downskin set B

Upskin set B

45



50

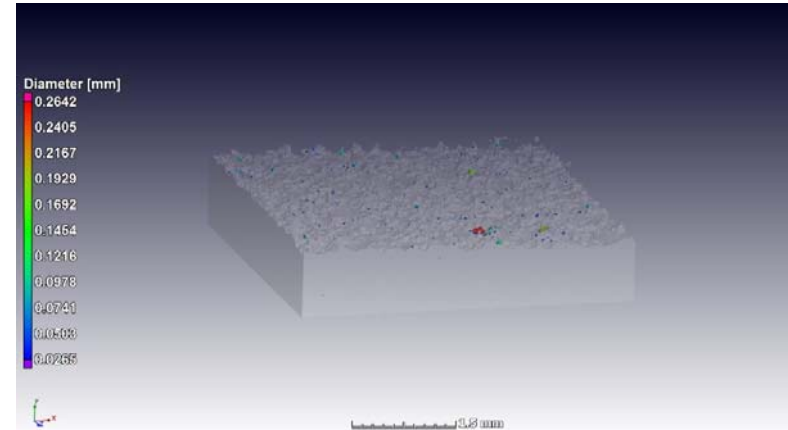
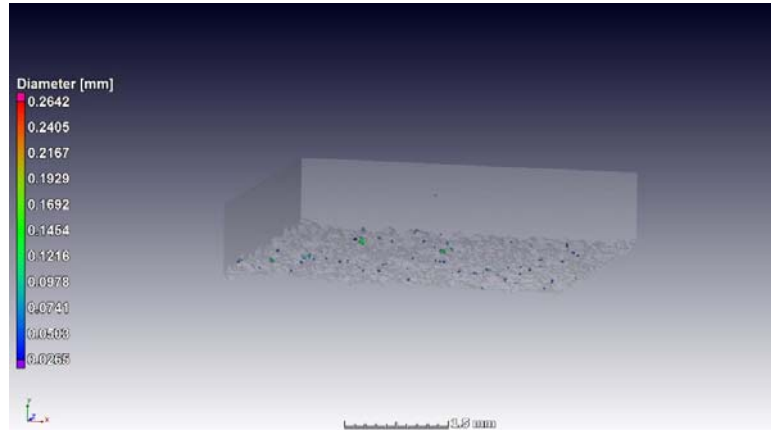


Angle (°)

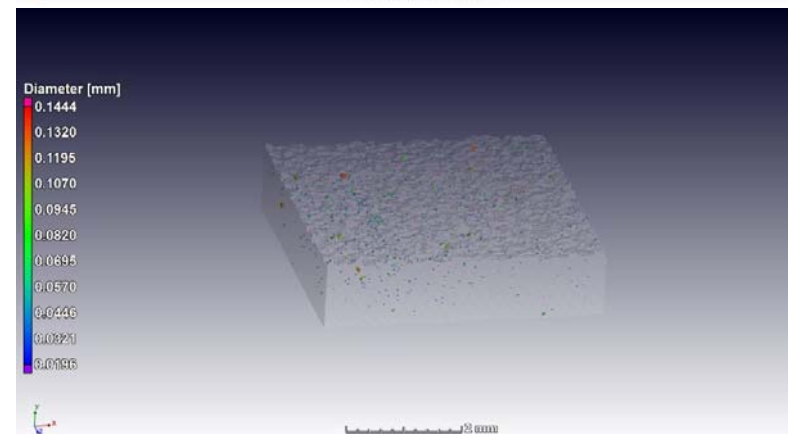
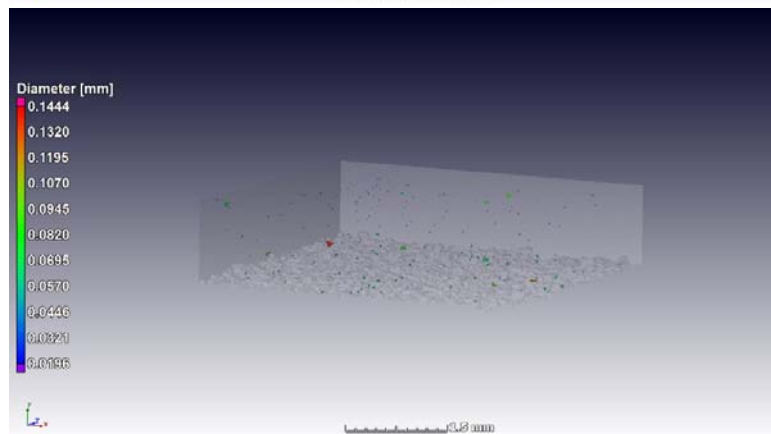
Downskin set B

Upskin set B

55



60

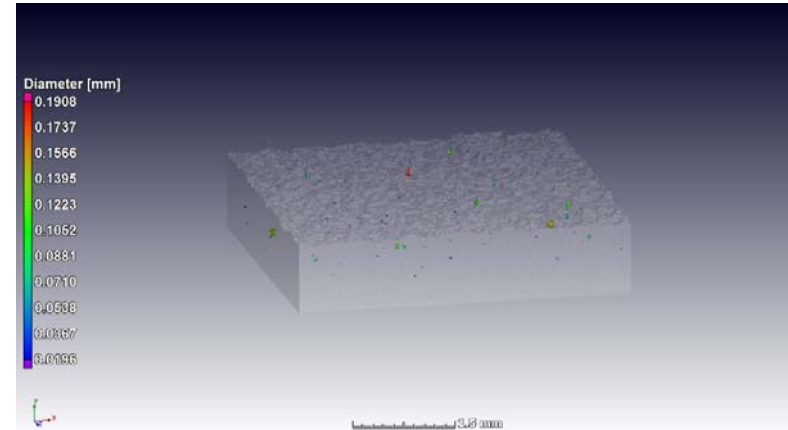
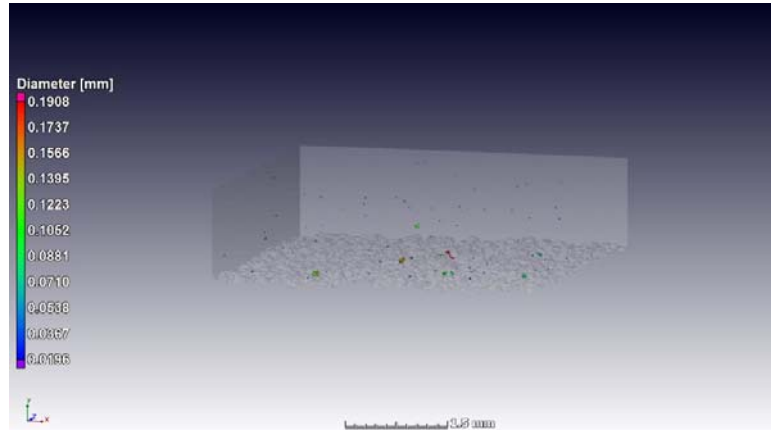


Angle (°)

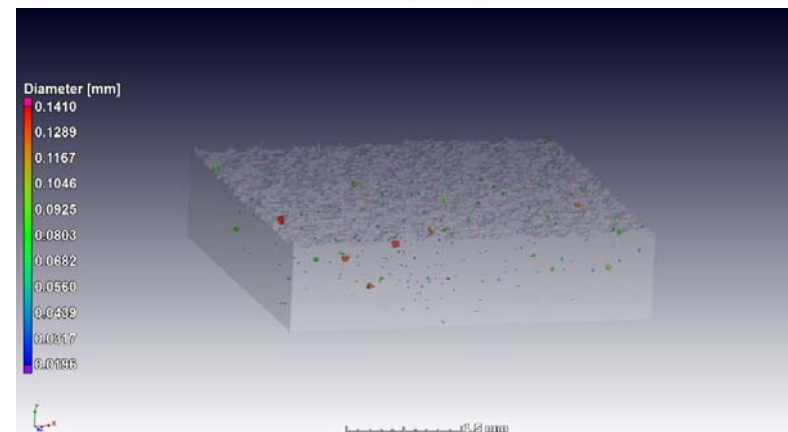
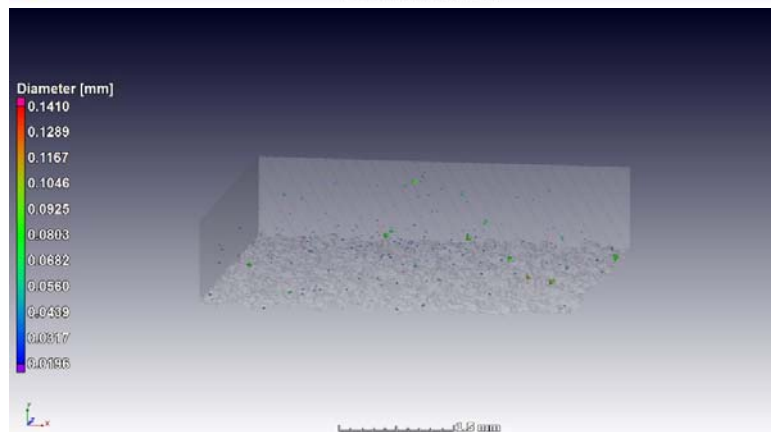
Downskin set B

Upskin set B

65



70

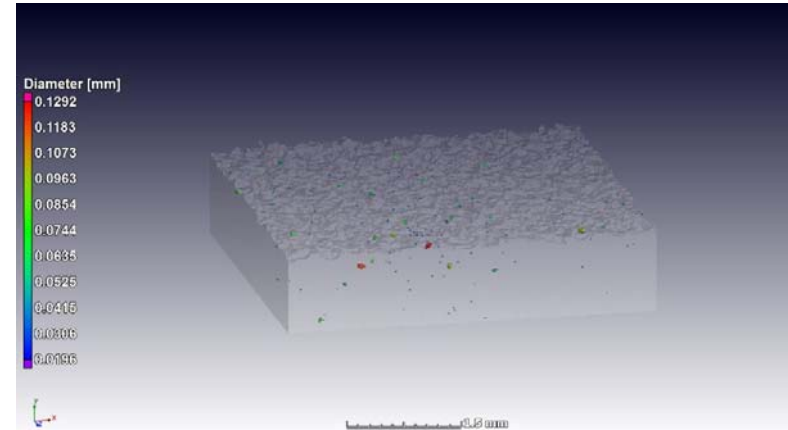
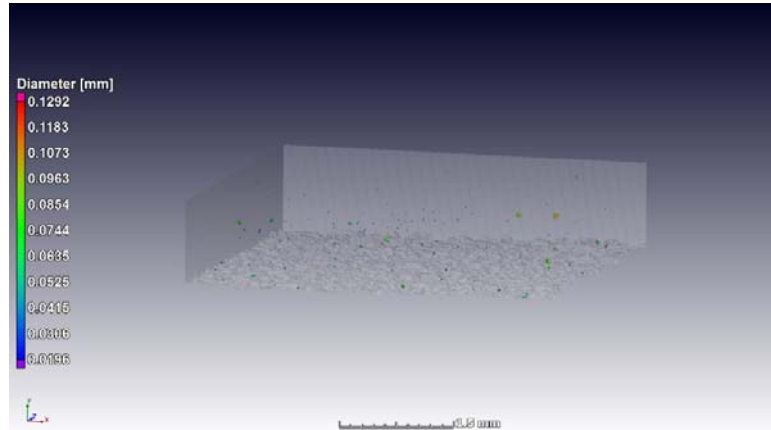


Angle (°)

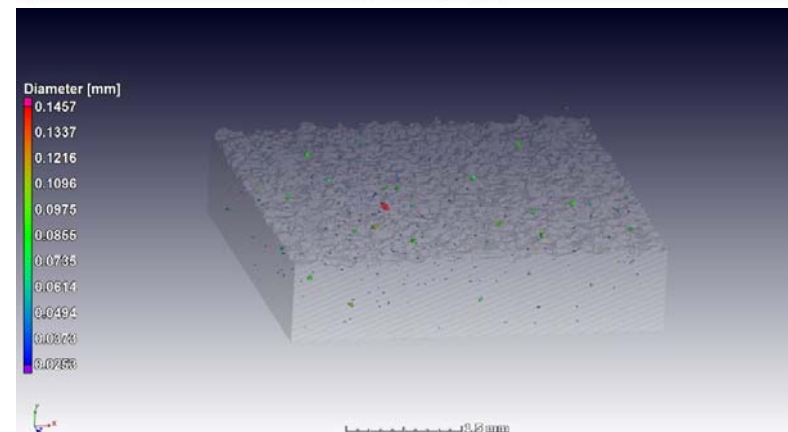
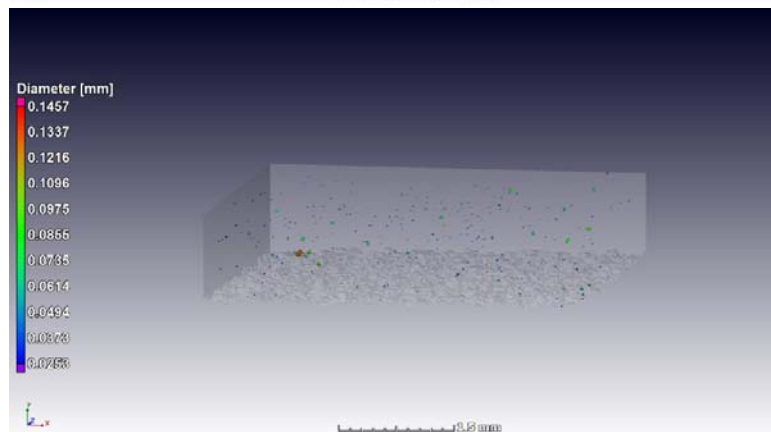
Downskin set B

Upskin set B

75



80

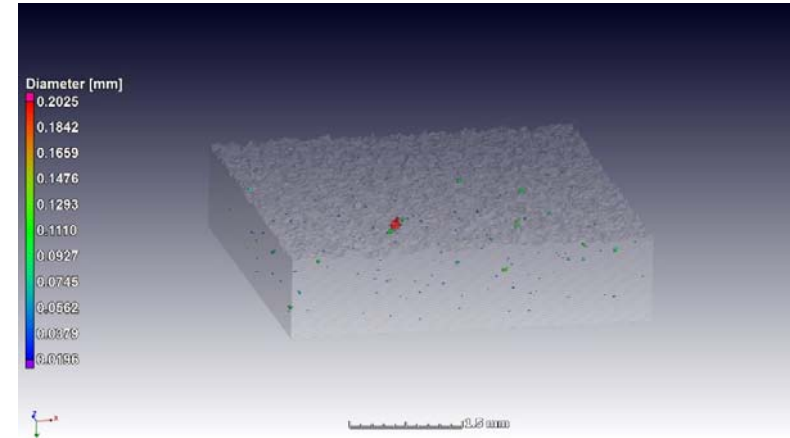
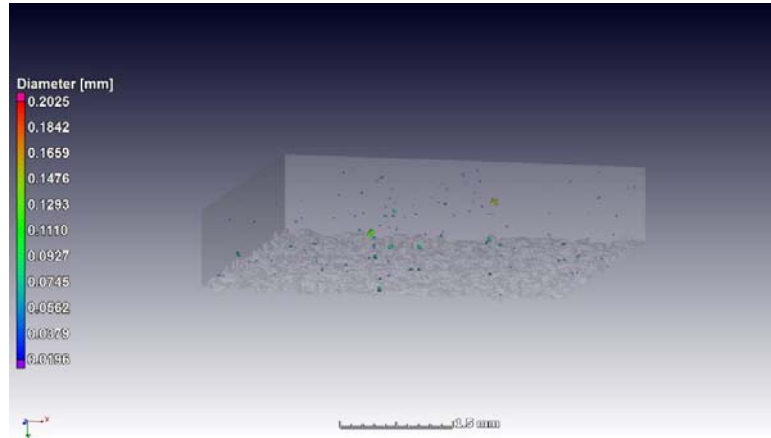


Angle (°)

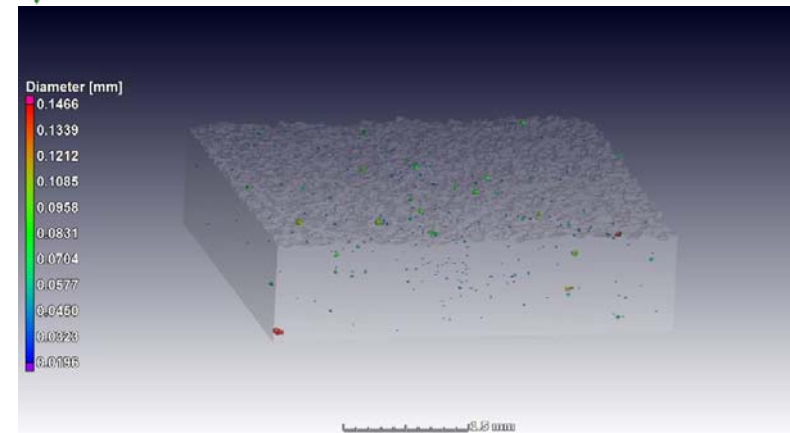
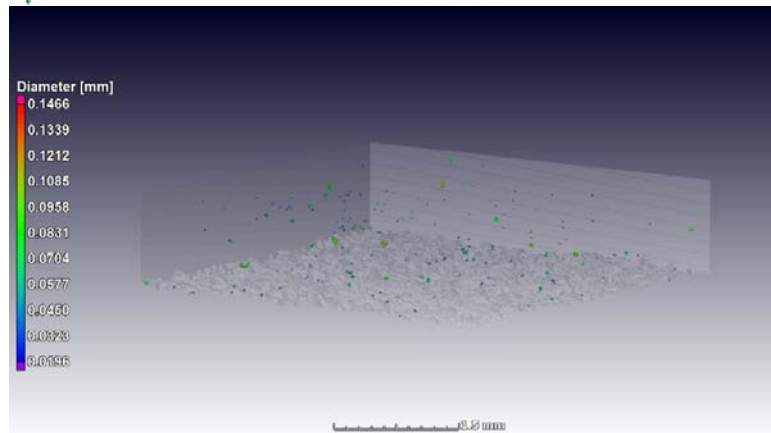
Downskin set B

Upskin set B

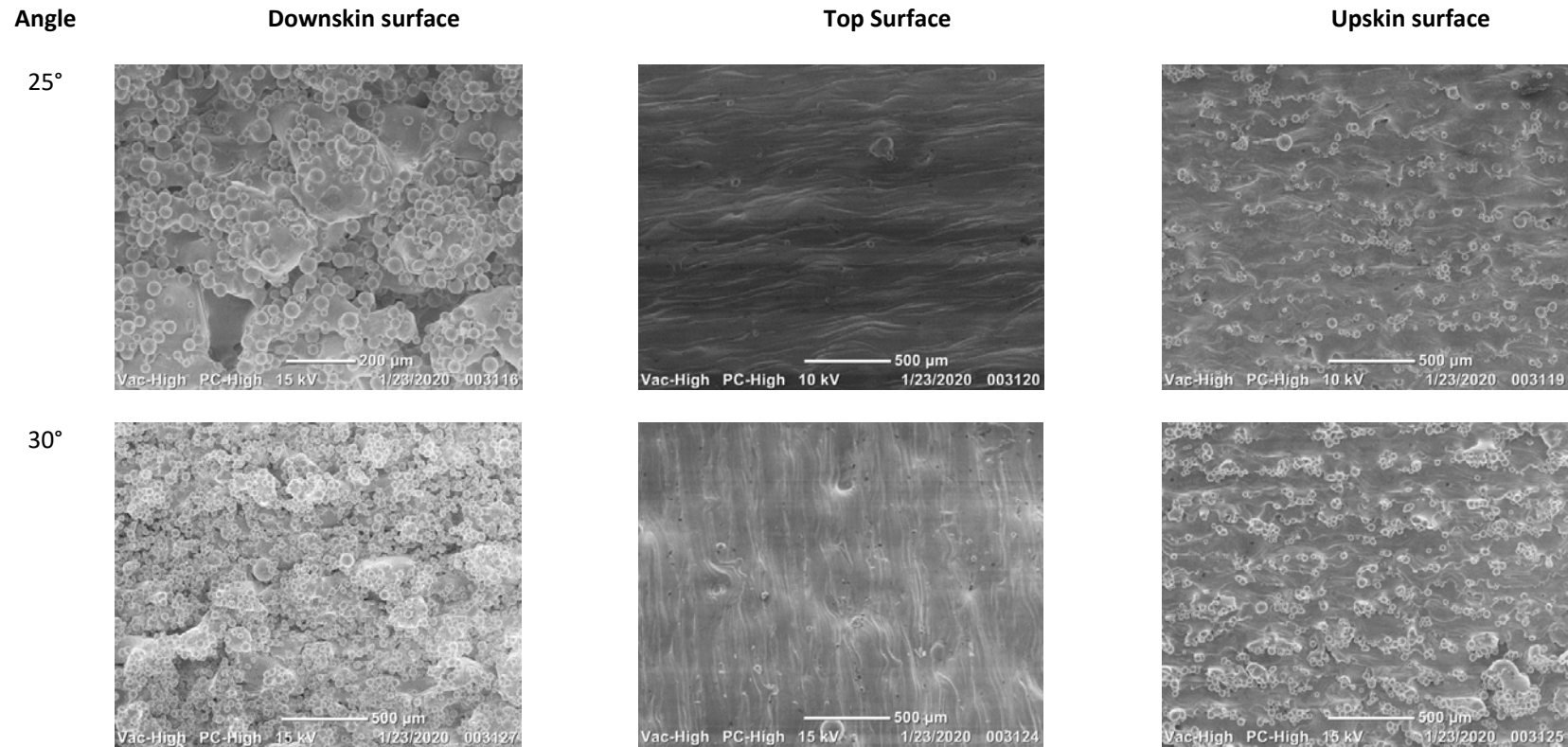
85



90



APPENDIX 11. SEM images showing the typical surfaces for the downskin, top and the upskin surfaces



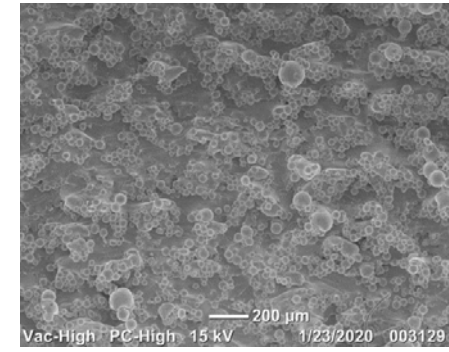
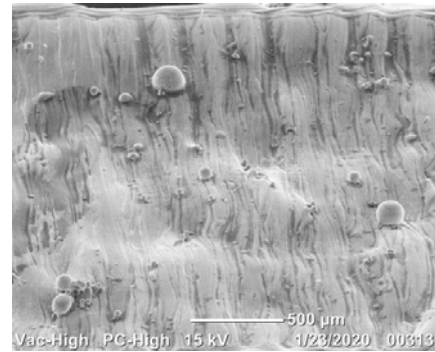
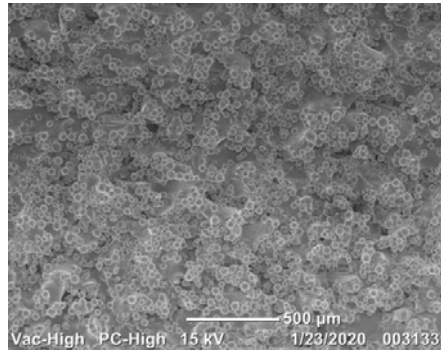
Angle

Downskin surface

Top Surface

Upskin surface

55°



90°

